UNIVERSITÀ DEGLI STUDI DI TRENTO

Doctoral School in Civil, Environmental and
Mechanical Engineering

Topic 2: Mechanics, Materials, Chemistry and Energy

Andrea Cugno

Mechanical Modelling of Single and Collective Cells Behavior

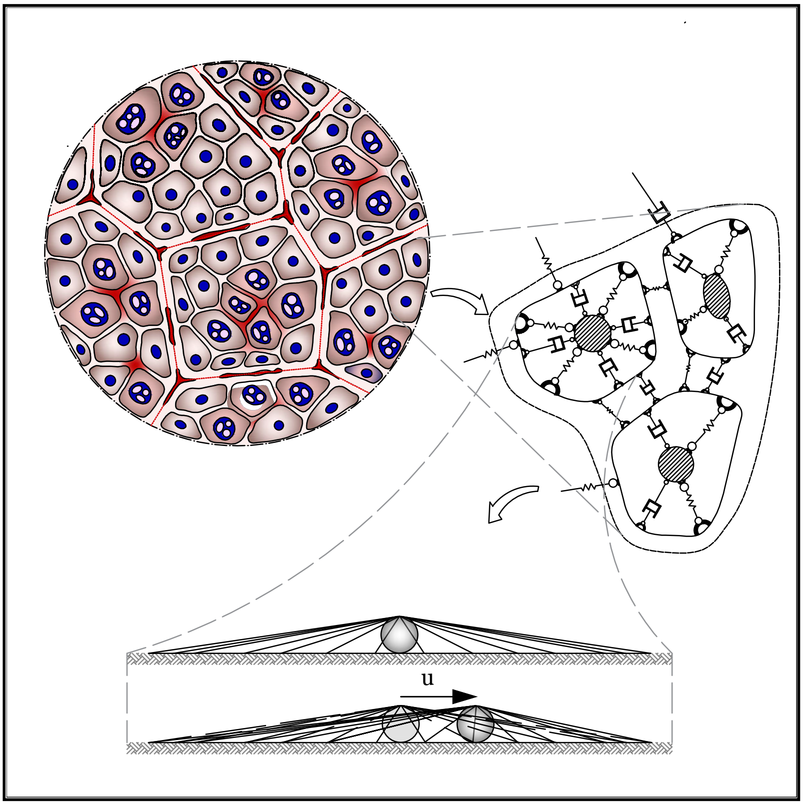

2017_Doctoral thesis

Recent experimental results have suggested important direct implications of viscoelasticity of human cells and cell cytoskeleton dynamics on some relevant collective and at single-cell behaviors such as migration, adhesion, and morphogenesis. Other experimental studies have been performed on individual cancer and healthy cells of different types, demonstrating that the former were about 70% softer than the latter. In this thesis with the aim of characterizing — and gaining insights into — the frequency response of single-cell systems to mechanical stimuli (typically LITUS), a generalized viscoelastic paradigm which combines classical and spring-pot based (fractional derivative) models is presented. Than the modelling has been enriched considering the non-linear effect of the prestress, induced in protein filaments during cell adhesion and in the cell membrane (with a simple multiscale scheme that incorporates finite elasticity and a 3-D circus tent-like model), on the overall cell stiffness and finally determining its influence on the in-frequency response of the cell. The theoretical results have shown that the differences in stiffness — at least in principle — allow us to mechanically discriminate between tumor and normal cells: the critical frequencies associated with oscillation magnitude peaks (from tens to hundreds of kilohertz) could be helpfully utilized for targeting or ad hoc altering the functions of cancer cells. An experimental validation of the theoretical results is an ongoing work and the preparation of the experimental setup is also presented.
In this thesis some first models have been presented to replicate in-vivo collective behavior of cells. Coherent angular rotation of epithelial cells has been reproduced by a cell-centered based mechanical model in which units are polarized, motile, and interact with the neighboring cells via harmonic forces. Starting from this model a continuum non-linear viscoelastic model incorporating the dynamics of liquid crystals has been studied and some preliminary numerical simulations have been performed.

Andrea Cugno was born in Avola (Sicily), Italy, on June 1, 1988. He received Bachelor and Master Degree cum laude in Biomedical Engineering from the University of Naples in 2010 and 2012, respectively. In 2013 he obtained the scholarship for the advanced training course “for specialist of Driver Monitoring systems and technologies”, from University of Naples in collaboration with Fiat Chrysler Automobiles (Pomigliano D’Arco, Naples, Italy) where he performed a “training on the job” stage. In 2014 he won the scholarship for the PhD at the University of Trento (DICAM). The principal research interests covered include: Cell Mechanics, Biomechanics, Continuum Mechanics, Viscoelasticity, Fractional Calculus. During his PhD he spent two periods abroad both in Pittsburgh, PA (USA): six months at the Institute for Complex Engineered Systems of the Carnegie Mellon University in 2014, then five months at the Department of Mechanical Engineering and Materials Science, University of Pittsburgh, in the 2016. Until now, he have coauthored 4 journal papers.

UNIVERSITY OF TRENTO - Italy
Department of Civil, Environmental
and Mechanical Engineering

Doctoral School in Civil, Environmental and Mechanical Engineering
Topic 2: Mechanics, Materials, Chemistry and Energy - XXIX cycle 2014/2016

Doctoral Thesis -April 2017

Andrea Cugno

Mechanical Modelling of single and collective cells behavior

Supervisors
prof Luca Deseri University of Trento (DICAM)
prof Massimiliano Fraldi University Federico II of Naples (DISIA)

Except where otherwise noted, contents on this book are licensed under a Creative
Common Attribution - Non Commercial - No Derivatives
4.0 International License

University of Trento
Doctoral School in Civil, Environmental and Mechanical Engineering
http://web.unitn.it/en/dricam
Via Mesiano 77, I-38123 Trento
Tel. +39 0461 282670 / 2611 - dicamphd@unitn.it

To my family, the only one that, at the end, has been, are and will be close to me. The have supported me always unconditionally.

Alla mia famiglia, le uniche persone che alla fine mi sono state, sono e sempre saranno vicine. Mi hanno supportato sempre incondizionatamente.

ACKNOWLEDGMENTS

First and foremost, I would like to sincerely and deeply thank my Bachelor, Master and PhD advisor Professor Massimiliano Fraldi, for his professionalism, for having guided me with patience until this achievement. Without his words and his trust felt in the right moment, things would have been different, an excellent motivator, a person with a deep culture.

My best acknowledgments are for my other PhD tutor Professor Luca Deseri, a person from which one can learn a lot, a formidable researcher. Also thanks to him I had the opportunity to spent two periods abroad in top level places and collaborating with top level people.

I deeply acknowledge Professor Kaushik Dayal for having hosted me at Carnegie Mellon and for all his ad-vices on the numerical issues.

Finally but not last, a special acknowledgement is dedicated to professor Giovanni Paolo Galdi for having hosted me at the university of Pittsburgh, and for making me feel his esteem. It was an honor to meet him.

SUMMARY

Cells are fundamental units of any biological material. Their single and collective behaviors and the way in which they grow and aggregate interacting with the extracellular matrix to form tissues and organs in the human being are at the basis of most of the current resarch efforts in biology, medicine and bioengineering. Despite this great interest, many cell processes and related mechanobiological phenomena are still obscure or only partially understood.

Recent experimental results have suggested important direct implications of viscoelasticity of human cells and cell cytoskeleton dynamics on some relevant collective and at single-cell behaviors such as migration, adhesion, and morphogenesis. As a consequence, the mechanical properties of single cells and how cells respond to mechanical stimuli have gained increasing interest and to date are at the center of a vivid debate in the scientific community.

It has been observed, for example, that the effect of UltraSound (US) upon single cells is significantly influenced by the sonication protocol tratment in terms of the frequency and the energy density applied [56]. In fact, cell membrane damage has been induced by US in human blood cells and leukaemic cell lines [38] and it has been also seen that malignant cells are sometimes much more susceptible and prone to be killed than normal cells when subjected to ultrasound exposure [79, 80]. Further studies have shown that Low Intensity UltraSound (LITUS) decreases cell growth and induces cell death (apoptosis), inhibits cell proliferation in different kind of cell cancer lines as well as increases and stimulates wound healing [16, 62, 118] although the same investigators admit that "the molecular mechanism has not yet been clearly understood". The biologically relevant motion of intracellular particles, induced by ultrasonic waves, has been hypothesized to play a key role in the mechanism underlying the relative displacement between cell organelles and cytoplasm as an effect of the different inertias of the media. Although the question of how the mechanical vibrations act on the biological cell behaviour remains substantially an open issue, a study by Or & Kimmel [103] theoretically explores the possibility of resonance-like phenomena and suggests that mechanically induced oscillations —larger than maximal thermal fluctuations— might kindle high-frequency (compatible with low-

intensity therapeutic ultrasound (LITUS) ranges) strain regimes, potentially able to determine fatigue-like phenomena in cells. In particular, the frequency resonance hypothesis assumes that the absorption of ultrasound by proteins and protein complexes may directly alter signalling mechanisms within the cell, determining conformational shift or disrupting multimolecular complexes at critical frequencies around both 45 kHz and 1 MHz [66].

On the other hand, very recently, experimental studies have been performed on individual cancer and healthy cells of different types, demonstrating that the former were about 70% softer than the latter [1, 22, 23, 41, 70, 81–83, 85, 100, 104, 113, 115]. It seems that the increase in cell deformability is directly related to cancer progression, as observed by Ketene et al. [70] in the case of a transformed phenotype from a benign (non-tumorigenic) cell to a malignant (tumorigenic) one. Ploidinec et al. [111], by resolving the *nanomechanical signatures* of defined stages of tumour progression, also confirm that cancer evolution is associated with a significant softening of tumour epithelial cells in comparison with normal mammary epithelium, including metastasis, hypothesizing that metastatic cells gain their migration capabilities by acquiring a certain degree of flexibility and deformability to escape their original niche. Very recently, some studies have in detail modeled single-cell response to mechanical stimuli [44, 45, 59, 60].

Here, by recalling the above-mentioned experimental evidences related to the discrepancies in deformability between tumour and normal cells, with the aim of characterizing — and gaining insights into — the frequency response of single-cell systems to mechanical stimuli (typically LITUS), a generalized viscoelastic paradigm which combines classical (say Voigt, Maxwell and standard linear Kelvin (SLK)) and spring-pot-based (fractional derivative) models is presented in Chapter 2, in Chapter 1 preliminary introducing the fundamentals of nonlinear mechanics and classical and fractional viscoelasticity used in the PhD dissertation. To this first purpose, any detail on the complex structural organization of the cells in which the nucleus, cytoskeleton, elastic membrane and gel-like cytosol govern and interact with the cascade of events at the basis of the mechanobiology of the system has necessarily been neglected. After preliminary sensitivity analyses aimed to catch both qualitative and quantitative remarks on mechanically stimulated single-cell systems, the viscoelastic modelling was thus confined to cell lines whose mechanical properties have been experimentally measured in the literature with reference to healthy cells and their cancer counterparts. The theoretical results will show that the differences in stiffness — at least in principle — allow us to mechanically discriminate between tumour and normal cells, the critical frequencies associated with oscillation magnitude peaks (from tens to hundreds of kilohertz) confirming that mechanical resonance-like phenomena can prevail with respect to thermal fluctuations and thus could be helpfully used for targeting or *ad hoc* altering the functions of tumour cells. Furthermore, by making reference to experimental studies which evaluated the stiffness of single cells by means of Atomic Force Microscopy, Optical Tweezers and other techniques, it emerges that, when dealing with living systems, these measures of stiffness can be significantly affected by intrinsic structural changes of the biological matter, for example by the reorganization dynamics guided by polymerization-depolymerization processes, which change the internal configuration of the cytoskeleton in this way regulating adhesion and migration cell capabilities and in turn provoking nonhomogeneous cell deformations and changes in stiffness ([3, 9, 116]), with Young's moduli also oscillating from approximately 100 Pa to $10kPa$ ([11, 22, 23, 41, 70, 81–83, 85, 100, 113, 115]).

However, the vast majority of the experimental data somewhat consider stiffness of "round" (suspended) cells and not much effort has been devoted, from the modeling standpoint, to mechanically relate the overall change of cell stiffness to its stretched configuration and to the average number of active/assembled cytoskeletal filaments. Therefore, with the aim to enrich the modeling of single-cell systems, in Chapter 2 has also been considered the effect of the prestress (for instance, induced in protein filaments during cell adhesion) on the overall cell stiffness, finally determining its influence on the in-frequency response of the cell. To this end, a simple multiscale scheme that incorporates finite elasticity has been first proposed to include, by using a bottom-up homogenization procedure, suitable prestress-modified stiffness values into the viscoelastic single-cell models. Once the analytical expression of the overall elastic stiffness of an adherent cell has been obtained, some key model parameters (i.e., prestretch and number of "active" filaments) are then identified and determined to fit the realistic stiffness moduli experimentally measured in the literature for several cell types. Finally, considering the generalized spring-pot based (fractional derivative based) viscoelastic models above mentioned, the role played by the stretched state of the cytoskeletal elements on the cell vibration is studied in detail through sensitivity analyses in order to catch the variation on the resonance-like frequencies of the vibrational displacement of the nucleus with respect to its environment.

Successively, an enhanced 3-D *circus tent-like* model, which includes finite elasticity and involves prestretched filaments in the membrane as well as the deformation of the nucleus, has been introduced to better capture the actual effects of the cell configuration states on the overall *out of plane stiffness*. For modeling the nonlinear mechanical behavior of the cell membrane, by considering some recent analytic and experimental results regarding the stiffness tuning effect of Dielectric Elastomer followed by the application of a Electrical Field [27, 107–109], it has been constructed an analytical approach to find a solution of memebrane-nucleus coupled problem. The model proposed could be helpfully utilized in AFM experimental measurements when determining stiffness maps for example to give formulas for obtaining how actual prestress level in the cell membrane influence the overall cell elasticity.

To replicate more faithfully in-vivo behavior of cells, in Chapter 3, preliminary results and some first models have been presented to investigate the role that mechanics plays in *collective* cell behaviors, relevant in wound healing and embrogenesis processes (gastrulation). In fact, Wolgemuth et al. [78] suggest that wound healing is predominantly a mechanical process that is modified, but not produced, by cell-cell signaling. Coherent angular rotation of epithelial cells, occuring during many vital physiological processes including tissue morphogenesis and glandular formation, has been replicated by Mandar et al [122] by a cell-centered based mechanical model in which units are polarized, motile, and interact with the neighboring cells via harmonic forces. Starting from the above mentioned literature, a continuum non-linear viscoelastic model (upper convected Maxwell model) incorporating the dynamics of liquid crystals has been studied and some numerical simulations have been performed in order to reproduce recent experimental biological evidences for collective behavior of cells such as gastrulation.

Some in-progress experimental activities in act in the laboratory of the Institute of the Applied Sciences and Intelligent Systems "ISASI- Eduardo Caianiello" of the National Research Council (CNR) have been illustrated in Chapter 4. The activities have been to date limited to asses the experimental procedure and calibrate the setup. Subsequently analyzing cancer and healthy cell lines, ultrasounds will be applied at selected frequencies to prove the theoretical principle described in Chapter 2.

PUBLICATIONS

Some ideas and figures con be found in the following publications that I have co-authored:

- M. Fraldi, **A. Cugno**, L. Deseri, K. Dayal, and N. M. Pugno. “A frequencybased hypothesis for mechanically targeting and selectively attacking cancer cells.” In: *Journal of The Royal Society Interface* 12.111 (2015), p. 20150656. issn: 1742-5689. doi:10.1098/rsif.2015.0656. url: http : rsif . royalsocietypublishing.org / lookup/doi / 10.1098/ rsif.2015.0656.
- M Fraldi, **A Cugno**, A R Carotenuto, A Cutolo, N M Pugno, and L Deseri. “Small-on-Large Fractional Derivative Based Single-Cell Model Incorporating Cytoskeleton Prestretch.” In: *Journal of Engineering Mechanics* (2016), p. D4016001. issn: 0733-9399. doi: 10.1061/(ASCE) EM.1943- 7889. 0001178. url: http: // ascelibrary.org/doi/10.1061/(ASCE)EM. 1943-7889.0001178.
- S. S. Soumya, A. Gupta, **A. Cugno**, L. Deseri, K. Dayal, D. Das, S. Sen, and M. M. Inamdar. “Coherent Motion of Monolayer Sheets under Confinement and Its Pathological Implications.” In: *PLOS Computational Biology* 11.12 (2015). issn: 1553-7358. doi: 10.1371/journal. pcbi.1004670.
- **A. Cugno**, S. Palumbo, L. Deseri, M. Fraldi, and C. Majidi. “Role of Nonlinear Elasticity in Mechanical Impedance Tuning of Annular Dielectric Elastomer Membrane.” *Under revision in Extreme Mechanics Letters* (2017), pp. 1–18.

CONTENTS

1 MEACHANICAL FRAMEWORK 1
  - 1.1 Kinematics 1
  - 1.2 Concept of stress and balance of linear and angular momenta 8
  - 1.3 Work conjugate 10
  - 1.4 Constitutive Equation: isotropic non-linear hyperelasticity 13
  - 1.5 Classical and Fractional linear viscoelasticity 17

2 SINGLE CELL MECHANICS 23
  - 2.1 Frequency response of one-dimensional single-cell viscoelastic systems 27
    - 2.1.1 Cells behaving as quasi-standard Voigt model 29
    - 2.1.2 Cells behaving as quasi-standard Maxwell model 32
    - 2.1.3 Cells behaving as Spring-Pot based quasi-Standard Linear Kelvin model 33
  - 2.2 Sensitivity analyses and resonance hypothesis in single-cell dynamics 36
  - 2.3 Frequency-based detection of cancer and healthy cells at single-cell level 43
  - 2.4 Elemental nonlinear elastic model of an adherent cell 47
  - 2.5 3D-Circus Tent model for the Cell 62
    - 2.5.1 Cell-Membrane 63
    - 2.5.2 Cell-Nucleus 67
    - 2.5.3 Coupling 68

3 MECHANICAL MODELLING OF COLLECTIVE BEHAVIOR OF CELLS 73
  - 3.1 introduction 73
  - 3.2 Cell-centered discrete model for collective behavior 73
    - 3.2.1 Computational model 74
    - 3.2.2 Results 77
  - 3.3 Continuum model for collective behavior 88
    - 3.3.1 Mechanical Model 88
    - 3.3.2 preliminary results 90

4 IN PROGRESS EXPERIMENTAL ACTIVITY 93
  - 4.1 State of art 93

4.1.1 FEM Validation 93
4.1.2 Modal Analysis (FEM) 95
4.1.3 Harmonic vibration analysis 96
4.1.4 Ultrasonic irradiation of MCF7 and MCF10A cells 97
4.1.5 Selective toxicity of MCF7 cells at 24.5 kHz under 2D and 3D culture conditions 97
4.1.6 Increased cytotoxicity after fractionated ultrasonic irradiation 99
4.1.7 Combination of ultrasonic irradiation and paclitaxel 100
4.2 Preparation of the experimental Setup (at the ISASI) 102
4.2.1 Experiments 104
5 CONCLUSION & FUTURE PERSPECTIVE 111

BIBLIOGRAPHY 115

LIST OF FIGURES

Figure 1.1 Elstic Solid 17
Figure 1.2 Viscous fluid 18
Figure 1.3 Voigt model 19
Figure 1.4 Maxwell Model 20
Figure 1.5 Spring Pot 22
Figure 2.1 Cartoon of the idealized single-cell system: (*top-right*) healthy and tumor cells agglomerate; (*top-left*) typical cell unit, with nucleus and cytoskeleton structure embedded in the cytosol and confined by the lipid bilayer cell membrane; (*bottom-left*) idealized single-cell system with cell nucleus oscillating in a viscoelastic environment under the action of radiating ultrasound source; (*bottom-right*) adopted viscoelastic schemes (Voigt, Maxwell and generalized Spring-Pot based Standard Linear Kelvin models). 28
Figure 2.2 Sensitivity analysis for the frequency response of the cyclic displacement amplitude of a spherical object ($R = 1\ \mu$m) with respect to its surroundings with low viscosity ($\mu = 10^{-3}\,Pa \times s$) and varying Young modulus ($E = 100, 500, 1000, 5000, 10000\,Pa$): (**V**) Voigt; (**M**) Maxwell; (**SLK**) Standard Linear Kelvin; (**SLK_1**) generalized Standard Linear Kelvin with spring-pot in position 1, (**SLK_2**) 2 and (**SLK_3**) 3, with $\alpha = 0.5$. 38
Figure 2.3 Sensitivity analysis for the frequency response of the cyclic displacement amplitude of a spherical object ($R = 1\,\mu m$) with respect to its surroundings with stiffness ($E = 2100\,Pa$) and varying viscosity ($\mu = \left[10^{-3} \sim 10\right]\,Pa \times s$): (**V**) Voigt; (**M**) Maxwell; (**SLK**) Standard Linear Kelvin; (**SLK_1**) generalized Standard Linear Kelvin with spring-pot in position 1, (**SLK_2**) 2 and (**SLK_3**) 3, with $\alpha = 0.5$. 39

Figure 2.4 Sensitivity analysis for the frequency response of the cyclic displacement amplitude of a spherical object with respect to its surroundings with stiffness ($E = 2100\,\mathrm{Pa}$) viscosity ($\mu = 10^{-3}\,\mathrm{Pa}\times\mathrm{s}$) and varying size of the object ($R = 0.1, 1, 5, 10, 20\,\mu\mathrm{m}$): (**V**) Voigt; (**M**) Maxwell; (**SLK**) Standard Linear Kelvin; (**SLK_1**) generalized Standard Linear Kelvin with spring-pot in position 1, (**SLK_2**) 2 and (**SLK_3**) 3, with $\alpha = 0.5$. 40

Figure 2.5 Frequency response, in terms of relative displacement amplitude vs frequency, of Healthy (H) and Cancer (C) mesothelial cells extracted from carcinoma of the lung, simulated through the proposed viscoelastic schemes: ($R = 1\,\mu m$; $\mu = 10^{-3}\,Pa\times s$; measured cancer Young modulus:$E = 560\,Pa$; measured healthy Young modulus: $E = 2100\,Pa$). The six graphics are reffered to the following models: (**V**) Voigt; (**M**) Maxwell; (**SLK**) Standard Linear Kelvin; (**SLK_1**) generalized Standard Linear Kelvin with spring-pot in position 1, (**SLK_2**) 2 and (**SLK_3**) 3, with $\alpha = 0.5$. The grey regions highlight the difference in frequency between peaks in cancer and healthy cells. Dashed lines represent the displacement amplitudes corresponding to the thermal fluctuations, always smaller than the mechanical ones. 45

Figure 2.6 Bar-chart with synopsis of the theoretically derived in-frequency responses of healthy and cancer cells whose mechanical properties have been experimentally measured: the histograms compare peak frequencies for each tumor and normal cell line pair examined, by averaging over all the results obtained from the six viscoelastic schemes utilized. The first column reports the cell type and the corresponding literature reference from which the data are deduced; the last two columns give some quantitative results in terms of ratio between maximum ($\frac{(\Delta f)_{max}}{f_H}$) and minimum frequency shifts ($\frac{(\Delta f)_{min}}{f_H}$) over the reference resonance-like frequency of the healthy cell, for each cell line. 46

Figure 2.7 Cartoon –with plan and lateral views– of the elemental cell cytoskeleton structure: a) initial (stress-free) unknown configuration; b) adherent cell with non-linearly prestretched/prestressed filaments (reference configuration); c) *small-on-large* cell deformation induced by nucleus displacement (current configuration) 49

Figure 2.8 Illustration of how the axial forces kindled in each string contribute to the equilibrium of the nucleus: the angles ϕ_j are referred to the actual (displaced) nucleus position. 50

Figure 2.9 Plot of the dimensionless contribution of a filament to the cell stiffness as function of the prestretch: note that –for different Poisson's ratio values– a minimum is always highlighted. 53

Figure 2.10 Parametric analyses for the equivalent Young modulus of a single-cell system for different Poisson's ratios: a) elastic stiffness versus prestretch with fixed number of active filaments (75); b) elastic stiffness versus number of (active) filaments, with prescribed prestretch value ($\lambda_p = 1.3$). 55

Figure 2.11 Sensitivity analysis for the frequency response of the cyclic displacement amplitude of a spherical object ($R = 1\ \mu m$) with respect to its surroundings with prescribed viscosity ($\mu = 10^{-3}\, Pa \times s$) and varying Young modulus ($E = 100, 500, 1000, 5000, 10000\, Pa$ (**V**) Voigt; (**M**) Maxwell; (**SLK**) Standard Linear Kelvin; (**SLK_1**) generalized Standard Linear Kelvin with spring-pot in position 1, (**SLK_2**) 2 and (**SLK_3**) 3, with $\alpha = 0.5$. 57

Figure 2.12 Sensitivity analysis for the frequency response of the cyclic displacement amplitude of a spherical object ($R = 1\ \mu$m) with respect to its surroundings with prescribed viscosity ($\mu = 10^{-3}\, Pa \times s$), tangent Young modulus ($E = 2.6 \times 10^{9} Pa$) and Poisson ratio ($\nu = 0.4$) of the microfilaments, for a fixed number of active filaments ($n = 50$), varying the level of prestretch ($\lambda_p = 1, 1.5, 2, 3, 4$): (**V**) Voigt; (**M**) Maxwell; (**SLK**) Standard Linear Kelvin; (**SLK_1**) generalized Standard Linear Kelvin with spring-pot in position 1, (**SLK_2**) 2 and (**SLK_3**) 3, with $\alpha = 0.5$. 58

Figure 2.13 Sensitivity analysis for the frequency response of the cyclic displacement amplitude of a spherical object ($R = 1\ \mu$m) with respect to its surroundings with prescribed viscosity ($\mu = 10^{-3}\, Pa \times s$), tangent Young modulus ($E = 2.6 \times 10^{9} Pa$) and Poisson ratio ($\nu = 0.4$) of the microfilaments, for a fixed level of prestretch ($\lambda_p = 1.3$), varying number of active microfilaments ($n = 50, 100, 150, 200, 250$): (**V**) Voigt; (**M**) Maxwell; (**SLK**) Standard Linear Kelvin; (**SLK_1**) generalized Standard Linear Kelvin with spring-pot in position 1, (**SLK_2**) 2 and (**SLK_3**) 3, with $\alpha = 0.5$. 59

Figure 2.14 Cartoon of an adherent cell (a)), in the unkown rest and prestretched configuration, and its axysimmetric schematic idealization (b)). The nucleus, for sake of simplicity, is assumed to be a cylinder with radius r_i and height h in the prestretched configuration. The membrane is modeled as an annulus with external radius r_e and thickness t. The effect of prestretch it to compress the nucleus. 62

Figure 2.15 Longitudinal stretch λ_l vs prestretch λ_p that guarantee the equilibrium $f_n + f_m = 0$ with a specific choiche of the parameters: $\mu_m = 500\,Pa$, $\mu_n = 1000\,Pa$, $R_n = 500\,Pa$, $\nu_n = 0.49$, $H = 10\,\mu m$, $R_n = 1\,\mu m$, $r_e = \lambda_p \times 5\,\mu m$, $T = \lambda_p^2 \times 10\,nm$ 69

Figure 2.16 Normalized out of plane cell stiffness to the unstretched stiffness of the nucleus K_3/K_{30} vs prestretch λ_p with a specific choiche of the parameters: $\mu_m = 500\,Pa$, $\mu_n = 1000\,Pa$, $R_n = 500\,Pa$, $\nu_n = 0.49$, $H = 10\,\mu m$, $R_n = 1\,\mu m$, $r_e = \lambda_p \times 5\,\mu m$, $T = \lambda_p^2 \times 10\,nm$ 70

Figure 3.1 A schematic of cell center model depicting the arrangement of cells and the forces acting on them. (a) A 2-D monolayer of epithelial cells, confined inside a circular geometry is considered with cells represented as points at their center. (b) Delaunay triangulation (blue) has been used to model cell—cell connectivity, which finds the nearest neighbors of each point and form the connectivity array accordingly. Because of the greater clarity it affords and better connection with the experimental geometry, Voronoi tessellation (topological dual of Delaunay triangulation) is used for visualization of cells. 75

Figure 3.1 (c) When two originally connected cells move apart and form new neighbors, the connectivity of the system is updated using Delaunay triangulation. This connectivity update automatically takes T1 transitions into account. (d) Enlarged view of a representative cell i, along with its connection to neighboring cells. The position vector of this cell center is denoted by $\mathbf{r_i}$ and position vector of its j^{th} neighbor is denoted by $\mathbf{r_j}$. The blue arrow indicates the force, $\mathbf{F_{ij}}$ acting between cells i and j. The total force acting on i^{th} cell is the sum of the contributions from all the connecting neighbors. (e) The interaction between two adjacent cells is either compressive or tensile, depending upon the relative deformation of connecting spring with respect to its undeformed length, a_0. Here compressive and tensile stiffness of each spring is represented by kc and kt, respectively. While kc mimics the bulk cell stiffness, kt mimics cell-cell cohesivity. It is assumed that if the deformation of any spring is greater than d_{max}, the cell-cell connection is broken and there is no force transfer between these two cells. (f) Force acting on each cell is resolved along antiparallel ($\mathbf{F}_{||}$) and perpendicular($\mathbf{F}_{\perp}$) to the direction of the cell's polarization($\widehat{\mathbf{p}}$). Here $\mathbf{v}$ denotes the velocity vector on each particle. (g) Velocity profile in the direction of polarization as a function of $\mathbf{F}_{||}$. 76

Figure 3.2 Coherent rotation of cells on circular geometry. (a) The time evolution of polarization vector, $\widehat{\mathbf{p}}$ and velocity vector $\widehat{\mathbf{v}}$ is shown for $\xi = 0.1$. The evolution rule for polarization is chosen in such a way that, from an initial random orientation, $\widehat{\mathbf{p}}$ will try to orient along velocity vector with time. (b) The coordination between $\widehat{\mathbf{p}}$ and $\widehat{\mathbf{p}}$ is decided by the parameter ξ. The higher the value of ξ, higher is the tendency of $\widehat{\mathbf{p}}$ to orient along $\widehat{\mathbf{v}}$. The orientation of $\widehat{\mathbf{p}}$ and $\widehat{\mathbf{v}}$ at steady state for $\xi = 0.5$ and $\xi = 1$ are also shown. (c) Mean vorticity for systems with different $\xi = 0.5$ is plotted as a function of time. (d) The tendency of polarization vector to orient with velocity vector is shown by the plot between $\widehat{\mathbf{p}} \cdot \widehat{\mathbf{v}}$ and time. As the value of ξ increases, value of $\widehat{\mathbf{p}} \cdot \widehat{\mathbf{v}}$ approaches 1, indicating perfect alignment between two vectors. (e) A plot of velocity correlation length for varying system size shows that correlation length equal to the confinement size. (f) A plot of correlation function with time shows that the velocity correlation length increases with time, till the coherent rotation sets in. 78

Figure 3.4 **Cell crowding leads to fluidisation of tissue.** (a) The relationship between velocity and radial distance is examined for varying number density. Keeping the values of other parameters same as in previous simulations, the absolute velocity, $|v|$ averaged over time, after the system reaches steady state, is plotted as a function of radial distance for varying number of cells $N = 140, 150, 160, 170$. As the number density of system increases, the velocity-radial distance curve become less linear, indicating the presence of shear in the system. (b)Variation of principal shear strain rate along the radial distance plottedas a function of number density. Increase in shear rate with number density illustrates the fluidisation of tissue induced by cell density. (c) Vorticity of system decreases with increase in cell density.(d)Without considering the effect of contact inhibition, mean velocity of the system increases with number density. 81

Figure 3.6 **Cell motility dictates the fluidized behavior of tissue.** (a)Mean velocity for varying values of cell motility (v_0).(b)Normalized velocity-radial distance 82

Figure 3.8 **Tissue size, cell stiffness and cell cohesivity influence the fluid-like behavior of tissue.** (a)The relationship between velocity and radial distance is examined for three systems with varying radius, while keeping the number density approximately same for all. The number of cells in the systems are taken as $N = 1170, 520, 130$ for $R = 15, 10, 5$, respectively. The values of other parameters are chosen as that of the previous simulations. It is observed that, while keeping the number density constant, with increase in system size, the velocity versus radial-distance profile become less linear as more number of cells tend to move with a velocity comparable to v0; this shows the presence of shear strain rate in the system.(b)Increase in cell stiffness by increasing the value of compressive stiffness (k_c) of a system will make the system stiff and resulting rotational behavior will be more like a solid.(c) Reduction in cell cohesivity (k_t) leads to fluid-like tissue behavior. 84

Figure 3.10 **Cell stiffness and cohesivity dictate invasion pattern from coherent motion.** Three different systems of cells are taken with different stiffness of cell-cell connections. Simulations for (a) a soft system with $k_c = 1$ and $k_t = 1$; (b) a medium stiff system with $k_c = 10$ and $k_t = 1$; (c) stiff system with $k_c = 10$ and $k_t = 10$. The number of cells in all the three cases are same and equal to 100. After reaching a steady state of rotation, confinement was removed at time, $t = 50$. The snapshots of cell migratory patterns at $t = 55$ and $t = 60$ are also shown. For the case of intermediate stiff system, cells migrate in clusters compared to softer system where cell invasion pattern is more scattered. At the highest stiffness, cells continue to rotate even after removal of boundary. The length scale for each set of figure is shown below them. 86

Figure 3.12 Table of the parameters used by [78] and in the simulations. These are extimated from experiments or from simulaiton (see [78] for majior detail) 91

Figure 3.13 Preliminary results obtained with the parameters in Figure 3.12 in three diferent time istants. 91

Figure 3.14 Figure from the work by Doxzen et al. [35]. MCDK has been plated and cultured in a disk exhibiting collective co-rotational behavior. 92

Figure 4.1 **Depth of indentation for MCF10A cells in water**[50](A). Calculated reaction force–deformation curves for different parameter sets for Young's modulus of cytoplasm and nucleus (first and second value in parenthesis) for cell type MCF10A compared to reference curves from the literature (Li et al, 2008). (B) Displacements of the first three eigenforms for MCF7 and MCF10A cells in water. 94

Figure 4.2 Influence of (A) material properties (Young's modulus for cytoplasm and nucleus are as first and second value in parenthesis), (B) cell dimensions, (C) thickness of the actin cortex in percent of the cell radius, and (D) cell embedding (Young's modulus for agar in parenthesis) on natural frequencies of MCF10A cells (A) or MCF7 cells (A-D). 96

Figure 4.3 Harmonic vibration analysis of (A) MCF7 and (B) MCF10A cells (minimal sizes for both cell types) with external hydrostatic pressure in a frequency range of 20 kHz up to 60 kHz showing the displacement amplitudes. The red horizontal lines depict the maximum cell size which allows the amplitudes with the cell dimension to be compared. 97

Figure 4.4 **Increased death of MCF7 and MDA-MB-231 cells after irradiation with an ultrasonic frequency of** $24.5\,kHz$**.** (A) Cells either cultivated in 2D culture or (B) growing in 3D culture on alginate beads (gems) were treated with $24.5\,kHz$ and four different intensities for $4\,min$; $1\,h$ later the proportion of dead cells (propidium iodide (PI) positive cells) was determined by FACS analysis. Results represent the means of data from eight (A) or three (B) independent experiments; the error bars represent the standard errors; p-values were calculated by the two-sided, paired Student's t-test with * p<0.05, ** p<0.01. 98

Figure 4.5 **Decreased survival of MCF7 cells after irradiation with an ultrasonic frequency of** $24.5\,kHz$ **as determined by XCelligence (Roche).** 99

Figure 4.6 **Decreased survival of HL60 cells after fractionated irradiation.**HL60 suspension cells were treated by ultrasonic irradiation once, twice or three times at intervals of 3h (2x 3 h, 3x 3 h) or 6 h (2x 6 h). The number of vital cells was determined by FACS 1 h after each irradiation. (The number of vital cells of the untreated control was set as 100%.) Results represent the means of data fromthree independent experiments; the error bars represent the standard errors; p-values were calculated by the two-sided, paired Student's t-test with * p<0.05, ** p<0.01, *** p<0.001. 100

Figure 4.7 **Treatment of MCF7 cells with either (A) ultrasonic irradiation with 23.22 kHz and two different intensities ($0.3\,\mathbf{W/cm^2}$ or $1\,\mathbf{W/cm^2}$, dark grey bars), (B) paclitaxel with 100 nM or 200 nM (light grey bars) or (C) combinations of both treatments (ultrasonic irradiation followed by paclitaxel treatment; white bars) with a) constant concentration of paclitaxel and different intensities of ultrasonic irradiation, and b) constant intensity and different concentrations of paclitaxel.**Results represent the means of data from eight independent experiments; the error bars represent the standard errors; p-values were calculated by the two-sided, paired Student's t- test with * p<0.05, ** p<0.01, *** p<0.001. 101

Figure 4.8 a) Mach-Zehnder setup for digital holographic microscopy in transmission mode. Laser: laser light source (λ=488nm); O: object wave; R: reference wave; BS1, BS2: non-polarizing beam splitter cubes; M: mirror; AFS Module: sample holder and ultrasound generator; MO: microscope lens; Camera: hologram recording device (CMOS image sensor); PC: computer. b) Detailed structure of the flow cell, consisting of two glass plates with a fluid chamber in between. For the ultrasound generation, a piezo plate is attached to the upper glass slide and connected to a signal generator. 105

Figure 4.9 Primary radiation forces simulated profile inside the microchannel. The forces are generated by a driving signal with frequencies of $14.11MHz$ (green) and $7.04MHz$ (blu), and amplitude $V = 7Vpp$. The corresponding nodal planes (N) and the initial plane are highlighted. 106

Figure 4.10 a) Changes in the particle's axial position upon application of two resonant frequencies, $7.04 MHz$ and $14.11 MHz$, as reconstructed from the numerical refocusing of the holographic video. The three images in the left are the recorded holograms where the axial movement is clearly detectable b) Schematic depiction of the changes in the microspheres height. 108
Figure 4.11 Four amplitude reconstructions of the holographic sequence. The red boxes highlight the results of the ROI extraction method where the estimated number of microspheres for the detected cluster is calculated. 109
Figure 4.12 Estimation of (a) the number of clusters of microspheres in time and (b) the number of microspheres per cluster in time. 110

LIST OF TABLES

Table 1 Transformation for Kinematic tensors for rigid-body rotations in reference and current frames 6
Table 2 Transformation rule for Stress measures tensors for rigid-body rotations in reference and current frames 12
Table 3 Synoptic frame illustrating how to set the parameters characterizing the proposed generalized quasi-standard linear Kelvin viscoelastic model, in order to replicate Elastic, Viscous, Voigt (V), Maxwell (M) and standard linear Kelvin (SLK) limit cases, as well as the three intermediate chosen configurations, say SLK_1, SLK_2 and SLK_3, employed to perform the subsequent analyses. 35
Table 4 Actual stiffness for different lines of healthy and cancer cells, measured by means of several techniques, as precised in the references reported in the first column. 48

1

MEACHANICAL FRAMEWORK

In this chapter, the fundamentals of continuum mechanics are recalled, with specific attention to the formulas and methods nedded to follow the PhD Thesis issues. Additionally, essential concepts of classical and fractional viscoelasticity have been also introduced. The interested reader will find more details obout continuum mechanics in the work by Gurtin, Ogden, Holzapfel, Bigoni, Cowin. [6, 20, 54, 55, 61]. Viscoelasticity can be instead deepened in books by Tschoegl, Samko, Cottone [18, 117, 127].

About the notation, vectors in the Euclidean $\mathbb{R}^3$ are indicated by boldface lower-case letters $(\mathbf{a},\mathbf{b},...)$ and second order tensors with upper boldface letters $(\mathbf{A},\mathbf{B},...)$. The classical *continuum hypothesis* for which the body $\mathscr{B}$ occupies densely the space $\mathbb{R}^3$ is used, hence the existence of a strictly positive continuous *density* function $\rho(\mathbf{x})$, for any $\mathbf{x} \in \Omega$, has been postulated.

1.1 KINEMATICS

Let us consider a body $\mathscr{B}$ that occupies densely a subset of the Euclidean space. An arbitrary configuration is chosen as a *reference* configuration, denoted by Ω_0, for which the body is considered in a undeformed state. During the motion a change in configuration could occur and so a new region of the space Ω, the so-called *current* configuration, is occupied.

Two different coordinates systems (COOS), that is the *reference frame* with fixed origin $\mathbf{O}$ and orthonormal basis vector $\mathbf{E_I}\,(I=1,2,3)$, and the *current frame* with basis $\mathbf{e}_i\,(i=1,2,3)$ and origin $\mathbf{o}$ are introduced. As well-known, problems in continuum mechanics may be formulated either using the so-called *Lagrangian (or material) description*, i. e. referring everything w.r.t. the reference frame and so using the reference position $\mathbf{X}$ as independent variable, or using the so-called *Euelerian (or spatial) description*, i. e. referring everything w.r.t. the current frame and considering the current position $\mathbf{x}$ as independent variable. Capitol and lower letters notation are used referring to the material and spatial description,

respectively. The Einstein summation convention of the repeated indexes is used.
The change in configuration is due by the *motion* (**u**) defined as follows

$$\mathbf{u} = \mathbf{x} - \mathbf{X}, \tag{1.1}$$

being **X** the *material* (or *Lagrangian*) description for the position of a point in the reference configuration and **x** the corresponding *current* (*Eulerian*) position of the same point in the current configuration.
The current position is *mapped* by a bijective so-called *deformation* function ($\chi : \Omega_0 \rightarrow \Omega$) $\mathbf{x} = \chi(\mathbf{X})$, assumed to be sufficiently regular; $\mathbf{X} = \chi^{-1}(\mathbf{x})$ describes the inverse mapping.
In order to analyze the deformation locally, i.e. in a neighborhood of a material particle, it is possible to consider the differential of the deformation mapping $dx_i = \frac{\partial \chi_i}{\partial X_J} dX_J$ which is possible to write as follows in a compact way

$$\mathbf{dx} = \mathbf{FdX} \tag{1.2}$$

where the second order tensor **F** is the *deformation gradient* or the gradient of the deformation mapping with respect the material coordinates, i.e.

$$\mathbf{F} = Grad\chi(X) \equiv \nabla_X \otimes \chi(X) = \mathbf{I} + \nabla_X \otimes u(X). \tag{1.3}$$

The gradient of the inverse motion $\chi^{-1}(\mathbf{x})$ corresponds to the inverse of the deformation gradient F^{-1} defined as follows

$$F^{-1} = grad\chi^{-1}(x) \equiv \nabla_x \otimes \chi^{-1}(x) \tag{1.4}$$

In the equations (1.3) and (1.4) *Grad* and ∇_X symbols denote gradient operation with respect the reference frame and to distinguish from *grad* or ∇_x symbols that are gradients taken with respect the current reference frame. $\mathbf{u}(\mathbf{X})$ and $\mathbf{u}(\mathbf{x})$ are the two different descriptions of the displacement field.
F and $\mathbf{F}^{-1}$ are *two-point tensors* that map the material fiber (**dX**) in spatial fiber (**dx**) and vice versa respectively. The representations of **F** and $\mathbf{F}^{-1}$ with respect to the bases previously introduced are the following

$$\mathbf{F} = F_{iJ} e_i \otimes E_J \quad \text{and} \quad \mathbf{F^{-1}} = F_{Ij}^{-1} E_I \otimes e_j \tag{1.5}$$

where the mixed nature of $F_{iJ} e_i = \partial x_i / \partial X_J$ and $F_{Ij}^{-1} = \partial X_I / \partial x_j$ is highlighted.
For the physical meaning associated with the relationship (1.2) $J = detF >$

0. In particular J assumes the physical meaning of the changing in volume of the neighborhood of X during the deformation, being J the determinant of the Jacobian matrix, i.e.

$$dv = JdV \tag{1.6}$$

being dV and dv the elementary volume in the reference and current configuration. $J = 1$ means that the transformation is *isochoric* and if it happens for all the possible deformations implies that the material is *incompressible*.

Furthermore, considering the infinitesimal vector area $\mathbf{dA} = \mathbf{N}dA$ with normal $\mathbf{N}$ and centered in the reference position $\mathbf{X}$ in Ω_0, it will be transformed in the current infinitesimal vector area $\mathbf{da} = \mathbf{n}da$ with normal $\mathbf{n}$ and centered in the current position $\mathbf{x}$ in Ω by means the deformation gradient $\mathbf{F}$ following the so-called *Nanson's formula*

$$\mathbf{n}da = J\mathbf{F}^{-\mathbf{T}}\mathbf{N}dA \tag{1.7}$$

It is worth to highlight that the deformation gradient incorporates both the change in orientation (rotation) and in elongation (stretch) that the material fibers $\mathbf{dX}$ undergo during the deformation. To *uncouple* this two different effects the *polar decomposition theorem* is used. In fact, given a second order tensor $\mathbf{F}$ there exist two symmetric and positive definite tensors, $\mathbf{U}$ and $\mathbf{V}$, and a unique orthogonal *rotational* tensor $\mathbf{R}$ ($\mathbf{R}\mathbf{R}^\mathbf{T} = \mathbf{I} = \mathbf{R}^\mathbf{T}\mathbf{R}$, $det\mathbf{R} = +1$) such that

$$\mathbf{F} = \mathbf{RU} = \mathbf{VR} \tag{1.8}$$

being $\mathbf{R}$ a two-point tensor, while $\mathbf{U}$ and $\mathbf{V}$ are the *right* and *left stretch tensors* respectively given by

$$\mathbf{U} = \left(\mathbf{F}^\mathbf{T}\mathbf{F}\right)^{1/2}, \mathbf{V} = \left(\mathbf{F}\mathbf{F}^\mathbf{T}\right)^{1/2} \tag{1.9}$$

Using the spectral decomposition it is possible to explicit in a diagonal form the stretch tensors as follows

$$\mathbf{U} = \lambda_I \bar{\mathbf{E}}_\mathbf{I} \otimes \bar{\mathbf{E}}_\mathbf{I}, \quad \text{and} \quad \mathbf{V} = \lambda_i \bar{\mathbf{e}}_\mathbf{i} \otimes \bar{\mathbf{e}}_\mathbf{i} \tag{1.10}$$

where $\bar{\mathbf{E}}_\mathbf{I}$ and $\bar{\mathbf{e}}_\mathbf{i}$ are the eigenvectors, the *principal directions*, in the reference and current frames respectively; instead $\lambda_I = \lambda_i$ are the eigenvalues or *principal stretches*, which assume the physical meaning of changes in length of the material or spatial fiber in the principal directions. As shown by eqn. (1.10) $\mathbf{U}$ *lives* and *acts* in the reference frame, namely maps a vector living in the reference frame Ω_0 into itself, $\mathbf{V}$ doing the same in Ω.

In this framework the deformation gradient, through the polar decomposition, can be seen as acting on a generic vector in two different substeps. Considering the right decomposition a stretching in the reference frame is followed by the rotation which causes the changing from reference frame to current frame, while considering the left decomposition, a change of reference frame is followed by a stretching in the current frame.

Polar decomposition of $\mathbf{F}$ and the spectral decomposition of $\mathbf{U}$ and $\mathbf{V}$ give $J = det\mathbf{F} = det\mathbf{U} = det\mathbf{V}$ (since $det\mathbf{R} = 1$) in terms of the principal stretches

$$J = \lambda_1 \lambda_2 \lambda_3. \tag{1.11}$$

Furthermore, the second order tensors

$$\mathbf{C} = \mathbf{F^T F} = \mathbf{U^2} \quad \text{and} \quad \mathbf{B} = \mathbf{F F^T} = \mathbf{V^2} \tag{1.12}$$

are the *right* ($\mathbf{C}$) and *left (*$\mathbf{B}$*) Cauchy stretch tensors* following the same properties of $\mathbf{U}$ and $\mathbf{V}$ respectively, except for the fact that in the spectral decomposition the eigenvalues appear squared. The stretch tensors $\mathbf{C}$ and $\mathbf{B}$ provide local measures of the deformation since, as above highlighted (eqns. 1.10 and 1.12) their principal components represent the stretch of three orthogonal fibers, aligned with the eigenvectors. Therefore, all the tensors $\mathbf{C}, \mathbf{B}, \mathbf{U}$ and $\mathbf{V}$ can be chosen to quantify the strain. Worthily a strain measure must exclude rigid rotation and translations because does not produce actual deformations. In this perspective there are infinite possibilities of choices, collected in Lagrangian and Eulerian strain measures as follows

$$\mathbf{E^{(m)}} = \begin{cases} \frac{\mathbf{U^{(m)}} - I}{m} \, \text{for} \, m \neq 0 \\ \log \mathbf{U} \, \text{for} \, m = 0 \end{cases} \quad , \quad \mathbf{G^{(m)}} = \begin{cases} \frac{\mathbf{V^{(m)}} - I}{m} \, \text{for} \, m \neq 0 \\ \log \mathbf{V} \, \text{for} \, m = 0 \end{cases} \tag{1.13}$$

being m an integer. For the special case of $m = 0$, the *Hencky strain* measure, the logarithm of a tensor is defined for symmetric positive definite tensors taking the logarithm of the eigenvalues ($\varepsilon_i = \log \lambda_i$) in its spectral decomposition or the so-called *true strain*. When $m = 2$, $\mathbf{E}^{(2)}$ and $\mathbf{G}^{(2)}$ are the *Green Lagrange* strains that from eqn. (1.12) and (1.3) one has

$$\begin{aligned} \mathbf{E}^{(2)} &= \frac{1}{2}\left[\nabla_X \mathbf{u} + (\nabla_X \mathbf{u})^T + \nabla_X \mathbf{u}\,(\nabla_X \mathbf{u})^T\right] \quad \text{and} \\ \mathbf{G}^{(2)} &= \frac{1}{2}\left[\nabla_x \mathbf{u} + (\nabla_x \mathbf{u})^T + \nabla_x \mathbf{u}\,(\nabla_x \mathbf{u})^T\right] \end{aligned} \tag{1.14}$$

When the displacement field is infinitesimal, the material description $\mathbf{U}$ coincides with the spatial description $\mathbf{u}$ and the second-order terms in (1.14) can be neglected and so $\mathbf{E}^{(2)} \simeq \mathbf{G}^{(2)} \simeq \mathbf{E}$, being $\mathbf{E} = \frac{1}{2}(\nabla \mathbf{u} + (\nabla \mathbf{u})^T$ the infinitesimal strain.

Rigid-body rotation in reference and current configuration: transformation of the kinematic tensors

It will be considered, here, the effect of rigid-body rotations, represented by a tensor $\mathbf{Q} \in Orth^+$ applied in the reference configuration or in the current configuration to the kinematic tensors.
If the rotation is applied in the reference configuration as reference frame can be chosen Ω_0 or Ω_0^* in which the difference is a rigid-body rotation. A vector $\mathbf{w}$ living in the current configuration can be seen, following Equation (1.2), either as result of

$$\mathbf{w} = \mathbf{F}\mathbf{w_0} \quad \text{or} \quad \mathbf{w} = \mathbf{F}^*\mathbf{w_0^*}, \tag{1.15}$$

being $\mathbf{F}$ and $\mathbf{F}^*$ the two deformation gradients relative to the two reference configurations Ω_0 and Ω_0^* respectively, $\mathbf{w_0}$ and $\mathbf{w_0^*} = \mathbf{Q}\mathbf{w_0}$ the vector $\mathbf{w}$ seen in the two reference frames. Thus one has the deformation gradient relative the rotated configuration as follows

$$\mathbf{F}^* = \mathbf{F}\mathbf{Q}^{\mathbf{T}} \tag{1.16}$$

Considering now a rigid body rotation in the spatial configuration, one can consider two different current frames Ω and Ω^*. The Eulerian vector $\mathbf{w}$ differs from its representation in the rotated frame ($\mathbf{w}^* = \mathbf{Q}\mathbf{w}$) and since Equation (1.15) holds true, between the two deformation gradients when a rotation is applied in the current configuration the following relationship is found

$$\mathbf{F}^* = \mathbf{Q}\mathbf{F} \tag{1.17}$$

From Equations (1.16) and (1.17), when a rigid-body transformation is applied in the reference or current frame the relationship between the

"Rotated" tensor	Rigid-body rotation in the reference frame $(\Omega_0 \rightarrow \Omega_0^*)$	Rigid-body rotation in the current frame $(\Omega \rightarrow \Omega^*)$
$\mathbf{F}^*$	$\mathbf{FQ^T}$	$\mathbf{QF}$
$\mathbf{R}^*$	$\mathbf{RQ^T}$	$\mathbf{QF}$
$\mathbf{U}^*$	$\mathbf{QUQ^T}$	$\mathbf{U}$
$\mathbf{V}^*$	$\mathbf{V}$	$\mathbf{QVQ^T}$
$\mathbf{C}^*$	$\mathbf{QCQ^T}$	$\mathbf{C}$
$\mathbf{B}^*$	$\mathbf{B}$	$\mathbf{QBQ^T}$
$\mathbf{E^{(m)*}}$	$\mathbf{QE^{(m)*}Q^T}$	$\mathbf{E^{(m)*}}$
$\mathbf{G^{(m)*}}$	$\mathbf{G^{(m)*}}$	$\mathbf{QG^{(m)*}Q^T}$

Table 1: Transformation for Kinematic tensors for rigid-body rotations in reference and current frames

tensor $\mathbf{C}^*$, $\mathbf{U}^*$, $\mathbf{E}^{(\mathbf{m})*}$, $\mathbf{B}^*$, $\mathbf{V}*$, and $\mathbf{G}^{(\mathbf{m})*}$ and their unrotated counterparts are reported in the Table 1, where is possible to better recognize the Lagrangian, Eulerian or two-point nature of the kinematic tensors. In fact, a purely material tensor ($\mathbf{C}, \mathbf{U}$ and $\mathbf{E}^{(\mathbf{m})}$) is not affected by the transformations in the spatial configuration; on the contrary, a purely spatial tensor ($\mathbf{B}, \mathbf{V}$ and $\mathbf{G}^{(\mathbf{m})}$) is not affected by the transformations in the material configuration. A two-point tensor ($\mathbf{F}, \mathbf{R}$), finally, is always influenced by both material and spatial rotation.

The dependence on time and some time derivations

For sake of simplicity up to here it has not been considered the dependence on time of the mapping $\mathbf{x} = \chi(\mathbf{X}, t)$, namely the current configuration Ω_t is actually dependent from the instant t. Since the mapping is invertible as above highlighted is possible to use indifferently both the material and spatial description of the *motion*. It is, thus, possible to introduce the *material description of the velocity*, as follows

$$\mathbf{v}(\mathbf{X}, t) \triangleq \frac{\partial \chi(\mathbf{X}, t)}{\partial t}. \tag{1.18}$$

In a similar way, it is possible to introduce the *spatial description of the velocity*, as follows

$$\mathbf{v}(\mathbf{x}, t) \triangleq \frac{\partial \chi(\chi^{-1}(\mathbf{x}, t), t)}{\partial t}. \tag{1.19}$$

More generally, for a generic field f the time derivative depends on the description used. In fact the *Material time derivative*, here indicated by

$\frac{D\square}{Dt}$ or $\dot{\square}$ of a materially described field $f(\mathbf{X},t)$ is the time derivative with the position $\mathbf{X}$ held fixed, namely

$$\dot{f}(\mathbf{X},t) = \frac{Df(\mathbf{X},t)}{Dt} = \frac{\partial f(\mathbf{X},t)}{\partial t} \text{ holding } \mathbf{X} \text{ fixed.} \tag{1.20}$$

The *Spatial time derivative*, here indicated by $\frac{d\square}{dt}$ or $\square'$ of a spatially described field $f(\mathbf{X},t)$ is the time derivative with the position $\mathbf{x}$ held fixed, namely

$$f'(\mathbf{x},t) = \frac{df(\mathbf{x},t)}{dt} = \frac{\partial f(\mathbf{x},t)}{\partial t} \text{ holding } \mathbf{x} \text{ fixed} \tag{1.21}$$

Finally, to compute the material time derivative of a spatially described field $f(\mathbf{x},t)$, one must first convert its description to material $\mathbf{X} = \chi^{-1}(\mathbf{x},t)$, take its (material) time derivative using the chain rule, and then convert the result back to spatial, obtaining

$$\dot{f}(\mathbf{x},t) = \frac{Df(\mathbf{x},t)}{Dt} = grad\, f(\mathbf{x},t) \cdot \mathbf{v}(\mathbf{x},t) + \frac{\partial f(\mathbf{x},t)}{\partial t}. \tag{1.22}$$

Note that in the Equation (1.22) the "essence" (scalar, vector, second order tensor, etc) of the field f must to be taken into account, when the gradient and the associated meaning of the inner product $(grad\, f(\mathbf{x},t) \cdot \mathbf{v}(\mathbf{x},t))$ are considered.
Considering, for example, the material time derivative of the spatial description of the velocity field $\mathbf{v}(\mathbf{x},t)$; one obtains

$$\dot{\mathbf{v}} = \mathbf{L}\mathbf{v} + \frac{\partial \mathbf{v}}{\partial t} \tag{1.23}$$

where

$$\mathbf{L} = grad\mathbf{v} \tag{1.24}$$

is the spatial tensor *velocity gradient* that maps spatial vector in spatial vector and the meaning of the operation $\mathbf{Lv}$ has to be considered as the action of the tensor field $\mathbf{L}$ to the vector field $\mathbf{v}$. An additive decomposition in its symmetric and skew-symmetric part allows to introduce the stretching ($\mathbf{D}$) and the spin ($\mathbf{W}$) tensors as follows

$$\mathbf{D} = \frac{\mathbf{L} + \mathbf{L}^{\mathrm{T}}}{2} \qquad \mathbf{W} = \frac{\mathbf{L} - \mathbf{L}^{\mathrm{T}}}{2} \tag{1.25}$$

Considering the chain-rule the material time derivative of the (material field) gradient of the deformation is thus

$$\dot{\mathbf{F}}(\mathbf{X},t) = Grad\dot{\chi}(\mathbf{X},t) = \mathbf{L}_m\mathbf{F} \tag{1.26}$$

being $\mathbf{L}_m = \mathbf{L}\big|_{\mathbf{x}=\chi(\mathbf{X},t)}$ the material description of the spatial tensor velocity gradient. The Equation (1.26) is the *evolution rule* for the deformation gradient that can be inverted providing an alternative way to find the material description of the velocity gradient, i. e.

$$\mathbf{L}_m = \dot{\mathbf{F}}\mathbf{F}^{-1} \tag{1.27}$$

1.2 CONCEPT OF STRESS AND BALANCE OF LINEAR AND ANGULAR MOMENTA

In this section the balance laws governing the dynamical equilibrium are introduced. Considering a body Ω in the current configuration, two possible actions can occur: *traction* $\mathbf{t}$ or contact forces, namely force per unit surface, and *body forces* $\mathbf{b}$ or mass forces, namely force per unit volume. If the equilibrium holds the balance of linear and angular momentum laws must be satisfied for any portion $\mathscr{P}$ of the body Ω, i. e.respectively

$$\int_{\mathscr{P}} \mathbf{b}\,dv + \int_{\partial\mathscr{P}} \mathbf{t}\mathbf{n}ds = \int_{\mathscr{P}} \rho\dot{\mathbf{v}}\,dv, \tag{1.28}$$

$$\int_{\mathscr{P}} (\mathbf{x}-\mathbf{o})\times\mathbf{b}\,dv + \int_{\partial\mathscr{P}} (\mathbf{x}-\mathbf{o})\times\mathbf{t}\mathbf{n}ds = \int_{\mathscr{P}} \rho(\mathbf{x}-\mathbf{o})\times\dot{\mathbf{v}}\,dv \tag{1.29}$$

If Ω is in equilibrium when a cut is performed in the body though a plane π at the point $\mathbf{x}$ with unit normal $\mathbf{n}$, the two parts of the body are not in equilibrium anymore if one does not consider, following the action-reaction principle, the interactions $\mathbf{t}$ transmitted between the two surfaces. Following the so-called Cauchy theorem the interaction is a linear function of the unit normal $\mathbf{n}$ to the surface π at $\mathbf{x}$ through a second order (spatial)tensor taken as measure of the actual stress in the current configuration, the *Cauchy stress tensor* $\mathbf{T}(\mathbf{x})$, namely,

$$\mathbf{t}(\mathbf{x},\mathbf{n}) = \mathbf{T}(\mathbf{x})\mathbf{n} \tag{1.30}$$

The components $T_{ij}(\mathbf{x})$ of the Cauchy stress tensor are the actual measure of the stresses at the point $\mathbf{x}$ lying in the surface with normal i and directed along j.

Substituting eqn. (1.30) into Equations (1.28) and (1.29) considered for any portion P of Ω by means the Cauchy divergence theorem one can obtain the *indefinite equations of (local)equilibrium*

$$div\mathbf{T} + \mathbf{b} = \rho\mathbf{v} \tag{1.31}$$

$$\mathbf{T} = \mathbf{T}^T \tag{1.32}$$

The equilibrium in current configuration can be ensured by means of Equations (1.28) and (1.29) or locally by Equations (1.31) and (1.32), regardless the deformations (the kinematics) experienced by the body as a consequence of the application of the external action; to consider the balance law in the reference frame a so-called *Pull-Back* operation is needed according to the kinematic for which it is possible to map from $\mathscr{P} \in \Omega \to \mathscr{P}_0 \in \Omega_0$ and thus, making a change in variables and also considering Equations (1.6), (1.7) and (1.30), the balance of linear momentum becomes

$$\int_{\mathscr{P}_0} \mathbf{b} J\, dV + \int_{\partial \mathscr{P}_0} J\mathbf{T}\mathbf{F}^{-\mathbf{T}}\mathbf{N}\, dS = \int_{\mathscr{P}_0} \rho \mathbf{v}(\dot{\mathbf{X}}) J\, dV. \tag{1.33}$$

Applying the divergence theorem, since the Equation (1.33) must to be satisfied $\forall \mathscr{P}_0 \in \Omega_0$, the equations of equilibrium in the reference frame become

$$Div\,\mathbf{P} + \mathbf{b_0} = \rho_0 \dot{\mathbf{V}} \tag{1.34}$$

where $\mathbf{b_0} = J\mathbf{b}$ is the body forces evaluated in the reference frame and ρ_0 is the density in the reference configuration, while

$$\mathbf{P} = J\mathbf{T}\mathbf{F}^{-\mathbf{T}} \tag{1.35}$$

is the *Nominal Stress* or *first Piola-Kirchhoff stress tensor*. As $\mathbf{F}$ is a two-point tensor, considering the local (spatial)load $\mathbf{df}$ on the element surface $\mathbf{n}da$ can be obtained also considering the reference frame as follows

$$\mathbf{df} = \mathbf{Tn}da = \mathbf{PN}dA \tag{1.36}$$

so it transforms element area in the reference frame $\mathbf{N}dA$ in the infinitesimal load $\mathbf{df}$ in the current configuration. With the position (1.35) the reference version of the Cauchy theorem takes the form

$$\mathbf{PN} = \mathbf{t_0}, \tag{1.37}$$

being $\mathbf{t}_0$ the *nominal traction* (traction in the reference configuration). Note that, by introducing the so-called *Kirchhoff* stress,

$$\mathbf{K} = J\mathbf{T} \tag{1.38}$$

one has that $\mathbf{T} = J^{-1}\mathbf{P}\mathbf{F}^{\mathbf{T}}$; the Piola stress tensor is thus in general not symmetric because $\mathbf{F}$ is non symmetric, but from Equation (1.32) the following relationship holds true

$$\mathbf{P}\mathbf{F}^{\mathbf{T}} = \mathbf{F}\mathbf{P}^{\mathbf{T}}. \tag{1.39}$$

1.3 WORK CONJUGATE

In this section the balance of the mechanical energy principle is presented. A consequence of this principle is the concept of *work conjugate* for which is possible to establish a conjugation among stress and stain measures.
The balance of mechanical energy formulated in terms of power is

$$P_{int} + \frac{dK(t)}{dt} = P_{ext} \tag{1.40}$$

being P_{int} the internal stress power, $K(t)$ the kinetic energy and P_{ext} the power provided by the external loading. The Equation (1.40) can be expressed either in Eulerian or Lagrangian forms. With reference the spatial description the three terms are derived taking the scalar product of Equation (1.28) with the spatial velocity $\mathbf{v}(\mathbf{x})$ and thus take the form

$$K(t) = \frac{1}{2}\int_{\Omega} \rho\, |\mathbf{v}|^2\, dv \tag{1.41}$$

$$P_{int}(t) = \int_{\Omega} \mathbf{T}\cdot\mathbf{L}\, dv = \int_{\Omega} \mathbf{T}\cdot\mathbf{D}\, dv \tag{1.42}$$

$$P_{ext}(t) = \int_{\Omega} \mathbf{b}\cdot\mathbf{v}\, dv + \int_{\partial\Omega} \mathbf{t}\cdot\mathbf{v}\, ds \tag{1.43}$$

Considering the internal power one infers that the Cauchy stress tensor $\mathbf{T}$, since is symmetric, is conjugated with the stretching tensor $\mathbf{D}$. For sake of clarity here one can consider quasi- static problem for which the *internal Energy* Ψ confirms that the Cauchy stress tensor is conjugated, with the symmetric part of the gradient of the Eulerian displacement $\mathbf{u}(\mathbf{x})$

$$\Psi = \mathbf{T}\cdot\nabla_{\mathbf{x}} \otimes \mathbf{u} \tag{1.44}$$

Focusing the attention to the internal power, it can be expressed also in the reference configuration, making a change of domain and of variables, taking into account the property of three second order tensors $(\mathbf{A},\mathbf{B},\mathbf{C})$ that is $\mathbf{A}\cdot\mathbf{B}\mathbf{C} = \mathbf{A}\mathbf{C}^{\mathbf{T}}\cdot\mathbf{B}$, the Equations (1.27) and (1.35), Equation (1.42) becomes

$$\int_{\Omega} \mathbf{T}\cdot\mathbf{D}\, dv = \int_{\Omega_0} \mathbf{K_0}\cdot\mathbf{D_0}\, dV \int_{\Omega_0} \mathbf{P}\cdot\dot{\mathbf{F}}\, dV \tag{1.45}$$

being $\mathbf{K}_0$ and $\mathbf{D}_0$ the Lagrangian description of the Kirchhoff stress and the stretching respectively.

From Equation (1.45) one deduces that the first Piola-Kirchhoff stress is conjugate to the time derivative of the gradient of the deformation, the material description of the Kirchhoff stress is conjugate with the material description of the stretching and also the following equality arises

$$\mathbf{K_0} \cdot \mathbf{D_0} = \mathbf{P} \cdot \dot{\mathbf{F}} \tag{1.46}$$

The quasi static version of Equation (1.46) shows that the $\mathbf{K}_0$ is conjugate with the $\nabla_{\mathbf{X}} \otimes \mathbf{u}$ and the $\mathbf{P}$ stress with $\mathbf{F}$, i. e.

$$\Psi = \mathbf{K_0} \cdot \nabla_{\mathbf{X}} \otimes \mathbf{u} \tag{1.47}$$

In this framework, it is possible to define several tensor pairs that have the property that their dot product gives the rate of internal mechanical work per unit reference volume. In particular, choosing a suitable strain measure, the conjugate stress can be obtained through the definition (1.46). For instance, a family of symmetric Lagrangian and Eulerian stress tensors $\mathbf{T}^{(h)}$ and $\mathbf{Z}^{(h)}$ can be defined as the conjugates of the strain tensors $\mathbf{E}^{(h)}$ and $\mathbf{G}^{(h)}$ in Equation (1.13), respectively by

$$\mathbf{Z}^{(h)} \cdot \frac{D\mathbf{G}}{Dt}^{(h)} = \mathbf{K_0} \cdot \mathbf{D_0} = \mathbf{P} \cdot \dot{\mathbf{F}} = \mathbf{P} \cdot \frac{D\mathbf{F}}{Dt} = \mathbf{T}^{(h)} \cdot \frac{D\mathbf{E}}{Dt}^{(h)} \tag{1.48}$$

A special case is the *Second Piola-Kirchhoff stress tensor* $\mathbf{T}^{(2)}$ that is conjugated with the Green-Lagrange strain; from Equation (1.48) one has

$$\mathbf{T^{(2)}} = \mathbf{F^{-1}K_0F^{-T}} = \mathbf{F^{-1}P} \tag{1.49}$$

Rigid-body rotation in reference and current configuration: transformation of the stress tensors

To better understand the material or spatial nature of the stress measures above introduced, let us consider the effects of a rigid-body rotation, by means (as mentioned in the case of transformation of the kinematic tensor Section 1.1) a rotation tensor $\mathbf{Q} \in Orth^{+}$, applied in the reference or current frame.

If the rotation is applied in the current configuration $\Omega*$ the unit normal $\mathbf{n}^*$ to a generic point $\mathbf{x}^*$ and stress vector $\mathbf{t}^*$ can be obtained from the corresponding unrotated vector via

$$\mathbf{n}^* = \mathbf{Qn}, \quad \mathbf{t}^* = \mathbf{Qt} \tag{1.50}$$

By means the Cauchy theorem (Equation (1.30)) one can obtain the relationship between the *true stress* in the rotated frame and the corresponding in Ω showing the Eulerian nature of the Cauchy stress measure

$$\mathbf{T}^{*} = \mathbf{QTQ}^{\mathbf{T}} \tag{1.51}$$

Moreover with reference to the relationship between **P** and **T** (Equation (1.35)) and the transformation rules summarized in Table 1, one deduces the two-point nature, as **F**, of the first Piola-Kirchhoff stress measure; in fact, the rigid-body rotation in the current frame acts as follows

$$\mathbf{P}^{*} = \mathbf{QP} \tag{1.52}$$

Similarly, with reference to Equation (1.49) one can obtain the transformation rule for the Lagrangian second Piola-Kirchhoff stress measure and generalize it for each Lagrangian and Eulerian stress measure defined by Equation (1.48) as follows

$$\mathbf{T}^{(\mathbf{2})*} = \mathbf{T}^{(\mathbf{2})}, \quad \mathbf{T}^{(\mathbf{m})*} = \mathbf{T}^{(\mathbf{m})} \tag{1.53}$$

$$\mathbf{Z}^{(\mathbf{m})*} = \mathbf{QZ}^{(\mathbf{m})}\mathbf{Q}^{\mathbf{T}} \tag{1.54}$$

With respect to a rigid rotation in reference configuration one can obtain the transformation rules verifying that the stress power, Equation (1.48), *is independent from rigid-body rotations* of the reference and current configuration (some time it is called *objective*). The relationship between transformed strain tensors and their corresponding stress tensors are summarized in Table 2 for both rigid-body rotation in reference and current frames, where it is possible to better recognize the Lagrangian, Eulerian or two-point nature of the various stress measures.

"Rotated" tensor	Rigid-body rotation in the reference frame $(\Omega_0 \rightarrow \Omega_0^*)$	Rigid-body rotation in the current frame $(\Omega \rightarrow \Omega^*)$
$\mathbf{P}^*$	$\mathbf{PQ}^{\mathbf{T}}$	$\mathbf{QP}$
$\mathbf{T}^*$	$\mathbf{T}$	$\mathbf{QTQ}^{\mathbf{T}}$
$\mathbf{T}^{(\mathbf{m})*}$	$\mathbf{QT}^{(\mathbf{m})*}\mathbf{Q}^{\mathbf{T}}$	$\mathbf{T}^{(\mathbf{m})*}$
$\mathbf{Z}^{(\mathbf{m})*}$	$\mathbf{Z}^{(\mathbf{m})*}$	$\mathbf{QZ}^{(\mathbf{m})*}\mathbf{Q}^{\mathbf{T}}$

Table 2: Transformation rule for Stress measures tensors for rigid-body rotations in reference and current frames

1.4 CONSTITUTIVE EQUATION: ISOTROPIC NON-LINEAR HYPERELASTICITY

In the previous sections the fundamental equations to characterize the kinematics, stresses and balance equations have been introduced. These equations hold for any continuum body, but are not sufficient *to close the problem of the mechanical equilibrium*, consisting in the finding of the components of the displacement field ($\mathbf{u}$) and the components of the stress field (for example $\mathbf{T}$) for each point of the body. *Constitutive laws*, must be established to specialize the problem of the mechanical equilibrium for the body at hand, that in general enables to express the stress in terms of the other field functions such as strain measure and vice-versa. In this section the isotropic homogeneous (in which the distribution of the internal constituents are assumed to be uniform) hyperelasticity of continuum (solid) media has been considered within non linear regime. A solid is called *hyperelastic* if a scalar *strain energy density function* Ψ - the so-called *Helmholtz free-energy function*- there exists, depending solely on the state of the deformation identified by the deformation gradient $\mathbf{F}$ such that one obtains the first Piola-Kirchhoff stress tensor $\mathbf{P}$ (the stress conjugate to deformation gradient) as follows

$$\mathbf{P} = \frac{\partial \Psi(\mathbf{F})}{\partial \mathbf{F}}, \tag{1.55}$$

and using the Equation (1.35) the symmetric Cauchy (true)stress can be obtained from the Equation (1.55) as follows

$$\mathbf{T} = J^{-1}\frac{\partial \Psi(\mathbf{F})}{\partial \mathbf{F}}\mathbf{F}^T = J^{-1}\mathbf{F}\left(\frac{\partial \Psi(\mathbf{F})}{\partial \mathbf{F}}\right)^T. \tag{1.56}$$

The strain energy density function has the property to be poly-convex, in fact the global existence theory of the solution of the problem of mechanical equilibrium is based on this property. Moreover, the function Ψ represents physically the *stored energy* during the deformation and for this reason a *normalization condition* must exist, namely when no deformation occurs ($\mathbf{F} \equiv \mathbf{I}$) the density function vanishes ($\Psi(\mathbf{I}) = 0$) being actually the global minimum since it is also non negative ($\Psi(\mathbf{F}) \geq 0$)). Furthermore, for the behavior at finite strain the scalar-valued function Ψ must satisfy also the so-called *growth condition*, i.e. it tends to $+\infty$ either when J approaches to 0 or $+\infty$, namely a compression of the body to a point or an infinite expansion requires an infinite amount of energy.

Another important property is that the function Ψ is objective in the sense that a superimposed rigid translation and rotation ($\mathbf{Q} \in orth^{+}$) of the current deformation χ does not modify the energy stored. Hence,

$$\Psi(\mathbf{F}) = \Psi(\mathbf{F}^{*}) = \Psi(\mathbf{Q}F) \tag{1.57}$$

being $\mathbf{F}^{*} = \mathbf{QF}$ the deformation gradient after the imposing of the rigid-body roto-translation. In this perspective, taking as rotation tensor the proper rotation tensor defined in Equation (1.8) $\mathbf{R}^{T}$ (or $\mathbf{R}$), one has that $\Psi(\mathbf{F}) = \Psi(\mathbf{R}^{\mathbf{T}}\mathbf{F}) = \Psi(\mathbf{R}^{\mathbf{T}}\mathbf{RU})$ and so one has

$$\Psi(\mathbf{F}) = \Psi(\mathbf{U}) = \Psi(\mathbf{V}) \tag{1.58}$$

Since from Equations (1.12) to (1.14) hold, one deduces that Ψ may be also expressed in terms of the right (left) Cauchy-Green $\mathbf{C}$ ($\mathbf{B}$) or equivalently of the Green Lagrange strain tensor $\mathbf{E}^{(2)}$ ($\mathbf{G}^{(2)}$), or more in general in terms of a specific strain measure $\mathbf{E}^{(\mathbf{m})}$ ($\mathbf{G}^{(\mathbf{m})}$), namely

$$\Psi(\mathbf{F}) = \Psi(\mathbf{C}) = \Psi(\mathbf{B}) = \Psi(\mathbf{E}^{(2)}) = \Psi(\mathbf{G}^{(2)}) = \Psi(\mathbf{E}^{(\mathbf{m})}) = \Psi(\mathbf{G}^{(\mathbf{m})}) \tag{1.59}$$

By means of the chain rule ($\left(\frac{\partial\Psi(\mathbf{F})}{\partial\mathbf{F}}\right)^{T} = 2\frac{\partial\Psi(\mathbf{C})}{\partial\mathbf{C}}\mathbf{F}^{T}$), since $\mathbf{C}$ is symmetric and thus the gradient of $\Psi(\mathbf{C})$ with respect to $\mathbf{C}$ is also symmetric, the Equations (1.55) and (1.56) can be expressed also in terms of $\mathbf{C}$, i. e.

$$\mathbf{P} = \mathbf{F}\frac{\partial\Psi(\mathbf{C})}{\partial\mathbf{C}} \tag{1.60}$$

$$\mathbf{T} = 2J^{-1}\mathbf{F}\frac{\partial\Psi(\mathbf{C})}{\partial\mathbf{C}}\mathbf{F}^{T} \tag{1.61}$$

Note that the choice of the strain measure used to define the strain energy density function specializes the constitutive law for the conjugated stress measure (Equation (1.48)); in fact, for a hyperelastic material, the constitutive law can be expressed also as follows

$$\mathbf{T}^{(m)} = \frac{\partial\Psi(\mathbf{E}^{(m)})}{\partial\mathbf{E}^{(m)}} \tag{1.62}$$

Isotropic Hyperelasticity

A material is *isotropic* when possesses the property that its response does not change with respect changing in any direction of the solicitation. In the context of hyperelasticity this implies an invariance of Ψ to any rotations in the sense that, considering a strain density function expressed in term of **C** and the transformation rules to rigid-body rotation in Section 1.1 one has

$$\Psi(\mathbf{C}) = \Psi(\mathbf{C}^*) = \Psi(\mathbf{QCQ^T}). \tag{1.63}$$

Recalling the *Representation Theorem* for isotropic scalar function, the isotropic scalar-value tensor functions $\Psi(\mathbf{C})$ can be expressed in terms of any invariants of **C**. Taking as invariant the principal invariant of **C** ($I_1(\mathbf{C})$,$I_2(\mathbf{C})$ and $I_3(\mathbf{C})$), by means of the chain rule and the definition of the invariant one, can obtain:

$$\mathbf{P} = 2\mathbf{F}\left[\left(\frac{\partial\Psi}{\partial I_1} + I_1\frac{\partial\Psi}{\partial I_2}\right)\mathbf{I} - \frac{\partial\Psi}{\partial I_2}\mathbf{C} + I_3\frac{\partial\Psi}{\partial I_3}\mathbf{C^{-1}}\right] \tag{1.64}$$

Instead, considering as invariant the principal stretches λ_i, the eigenvalues of **C**, one can obtain, as consequence of Equation (1.55), the principal Piola-Kirchhoff stresses P_i as follows

$$P_i = \frac{\partial\Psi}{\partial\lambda_i}, \tag{1.65}$$

and thus, inverting Equation (1.35), one can express the principal Cauchy stresses T_i as follows

$$T_i = J^{-1}\lambda_i\frac{\partial\Psi}{\partial\lambda_i}, \tag{1.66}$$

Incompressible material

If a material maintains constant the volume during any deformation, this implies that, by Equation (1.6),

$$J - 1 = 0 \quad \text{with} \quad J = I_3(\mathbf{C}) \tag{1.67}$$

representing an internal constraint, the *incompressibility constraint*. As usual in physics when dealing with constrains, the strain energy density function is enhanced by a *Lagrange multiplier* in order to include the constraint into the constitutive law, and thus the function Ψ may be postulated as follows

$$\Psi = \Psi(\mathbf{F}) - p(J-1) \tag{1.68}$$

p being the scalar the multiplier that can identified by an *hydrostatic pressure*. As usual when dealing with Lagrangian multiplier in boundary value problems one can obtain p imposing the boundary conditions,

namely the equilibrium at the boundary.
The stress tensor P, thus becomes

$$\mathbf{P} = -p\mathbf{F}^{-\mathbf{T}} + \frac{\partial \Psi(\mathbf{F})}{\partial \mathbf{F}} \tag{1.69}$$

Inverting Equation (1.35) in the incompressibility framework ($J = 1$) and thus multiplying in Equation (1.69) both sides for $\mathbf{F}^T$, one obtains the Cauchy stress tensor for incompressible hyperelastic materials, i. e.

$$\mathbf{T} = -p\mathbf{I} + \mathbf{F}\frac{\partial \Psi(\mathbf{F})}{\partial \mathbf{F}} \tag{1.70}$$

Note that in the case of incompressible isotropic material the invariants will be reduced to I_1 and I_2, in the case one use the principal invariants, or two of the principal stretches (λ_i), since the third one is dependent from the other two stretches ($I_3 = J = \lambda_1\lambda_2\lambda_3 = 1$).
In the framework of incompressible hyperelastic materials there are several phenomenological models, most of which can be expressed as special cases of the *Ogden model* for which $\Psi(\mathbf{F})$ is given by:

$$\Psi(\lambda_1,\lambda_2,\lambda_3) = \sum_{p=1}^{N} \frac{\mu_p}{\alpha_p}\left(\lambda_1^{\alpha_p} + \lambda_2^{\alpha_p} + \lambda_3^{\alpha_p} - 3\right) \tag{1.71}$$

being the parameters μ_p and α_p specific phenomenological coefficients which characterizing the material at hand. To be consistent with the linear elastic theory, namely $\lambda_i \to 1$ for $i = 1,2,3$, the parameter must respect the following condition

$$2G = \sum_{p=1}^{N} \mu_p\alpha_p \quad \text{with } \mu_p\alpha_p \quad \forall p = 1,2,..,N \tag{1.72}$$

with $G = \frac{E}{2(1+\nu)}$ is the first Lamé constant, the *shear Modulus*, being a third of the *Young Modulus E* as the material is incompressible (*Poisson ration* $\nu \to 0.5$).
It is worth to introduce some special cases of the Ogden model that is the *Neo-Hookean model* and the *Mooney-Rivlin model*. The former is obtained by setting $N = 1$ and $\alpha_1 = 2$, namely

$$\Psi_{NH} = \frac{\mu_1}{2}(\lambda_1^2 + \lambda_2^2 + \lambda_3^2 - 3) = \frac{\mu_1}{2}(I_1(\mathbf{C}) - 3) \quad \text{with } \mu_1 = G, \tag{1.73}$$

while, the latter is obtained by setting $N = 2$, $\alpha_1 = 2$ and $\alpha_2 = -2$, namely

$$\begin{aligned}\Psi_{MR} =& \frac{\mu_1}{2}(\lambda_1^2 + \lambda_2^2 + \lambda_3^2 - 3) - \frac{\mu_2}{2}(\lambda_1^{-2} + \lambda_2^{-2} + \lambda_3^{-2} - 3)\\ =& \frac{\mu_1}{2}(I_1(\mathbf{C}) - 3) - \frac{\mu_2}{2}(I_2(\mathbf{C}) - 3) \quad \text{with } \mu_1 - \mu_2 = G\end{aligned} \tag{1.74}$$

Compressible materials

There are several approaches in literature to model the phenomenological behavior of compressible materials. For example the response can be *decoupled* in a purely *isochoric* and purely *volumetric* contribution, since some materials behave quite differently in bulk in comparison with shear tests. With respect to the following applications, let us introduce here the Neo-Hookean model for compressible material. It is a *coupled* approach in which the isochoric and the volumetric contribution are not singularly detectable. The strain energy density function is given by

$$\Psi_{CNH}(I_1, J) = +\frac{G}{2}(I_1 - 3) + \frac{G}{2\beta}\left(J^{-2\beta} - 1\right) \tag{1.75}$$

being G the "tangent" shear modulus and $\beta = \frac{\nu}{1-2\nu}$ a parameter depending on the "tangent" Poisson ratio ν.

1.5 CONSTITUTIVE EQUATION: FUNDAMENTALS OF LINEAR CLASSICAL AND "FRACTIONAL" VISCOELASTICITY

In the context of linear deformation the materials behave as elastic solids, viscous fluids and with a behavior in between these two families that is the viscoelastic material.

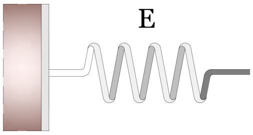

Figure 1.1: Elstic Solid

Elastic solids, as previously mentioned, have the characteristic to assume a own shape (solid) and the deformation due to external loading is completely recovered when the loading is removed (elastic). Considering, for sake of simplicity a 1-D experiment, the constitutive law in the context of linear elasticity is the Hooke law, namely the true stress T in the direction of the deformation ε is linearly dependent by means of a parameter depending on the specific material that is the Young Modulus E, following the relationship

$$T_E(t) = E\varepsilon(t) \tag{1.76}$$

ε being the only component of linerized version of the Green-Lagrange strain measure in Equation (1.14). The Equation (1.76) highlights that the tension in a specific instant $T(t)$ depends on the deformation at the same time $\varepsilon(t)$ and vice-versa. Thus, if the solicitation is removed an instantaneous recovery occurs, instead if it holds, there is no further increment in the deformation. Usually, as shown in Figure 1.5, to represent elastic solids a spring is used.

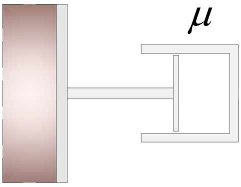

Figure 1.2: Viscous fluid

Viscous fluids unable to have an own shape, assume the one of the receptacle containing them and in the ideal behavior -*Newtonian fluids* - the stress due to a deformation depends on its rate, following the so-called *Newton-Petroff* law as follows

$$T_\mu(t) = \mu\dot{\varepsilon}(t) \tag{1.77}$$

μ being constant parameter related to the viscosity of the fluid. The Equation (1.77) highlights that if the solicitation holds the deformation continues to increase and there is no recovering of the deformation after the removal of the external solicitation and no energy is stored, and thus recovered, but all is generally transformed in heat. Commonly the symbol used to represent viscous fluid is the dash-pot (see Figure 1.2)

Viscoelastic materials as mentioned, have an intermediate behavior. In fact, the stress at a certain time t depends on history of deformation (purely viscous) and a certain amount of energy - and thus deformation- is recovered (purely elastic). Considering the *Boltzmann superposition principle* the behavior of a viscoelastic material is completely described knowing either the *creep* ($\psi(t)$) or the *relaxation* ($\phi(t)$) functions, in fact is possible to describe the deformation ε and the stress T respectively, at a certain instant t following the subsequent relationships

$$\varepsilon(t) = \int_0^t \dot{T}(\tau)\psi(t-\tau)\,d\tau + T_0\psi(t),\ and \tag{1.78}$$

$$T(t) = \int_0^t \dot{\varepsilon}(\tau)\phi(t-\tau)\,d\tau + \varepsilon_0\phi(t) \tag{1.79}$$

where the the function $\psi(t)$ by definition is the deformation response of the material to a constant in time unit stress solicitation and T_0 is the stress at the initial instant, while the function $\phi(t)$ is the stress response of the material to a constant in time unit deformation applied and ε_0 is the deformation at the initial instant $t = 0$.

Historically the viscoelastic materials have been modeled by means classical paradigms such as the *Maxwell, Voigt and Standard Linear Kelvin* ones made by specific combinations of parallel and/or series of springs and dash-pots.

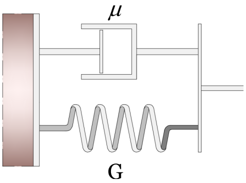

Figure 1.3: Voigt model

The Voigt (viscoelastic solid) idealization assumes that viscous and elastic elements are placed in parallel each other (see Equation (1.81)). In this way, the resulting overall stress can be determined by the simple sum of the stress due to the single constituting elements as follows

$$T(t) = T_E(t) + T_\mu(t) \tag{1.80}$$

where T_E and T_μ are the stresses due to the elastic contribution and viscous one respectively defined in Equations (1.76) and (1.77). Considering that a isodisplacement condition holds, namely the deformation in the dash-pot is the same of the one in the spring $\varepsilon_E(t) = \varepsilon_\mu(t) = \varepsilon_V(t)$ one has the following constitutive relationship

$$T_V(t) = E\varepsilon(t) + \mu\dot{\varepsilon_V}(t) \tag{1.81}$$

The relaxation function for the Voigt, when a constant unit deformation is applied at instant $t = 0$ will be

$$\phi(t) = E + \mu\delta(t) \tag{1.82}$$

being $\delta(t)$ a *Dirac* impulse and so behaving essentially as a viscous fluid instantaneously for $t = 0$, and as an elastic solid for $t \to \infty$. Instead the creep function is an exponential function as follows

$$\psi(t) = \frac{1}{E}\left(1 - e^{-\frac{E}{\mu}t}\right) \tag{1.83}$$

being the viscosity parameter $\nu = \frac{\mu}{E}$.

The *Maxwell* (viscoelastic fluid) paradigm is the in-series combination

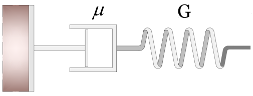

Figure 1.4: Maxwell Model

of a spring and a dash-pot (see Figure 1.4). In this case the the isostress condition holds and so the resulting deformation is the sum of the elastic ε_E and of the viscous ε_μ contribution

$$\varepsilon_M(t) = \varepsilon_M(t) + \varepsilon_\mu(t), \tag{1.84}$$

while the stress is shared $T_M(t) = T_E(t) = T_\mu(t)$ in the single elements. In this perspective the constitutive equation for the Maxwell model is thus

$$\dot{\varepsilon}_M = \mu T_M(t) + E\dot{T}_M(t) \tag{1.85}$$

Thus, the relaxation function is an exponential function as follows

$$\phi(t) = Ee^{-\frac{E}{\mu}t} \tag{1.86}$$

and the creep function is a linear function of the time as

$$\psi(t) = \mu t + \frac{1}{E} \tag{1.87}$$

behaving instantaneously as an elastic solid but for $t \to \infty$ as a viscous fluid. It is worth to highlight that Voigt and Maxwell represent an idealization of the actual behavior of the viscoelastic materials. It is very uncommon, for example, dealing with materials with relaxation function in agreement with Voigt model, although it is possible to find an appropriate time constant $\tau = \mu/E$ to approximate well the relaxation behavior of an actual viscoelastic material. Ually for the Maxwell model its creep function is in very good agreement with experiments but the relaxation behavior is not easily comparable with physical materials. In any case these paradigms have been widely utilized in the classical theory of viscoelasticity for their computational simplicity and because is possible to increase the accuracy combining multiple Voigt and Maxwell elements with other elastic and viscous models forming the so called *Zenner* or Standard Linear Solid (SLS) viscoelastic models. The general equation for the SLS is given by the following relationship

$$\sum_{k=0}^{n} a_k \frac{d^k}{dt^k} T(t) = \sum_{k=0}^{m} b_k \frac{d^k}{dt^k} \varepsilon(t) \tag{1.88}$$

where n and m depend on the complexity of the model adopted, i. e.the number of elastic and viscous elements in parallel/series combination, and a_k and b_k on the Young modulus and viscosity of each element. Worthily, increasing the number of the elements it is possible to increase the accuracy of the models but also their complexity since a greater number of parameters have to be found by means of best fitting analyses arising the possibility to deal with critical negative values for the stiffness, for expample.

Furthermore, since the response equations are ordinary differential equations, the kernel of the solution and thus of the relaxation/creep functions have exponential dependence on time. This is in contrast with numerous experimental study ([73, 101, 119]) that have shown a *power law* trend in time on the tension/deformation response. To model this kind of behavior and reduce the parameters needed to catch a qualitative acceptable analytic response, the *fractional calculus or fractional derivative* has to date been considered in order to overcome the limitation of the ordinary differential equation. The concept of the fractional derivative can be dated back to 1695 during correspondence between de L'Hospital and Leibniz. Their purpose was to give an answer to the famous question: 'What does the derivative $d^n f(x)/dx^n$ mean if $n = 1/2$?'. From that time, a branch of mathematics named fractional calculus has been developed and it is to date considered a generalization of the commonly used integer-order differentiation and integration. The basic idea is to look at a fractional derivative as the inverse operation of a fractional integral, as suggested by Riemann–Liouville. Caputo developed a concept of the fractional α derivative between the integer (ordinary) orders $n-1 \leq \alpha \leq n$, commonly indicated by ${}_{a}^{C}D_t^a$, which could be used in the "real world", defined as follows

$$ {}_{a}^{C}D_t^{\alpha} f(t) = \frac{1}{\Gamma(n-a)} \int_a^t (t-s)^{n-\alpha-1} f^{(n)}(s)\, ds \qquad (1.89) $$

where $f(t)$ is an integrable function in $[a,t]$ and Γ is the Euler Gamma function.

The idea to use fractional derivatives in viscoelasticity can be traced back to the work by Nutting [101]. He noted that, from the best fitting of experimental curves, the relationship between deformation and time could be described by a power law, i.e. $\varepsilon(t) \propto t^n T(t)^m$. In 1949, Blair & Caffyn [7] justified analytically this experimental law through fractional derivatives, introducing a new paradigm in viscoelasticity the so-called *spring-pot* *model* for which the relationship between stress and deformation holds as follows

$$T(t) = C_\alpha\, {}_0^C D_t^\alpha \varepsilon(t) \tag{1.90}$$

where ${}_0^C D_t^\alpha$ is the fractional derivative with $0 \leq \alpha \leq 1$ and C_α is a coefficient that, following Koeller [73] for the uni-axial stress/stretching test, takes the following form

$$C_\alpha = E\left(\frac{\mu}{E}\right)^\alpha . \tag{1.91}$$

It is worth to highlight that is possible to catch an infinite possible viscoelastic behaviors with the spring-pot model, varying with continuity the parameter α, between the limit purely elastic ($\alpha = 0$) and viscous ($\alpha = 1$) case. Although the spring pot seems to be the best analytic model to simulate the viscoelastic behavior of any material it does not have a complete physical interpretation, in fact is not possible to distinguish the single viscous or elastic contribution.

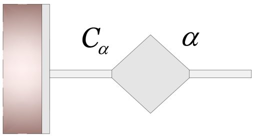

Figure 1.5: Spring Pot

In this perspective the relaxation $\phi(t)$ and the creep $\psi(t)$ functions follows a power law in time as follows

$$\phi = \frac{C_\alpha}{\Gamma(1-\alpha)} t^\alpha \tag{1.92}$$

$$\psi = \frac{1}{C_\alpha \Gamma(1+\alpha)} t^\alpha \tag{1.93}$$

It is finally opportune to observe that with only one spring-pot model with just two parameters (α and C_α), to find by a best fitting procedure, one can obtain a very good approximation of a generic viscoelastic experimental behavior of material. This is an enhancement with respect to use a consistent number of "classical" elements (ordinary time derivative)- i. e.SLS model- involving a grater number of parameters despite having not a similar good approximation since an exponential time dependence of the creep/relaxation functions is implicated.

2

SINGLE CELL MECHANICS

INTRODUCTION

In the human body there are trillions of (10 $\sim$ 100 microns in size) cells: they have all the same structure and all originate from a single fertilized egg, the zygote, that differentiates in specialized cells. The structure of the human cell is a complex factory that makes proteins, including tissue materials [20]. It is constituted by three mechanically relevant systems: the cell membrane - the wall of the factory - an about 10-nm thick very deformable (0.1 $\sim$ 1 kPa) lipid bilayer, the membrane-confined visco-elastic gel-like cytosol and the cytoskeleton - the bearing structure of the cell - an elastic network of protein filaments, embedded in the cytosol and anchored to the membrane, that maintains the cell shape, protects the cell, enables cell motion (migration and adhesion), mediating inner and outer loads. The main kinds of cytoskeletal filaments are microtubules (25-nm diameter tubes made up of spiraling tubulin in two-part subunits), actin filaments (7-nm diameter twisted double strands of the protein actin) and intermediate filaments (10-nm diameter interwoven, rope-strands), cell spreading and motility being driven by the assembly (polymerization) and disassembly (depolymerization) of branched actin filaments [3, 9].

Overall, the cell behaves as a viscoelastic system [30, 33, 56, 127]. However, differently from inorganic materials, biological soft matter is inhomogeneous and generally hierarchically organized [15, 43, 46, 63, 114] and thus reacts to mechanical stimuli by simultaneously involving several cell districts and processes, as well as protein filaments and supra-molecular and molecular structures present at different scale levels. The cell hierarchical organization works as a complex transducer device that converts macro-mechanical signals (pressure gradients, oscillation of organelles, etc) in a way to activate a biomechanical orchestra that steer a cascade of biochemical and physical coordinated events which govern the mechanobiology and the mechanosensing of the whole cell, regulating differentiation, growth, morphogenesis, and - through polymerization/depolymerization-based cytoskeleton structural rearrangements - migration and adhesion phenomena affecting both single-cell dynamics and macroscopic behaviors of tissue and tumor masses [31, 36, 53, 105].

Several scientific papers have been in the last two decades devoted to the study of the effects of mechanical stimuli on human cells, leading to observe a number of biological behaviors whose essential processes are often still obscure or only partially understood. It has been for example observed that the effect of ultrasound upon single cells is significantly influenced by the frequency and the energy density applied [118]. Cell membrane damages were observed after ultrasound treatment in human blood cells and leukemic cell lines [38], experimental studies demonstrating that malignant cells are sometimes much more susceptible and prone to be killed than normal cells when subjected to ultrasound exposure [79, 80]. Depending on cell type and sonication protocol, ultrasounds seem to be able - if adequately modulated - to decrease cancer cell growth as well as to increase and stimulate wound healing [118]. In particular, increases of the proliferation rate for hcMEC and MDCK healthy cells after application of ultrasound at various energy density levels and prescribed frequencies have been experimentally observed and, after ultrasonic exposure, HT29 monitored cancer cells have exhibited cell death (apoptosis) [118]. Additionally, it has been seen that ultrasounds inhibit cell proliferation of human myelomonocytic lymphoma U937 cells and stimulate MCF-7 breast cancer cells to undergo apoptosis [16, 62], although the same investigators admit that "the molecular mechanism of ultrasound induced apoptosis has not yet been clearly understood". Recently, however, Mizrahi et al [99] have experimentally observed significant cytoskeleton reversible remodeling dynamics when human airway smooth muscle cells were exposed to low intensity ultrasounds, these physical changes being caused by very small strains (10^{-5}) at ultrasonic frequencies (10^6 Hz), close to those caused by relatively large strains (10^{-1}) administered at physiological frequencies (10^0 Hz).

Biologically relevant motion of intracellular particles, induced by ultrasonic waves, has been hypothesized to play a key role in the mechanism at the basis of relative displacement between cell organelles and cytoplasm as effect of the different inertia of the media. Although the question on how the mechanical vibrations act on the biological cell behavior substantially still remains an open issue, a study by Or and Kimmel [103] theoretically explores the possibility of resonance-like phenomena and suggests that mechanically-induced oscillations - larger than maximal thermal fluctuations - might kindle high-frequency (compatible with Low Intensity Therapeutic Ultrasounds ranges) strain regimes, potentially able to determine fatigue-like phenomena in cells. In particular, the frequency resonance hypothesis assumes that the absorption of ultrasound by proteins and protein complexes may directly alter signaling mechanisms within the cell, determining conformational shift or disrupting of multimolecular complexes at critical frequencies found both around 45 kHz and 1 MHz [66].

On the other hand, very recently experimental studies have been performed on individual cancer and healthy cells of different types, demonstrating that the first ones were about 70% softer than the latter ([22, 23, 41, 70, 81–83, 85, 100, 113, 115] - see Table 4 for details). As a matter of fact, it seems that the increase in cell deformability is directly related to the cancer progression, as observed by Ketene et al [70] in the cases of a transformed phenotype from a benign (nontumorigenic) cell to a malignant (tumorigenic) one. Ploidinec et al [111], by resolving the *nanomechanical signatures* of defined stages of tumor progression, also highlight that cancer evolution is associated with a significant softening of tumor epithelial cells in comparison to normal mammary epithelium, including metastasis, hypothesizing that metastatic cells gain their migration capabilities by acquiring a certain degree of flexibility and deformability to escape their original niche. As assumed by Pachenari et al [104], metastatic cells could be spurred to become mechanically softer than healthy cells to pass through rigid capillaries whose diameters are smaller than tumor cells, deformability in this way playing a crucial role in the potency of tumor cells to form neoplastic foci. This seems to be also corroborated by experiments, as found by Abdolahad et al [1] who show that the fraction of entrapment of higher metastatic cancer cells (in carbon nanotubes) is significantly more than lower metastatic grades.

These results, which seem to be confirmed regardless of the cell lines examined and independently from the specific measurement technique used for determining the mechanical properties (Atomic Force Microscopy, Optical tweezers, etc.), lead to envisage possible new scenarios for biomechanical applications in medicine [67]. At least in principle, the above mentioned differences in cell stiffness might be in fact *ad hoc* exploited to build up mechanical-based targeting strategies for discriminating neoplastic transformations within human cell populations, in this manner paving the way for designing innovative complementary tools to cell-specific molecular tumor markers and, hopefully in a future, for possible applications in diagnoses and therapies of cancer diseases [50, 59, 60].

In this perspective, by recalling the above mentioned experimental evidences about the discrepancies in deformability between tumor and normal cells, with the aim of at early stage characterizing - and gaining insights into - the frequency response of single-cell systems to mechanical stimuli (typically Low Intensity Therapeutic Ultrasounds), a generalized viscoelastic paradigm which combines classical (say Voigt, Maxwell and standard linear Kelvin) and spring-pot based models is introduced for modeling the problem at hand (Section 2.1), by starting from the work by Or and Kimmel [103]. To this purpose, it has been necessarily neglected any detail related to the complex structural organization of the cells in which nucleus, cytoskeleton, elastic membrane and gel-like cytosol govern and interact with the cascade of events at the basis of the mechanobiology of the system.

Therefore, motivated by the above mentioned literature findings and with the aim of including the effect of the prestress –for instance induced in protein filaments during cell adhesion– on the overall cell stiffness and determining its influence on the in-frequency response of the cell, a simple multiscale scheme incorporating finite elasticity is first proposed to consider, by means of a *bottom-up* homogenization procedure, suitable prestress-modified stiffness values into the viscoelastic single-cell models. Successively, once the analytical expression of the overall elastic stiffness of an adherent cell has been obtained, the identification of some key model parameters (i.e. prestretch and number of "active" filaments) has been determined to fit the realistic stiffness moduli experimentally measured in the literature for several cell types. Finally, after a short presentation of new generalized spring-pot (fractional derivative-based) viscoelastic models, a preliminary wide campaign of sensitivity analyses aimed to catch both qualitative and quantitative remarks on mechanically stimulated single-cell systems (see Section 2.4), the viscoelastic modeling is finally specialized to cell lines whose mechanical properties have been experimentally measured in the literature with reference to healthy cells and their cancer counterparts. The theoretical results, illustrated in Section 2.3, will show that the differences in stiffness - at least in principle - allow to mechanically discriminate between tumor and normal cells, the critical frequencies associated to oscillation magnitude peaks (found from tens kHz to hundreds kHz) confirming that mechanical resonance-like phenomena can be prevailing with respect to thermal fluctuations and could thus be helpfully utilized for targeting or *ad hoc* altering the functions of tumor cells.

2.1 FREQUENCY RESPONSE OF ONE-DIMENSIONAL SINGLE-CELL VISCOELASTIC SYSTEMS

By starting from an approach recently proposed by Or and Kimmel [103] to analyze the case of vibrating cell nucleus in a viscoelastic environment excited by Low Intensity Therapeutic Ultra-Sound (LITUS), let us consider the single cell dynamics through an oscillating mass embedded in a viscoelastic medium (see Figure 2.1). A spherical rigid object with radius R is therefore considered to represent the nucleus, in which it is ideally assumed to be concentrated the whole mass of the cell, the environment being instead idealized to behave as a homogeneous and isotropic viscoelastic medium: in this way the system will be characterized by one degree of freedom activated by a prescribed time-varying LITUS-induced velocity law in the form

$$v_m(t) = v_{m0} e^{-i\omega_0 t} \tag{2.1}$$

where v_m is the velocity assigned to the medium, v_{m0} represents the complex velocity phasor, and $\omega_0 = 2\pi f$ is the angular frequency of the oscillations, f being the frequency measured in Hz. By essentially following the strategy suggested in the above mentioned work, the equation of motion can be written as

$$f_m = m_{ob} a_{ob} = \frac{4}{3}\pi R^3 \rho_{ob} \frac{d^2 u_{ob}}{dt^2} = f_{ac} - f_{res} \tag{2.2}$$

In eq. (2.2) t is the time, f_m represents the inertial force, m_{ob} is the nucleus mass whose density is ρ_{ob}, and u_{ob} is the associated displacement. Furthermore, f_{ac} is the basic driving force in the system, due to the acoustic pressure gradients that are induced by the ultrasound transducer. In the present case, where the object is very small compared with the acoustic wavelength, the acoustic force can be assumed with the simple form of a force which would act on a sphere of the same size in the absence of the object [90]; this permits to write

$$f_{ac} = \frac{4}{3}\pi \rho_m R^3 \frac{Dv_m}{Dt} \equiv \frac{4}{3}\pi \rho_m R^3 \frac{dv_m}{dt} \tag{2.3}$$

where ρ_m is the density of the medium. Dimensional analyses suggest that the convective term is small and therefore, in eq. (2.3), the absence of spatial variability leads to use regular time-differentiation d/dt instead of the substantial derivative D/Dt [103].

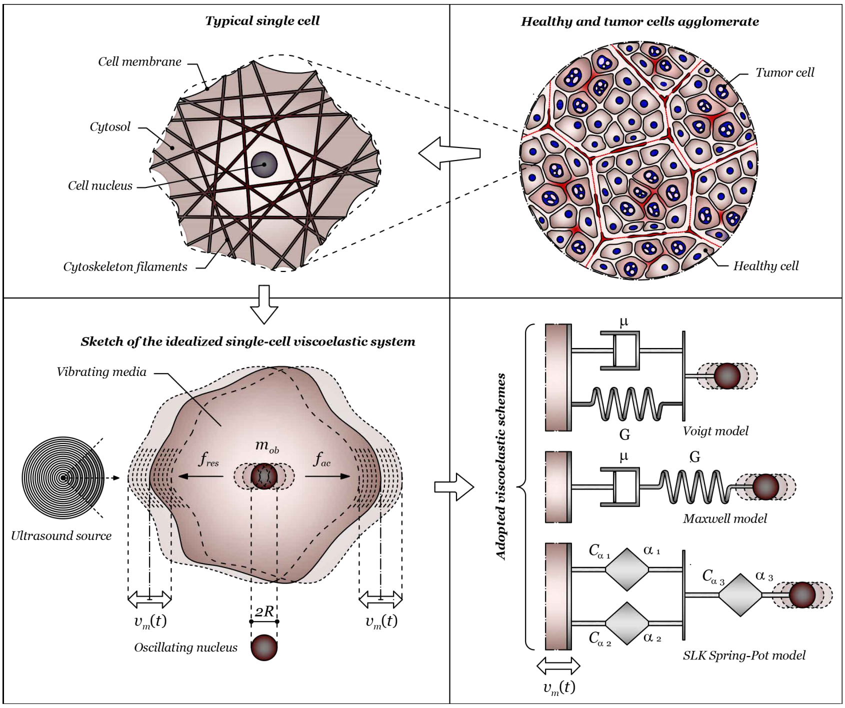
Typical single cell
Cell membrane
Cytosol
Cell nucleus
Cytoskeleton filaments
Healthy and tumor cells agglomerate
Tumor cell
Healthy cell
Sketch of the idealized single-cell viscoelastic system
Vibrating media
m_{ob}
f_{res}
f_{ac}
Ultrasound source
$v_m(t)$
$2R$
$v_m(t)$
Oscillating nucleus
Adopted viscoelastic schemes
μ
G
Voigt model
μ
G
Maxwell model
C_{α_1}
α_1
C_{α_3}
α_3
C_{α_2}
α_2
SLK Spring-Pot model
$v_m(t)$

Figure 2.1: Cartoon of the idealized single-cell system: (*top-right*) healthy and tumor cells agglomerate; (*top-left*) typical cell unit, with nucleus and cytoskeleton structure embedded in the cytosol and confined by the lipid bilayer cell membrane; (*bottom-left*) idealized single-cell system with cell nucleus oscillating in a viscoelastic environment under the action of radiating ultrasound source; (*bottom-right*) adopted viscoelastic schemes (Voigt, Maxwell and generalized Spring-Pot based Standard Linear Kelvin models).

Finally, f_{res} is the response force which is applied on the object by its surrounding as a result of their relative motion; as a consequence, the response force depends upon the rheological properties of the medium in which the object is embedded. In particular, in order to catch fundamental insights on different - and more complex - behaviors of single-cell systems, this force will be written as parametrically depending on several geometrical and mechanical features of interest. The analyses will be conducted by adopting two quasi-standard viscoelastic models, the classical Voigt and Maxwell ones, and finally considering a generalized standard linear Kelvin model, where dashpot and springs are substituted by so-called Spring-Pot systems, widely adopted in several recently appeared research works to interpret peculiar responses of biological structures [34].
Additionally, differently from the strategy utilized by Or and Kimmel [103] to solve the differential problem at hand, the Laplace transform will be here utilized by exploiting the well-known classical relationship between Laplace and Fourier transforms, that is $\mathscr{F}[\cdot] = \mathscr{L}[\cdot]\big|_{s=i\omega}$, in this way gaining the possibility of directly obtaining the response of the systems in terms of frequency.
With reference to the initial conditions, in all the cases the object is initially at rest, that is

$$u_{ob}\big|_{t=0} = 0 \quad , \quad \frac{du_{ob}}{dt}\big|_{t=0} = 0 \tag{2.4}$$

Then, by Laplace transforming the eq. (2.2), one obtains

$$f_m = \frac{4}{3}\pi R^3 \rho_{ob} s^2 U_{ob} = F_{ac} - F_{res} \tag{2.5}$$

where all the transformed terms are denoted with capital letters and s is the Laplace variable. As a consequence, in eq. (2.5) F_{ac} is the Laplace transforming of the acoustic force f_{ac} in the eq. (2.3), so obtaining

$$F_{ac} = \frac{4}{3}\pi \rho_m R^3 s V_m = \frac{4}{3}\pi \rho_m R^3 s^2 U_m \tag{2.6}$$

2.1.1 *Cells behaving as quasi-standard Voigt model*

As above introduced in section 1.5, in the Voigt idealization, viscous and elastic elements are connected to each other in parallel (see Figure

2.1). Differently from section 1.5 the constitutive relationship is here presented in terms of response force that is then obtained by simply summing up the contributions of the two elements as follows

$$f_{res} = f_{\mu} + f_G \tag{2.7}$$

where f_{μ} is the viscous force response and f_G represents the elastic contribution. By following the Or and Kimmel [103] suggestion, with the aim include the effects of rapid (high frequency) vibrations the classical contituvive relationships are here enhanced including spurious frequency dependent terms generally so-called *added mass* and *virtual friction*. In fact the viscous term is here modeled following Basset [5] and Landau and Lifshitz [77] for which the response force can be thus written as

$$f_{\mu} = 6\pi R\mu \left(1 + \sqrt{\frac{\omega R^2}{2\nu}}\right)(v_{ob} - v_m) + \frac{2}{3p}\pi R^3 \rho_m \left(1 + \frac{9p}{2}\sqrt{\frac{2\nu}{\omega R^2}}\right)(\dot{v}_{ob} - \dot{v}_m) \tag{2.8}$$

with μ and ν the dynamic and the kinematic viscosities of the medium, respectively, and $v = \dot{u}$cthe velocity. It is worth to highlight how the structure of the viscous response force assumed here differs from the classical Stokes force (eq. (1.77)) because in eq. (2.8) appears a spurious inertial contribution that Brennen [8] termed *added mass*, that is $3\pi R^3 \rho_m \sqrt{\frac{2\nu}{\omega R^2}}$. p ($p = 2$ in the present case) is the number of elements in parallel, here utilized to solve the ambiguous situation raised by [103], so avoiding the duplication of added mass contribution in the viscoelastic system at hand[1].

With reference to the elastic force, f_G, as proposed by Ilinskii et al. [65], is explicitly written as follows

$$f_G = 6\pi GR(u_{ob} - u_m) + 6\pi R^2 \sqrt{G\rho_m}(\dot{u}_{ob} - \dot{u}_m) + \frac{2}{3p}\pi R^3 \rho_m (\ddot{u}_{ob} - \ddot{u}_m) \tag{2.9}$$

---

[1] By separately inserting *virtual friction* and *added mass* in both the purely viscous and purely elastic models, Or and Kimmel [103] have that in the viscoelastic Voigt model "*the response force is obtained by summing up the contributions of the two elements (dashpot and spring)...*" and thus they have to successively detract "*the excessive added-mass term*" that erroneously twice appears. In the present thesis, to avoid of *a fortiori* neglecting the "excessive added-mass term", it has been solved this ambiguous situation by setting *ab origine* the viscoelastic forces so that any simple scheme as well as any combined viscoelastic construct (including the general fractional-based SLK model) contains the sole added-mass and virtual friction contributions to be considered.

Analogously to the previous case, the elastic response differs from the classical Hooke law (eq. (1.76)): in fact, rigorously speaking it does not represent a pure elastic contribution and - again to take into account the effects of rapid fluctuations determined by the dynamic interaction of the system with the environment which drive the response towards the actual physical behavior - additional terms appear in (2.9). In particular, these contributions are here constituted by the so-called *virtual friction* (a dissipative term represented by $6\pi R^2\sqrt{G\rho_m}$) and, again, the *added mass* (an inertial term), as suggested by Ilinskii et al [65]. In eq. (2.9), G is the elastic shear modulus of the medium, assumed to be about a third of the corresponding Young modulus as a consequence of the hypothesis of incompressibility, while u_m represents the vibrational displacement of the medium. Hereinafter, the following parameters are conveniently introduced

$$c_{0G} = 6\pi GR, \quad c_{1G} = 6\pi R^2\sqrt{G\rho_m}, \quad c_{2G} = \frac{2}{3p}\pi R^3\rho_m \tag{2.10}$$

$$c_{1\mu} = 6\pi R\mu\left(1+\sqrt{\frac{\omega R^2}{2\nu}}\right), \quad c_{2\mu} = \frac{2}{3p}\pi R^3\rho_m\left(1+\frac{9p}{2}\sqrt{\frac{2\nu}{\omega R^2}}\right) \tag{2.11}$$

and a further dimensionless constant is also defined as follows

$$\zeta = \frac{\rho_{ob}}{\rho_m} = \frac{1}{1+\gamma} \tag{2.12}$$

with $\gamma = \rho_m\rho_{ob}^{-1} - 1$. At the end, the quasi-standard Voigt viscoelastic constitutive law is written down

$$f_{res} = c_{0G}\left(u_{ob}-u_m\right)+\left(c_{1\mu}+c_{1G}\right)\left(\dot{u}_{ob}-\dot{u}_m\right)+\left(c_{2\mu}+c_{2G}\right)\left(\ddot{u}_{ob}-\ddot{u}_m\right) \tag{2.13}$$

Laplace transforming the response force (2.13) one has

$$F_{res} = \left(U_{ob}-U_m\right)\left[c_{0G}+\left(c_{1\mu}+c_{1G}\right)s+\left(c_{2\mu}+c_{2G}\right)s^2\right] \tag{2.14}$$

and, replacing (2.14) and (2.6) in (2.5) and after some algebraic manipulations, the final form of the equation is obtained as

$$\left[c_{0G}+\left(c_{1\mu}+c_{1G}\right)s+\left(\left(c_{2\mu}+c_{2G}\right)+\frac{4}{3}\pi\rho_{ob}R^3\right)s^2\right]\Delta U = \frac{4}{3}\pi\gamma\rho_{ob}R^3 sV_m \tag{2.15}$$

where $\Delta U = U_{ob} - U_m$. By solving the eq. (2.15), the in-frequency analytical solution in terms of amplitude of the relative displacement ΔU between cell nucleus and environment takes hence the form

$$|\Delta U|\Big|_{s=i\omega} = \left| \frac{\frac{4}{3}\pi\gamma\zeta\rho_m R^3 s V_m}{c_{0G} + (c_{1\mu} + c_{1G})\, s + \left((c_{2\mu} + c_{2G}) + \frac{4}{3}\pi\rho_{ob}R^3 \right) s^2} \right| \Bigg|_{s=i\omega} \tag{2.16}$$

2.1.2 *Cells behaving as quasi-standard Maxwell model*

As above introduced in section 1.5, in the Maxwell system, viscous and elastic elements are connected in series (see Figure 2.1). In order to obtain the response in terms of relative displacement ΔU one has to start by imposing the *isostress* condition, that is

$$F_G = F_\mu = F_{res} \tag{2.17}$$

and then to write the compatibility condition, that is that the sum of the relative displacement due to the elastic and to the viscous components equates the relative displacement

$$\Delta U = \Delta U_G + \Delta U_\mu \tag{2.18}$$

where F_μ and F_G constitute the Laplace transforms of the viscous and the elastic response forces given in eqs. (2.8) and (2.9), respectively. As a consequence, one has

$$F_\mu = (c_{1\mu}s + c_{2\mu}s^2)\Delta U_\mu, \quad F_G = (c_{0G} + c_{1G}s + c_{2G}s^2)\Delta U_G \tag{2.19}$$

from which viscous and elastic components of the relative displacement are separately given as

$$\Delta U_\mu = \frac{F_\mu}{c_{1\mu}s + c_{2\mu}s^2}, \quad \Delta U_G = \frac{F_G}{c_{0G} + c_{1G}s + c_{2G}s^2} \tag{2.20}$$

By recalling F_{res} from eq. (2.5) and by taking into account eq. (2.20), the analytical solution for the frequency response of the quasi-standard Maxwell system is finally obtained as follows

$$|\Delta U|\Big|_{s=i\omega} = \left| \frac{\frac{4}{3}\pi\gamma\rho_{ob}R^3 s V_m}{1 + \frac{4}{3}\pi\rho_{ob}R^3 s^2 \left(\frac{1}{c_{1\mu}s + c_{2\mu}s^2} + \frac{1}{c_{0G} + c_{1G}s + c_{2G}s^2} \right)} \right| \Bigg|_{s=i\omega} \tag{2.21}$$

2.1.3 *Cells behaving as Spring-Pot based quasi-Standard Linear Kelvin model*

2.1.3.1 *Spring-Pot model involving* virtual friction *and* added mass

In section section 1.5 it has been shwn that the so-called Spring-Pot model is a viscoelastic system in which the constitutive law is defined through *Fractional Derivatives*. For the present purpose, the Spring-Pot model is substantially that firstly introduced by Blair and Caffyn [7], but it is here generalized to take into account the *virtual friction* and the *added mass* by means of the suitable introduction of additional contributions. In particular, the response Spring-Pot force f_{SP} is defined as follows

$$f_{SP} := C_\alpha \left({}_0^C D_t^\alpha \left(u_{ob} - u_m\right)\right) + c_{1SP}\left(\dot{u}_{ob} - \dot{u}_m\right) + c_{2SP}\left(\ddot{u}_{ob} - \ddot{u}_m\right) \quad (2.22)$$

in which ${}_0^C D_t^\alpha$ represents the Caputo's fractional time-derivative of order α , with $\alpha \in [0,1]$, defined over the time interval $(0,t)$, C_α is a frequency-depending coefficient re-written by following Koeller [73]

$$C_\alpha = c_{0G}\left(\frac{c_{1\mu}}{c_{0G}}\right)^\alpha \quad (2.23)$$

while the dissipative and the inertial terms were included by assuming for them the following simplest form

$$c_{1SP} = (1-\alpha)c_{1G}, \quad c_{2SP} = c_{2G}\left(1 + \alpha\frac{9p}{2}\sqrt{\frac{2\nu}{\omega R^2}}\right) \quad (2.24)$$

in this way obtaining that in the limit cases, say $\alpha = 0$ and $\alpha = 1$, the Or and Kimmel [103] elastic and viscous models are respectively reproduced.

Therefore, by substituting eq. (2.22) into eq. (2.5) and additionally exploiting the fractional derivative rule which leads to Laplace transform preserving the ordinary (integer) derivative law for the Laplace variable s - i.e. ${}_0^C D_t^\alpha \xrightarrow{\mathscr{L}} s^\alpha$ - the Spring-Pot frequency response of the system is finally obtained in terms of relative displacement as follows

$$\forall\alpha \in [0,1], |\Delta U|\Big|_{s=i\omega} = \left|\frac{\frac{4}{3}\pi\gamma\rho_{ob}R^3 s V_m}{\left(\frac{4}{3}\pi\rho_{ob}R^3 + c_{2SP}\right)s^2 + c_{1SP}s + C_\alpha s^\alpha}\right|\Bigg|_{s=i\omega} \quad (2.25)$$

2.1.3.2 *Generalized standard linear Kelvin model incorporating Spring-Pot systems*

Among fundamental viscoelastic schemes, Standard linear Kelvin (SLK) models are often used to enrich Voigt and Maxwell ones by building up in series a Voigt system and an elastic spring. An alternative to this configuration is represented by the Maxwell-Wiechert model - a Maxwell system in parallel with an elastic spring - from which the most general form of linear viscoelastic scheme can be derived through the Prony series method. However, both the above mentioned models can be seen as special cases of the so-called Standard Linear Solid (SLS) systems [127]. Since Spring-Pot can be physically thought as a viscoelastic system with the special capability of smoothly generating intermediate behaviors as the constitutive parameter α moves from zero (purely elastic behavior) to one (purely viscous behavior), a generalized SLK model is here defined by substituting a spring-pot to each dashpot and spring in the classical SLK model, as illustrated in Figure 2.1. In this straightforward way, by also suitably including the additional terms of *virtual friction* and *added mass*, a powerful low-parameter linear viscoelastic system is finally obtained and the related in-frequency response derived in closed-form: as a result, all the above mentioned simpler viscoelastic schemes and analytical solutions, including those given in [103], are found as limit or special cases of this generalized spring-pot based SLK system.
Therefore, let us consider the generalized quasi-SLK model as illustrated in Figure 2.1. Due to the configuration of spring-pot elements, it is possible to write forces and displacements as follows

$$f_{SLK} = f_P = f_{SP3} \tag{2.26}$$

$$\Delta u_{SLK} = \Delta u_P + \Delta u_{SP3} \tag{2.27}$$

where f_{SLK} is the resultant force of the entire system, $f_P = f_{SP1} + f_{SP2}$, f_{SP1}, f_{SP2} and f_{SP3} representing the forces due to the three spring-pots shown in Figure 2.1, whose explicit expressions are given in eqn (2.22). Also, the terms appearing in (2.27) are the displacements, being $\Delta u_P = \Delta u_{SP1} = \Delta u_{SP2}$.
By Laplace transforming f_P and f_{SP3}, fractional derivative rule ${}_0^C D_t^\alpha \xrightarrow{\mathscr{L}} s^\alpha$ gives

$$F_P = \left[C_{\alpha 1} s^{\alpha 1} + C_{\alpha 2} s^{\alpha 2} + \left(c_{1SP1} + c_{1SP2}\right) s + \left(c_{2SP1} + c_{2SP2}\right) s^2\right] \Delta U_P \tag{2.28}$$

$$F_{SP3} = \left[C_{\alpha 3} s^{\alpha 3} + c_{1SP3} s + c_{2SP3} s^2\right] \Delta U_{SP3} \tag{2.29}$$

After standard manipulations it is possible to obtain

$$\Delta U_P = \frac{F_P}{C_{\alpha 1} s^{\alpha 1} + C_{\alpha 2} s^{\alpha 2} + \left(c_{1SP1} + c_{1SP2}\right) s + \left(c_{2SP1} + c_{2SP2}\right) s^2} \tag{2.30}$$

$$\Delta U_{SP3} = \frac{F_{SP3}}{C_{\alpha 3} s^{\alpha 3} + c_{1SP3} s + c_{2SP3} s^2} \tag{2.31}$$

By recalling F_{res} from eq. (2.5) one finally attains the analytical solution of the in-frequency response of the generalized SLK system is $|\Delta U_{SLK}|\Big|_{s=i\omega}$ where

$$\Delta U_{SLK} =$$

$$\frac{\gamma V_m \left[\frac{1}{s(c_{1SP1}+c_{1SP2})+s^2(c_{2SP1}+c_{2SP2})+C_{\alpha 1}s^{\alpha 1}+C_{\alpha 2}s^{\alpha 2}} + \frac{1}{s(c_{1SP3}+c_{2SP3}s)C_{\alpha 3}s^{\alpha 3}}\right]}{\left[\frac{1}{(c_{1SP1}+c_{1SP2})+s^2(c_{2SP1}+c_{2SP2})+C_{\alpha 1}s^{\alpha 1}+C_{\alpha 2}s^{\alpha 2}} + \frac{1}{(c_{1SP3}+c_{2SP3}s)+C_{\alpha 3}s^{\alpha 3}}\right] - \frac{1}{\frac{4}{3}\pi\rho_{ob}R^3 s^2}} \tag{2.32}$$

	Parameters					
Models	α_1	C_{α_1}	α_2	C_{α_2}	α_3	C_{α_3}
Elastic	0	$\to\infty$	-	-	0	c_{0G}
Viscous	0	$\to\infty$	-	-	1	$c_{1\mu}$
V	0	c_{0G}	1	$c_{1\mu}$	0	$\to\infty$
M	0	$\to 0$	1	$c_{1\mu}$	0	c_{0G}
SLK	0	c_{0G}	1	$c_{1\mu}$	0	c_{0G}
SLK_1	0.5	$C_{0.5}$	1	$c_{1\mu}$	0	c_{0G}
SLK_2	0	c_{0G}	0.5	$C_{0.5}$	0	c_{0G}
SLK_3	0	c_{0G}	1	$c_{1\mu}$	0.5	$C_{0.5}$

Table 3: Synoptic frame illustrating how to set the parameters characterizing the proposed generalized quasi-standard linear Kelvin viscoelastic model, in order to replicate Elastic, Viscous, Voigt (V), Maxwell (M) and standard linear Kelvin (SLK) limit cases, as well as the three intermediate chosen configurations, say SLK_1, SLK_2 and SLK_3, employed to perform the subsequent analyses.

The obtained generalized SLK model, which also takes into account *virtual friction* and *added mass*, is then capable to reproduce all the viscoelastic models presented in [103], including viscous and elastic ones;

additionally, modulating the spring-pot parameters - say the order of the fractional derivative α - a vast number of viscoelastic "intermediate" systems might be obtained, as summarized in table 3 for some selected cases that will be afterwards used in the simulations.

2.2 SENSITIVITY ANALYSES: QUALITATIVE INSIGHTS AND RESONANCE HYPOTHESIS IN SINGLE-CELL DYNAMICS

With the aim of deriving both quantitative information and qualitative insights into the frequency response of single-cell systems through simple (one-degree of freedom) visco-elastic schemes, sensitivity analyses have been performed by generalizing some models successfully employed by [103]. To explore possible different behaviors and enrich the in-frequency responses of these single-cell systems, a wide class of viscoelastic paradigms have been in particular considered by introducing a new generalized SLK model and constructing related analytical solutions. To gain realistic physical results, mechanical properties of actual cells have been deduced from consolidated literature data and, to untie the key aspects of the cell response from the specific choice of the viscoelastic model, the sensitivity analyses have been conducted by querying different schemes.

Actually, to measure physical and in particular biomechanical properties at single-cell scale level (i.e. stiffness, ultimate strain, strength, toughness, etc) is a difficult and often challenging task. This is fundamentally due to several obstacles that might emerge when dealing with complex microstructures characterizing living systems, difficulties essentially arising from the fact that, during the test, intrinsic changes of the biological structure, movements of its mechanical apparatus and biochemical responses can all in principle interfere with the actual property to be measured. Furthermore, for example at single-cell scale, mechanical features may be drastically different from a site to another, as a consequence of reorganization dynamics activated by adhesion, migration and polymerization-depolymerization processes which change the internal configuration of the cytoskeleton and, as a result, may determine non homogeneous distribution of stiffness and deformation [3, 9, 116]. With this respect, Lekka et al [83] show, for instance, that depth of indentation, the substrate on which the cells are spread, the load rate as well as the position and time of cell poking might all influence the stiffness

AFM measurements. This implies that the physical measurements generally can be strongly dependent on the technique utilized and, as a consequence, quantitative estimations may cover wide ranges. Several experimental tests [11, 22, 23, 41, 70, 81–83, 85, 100, 113, 115] have in fact shown that the Young's modulus of the cytoplasm of different (healthy and cancer) cell lines can oscillate from about 100 Pa to 10 kPa. Also, the size of the cell nucleus is of the order of few micrometers and may depend on the cell size [37]. Further studies on the overall cell viscosity demonstrated that rheological properties may span over five orders of magnitude, probably as effect of the high dependence of the response on frequency bands and measurement techniques. Indeed, as highlighted in the paper by Or and Kimmel [103], while the viscosity of aqueous cytoplasm was found to be similar to that of water in fibroblasts, say $\mu = (1.3 \pm 0.1) \times 10^{-3}$ Pa×s [49], and slightly higher in smooth muscle cells, e.g. $\mu = (12.5 \pm 5.5) \times 10^{-3}$ Pa×s [129], the apparent viscosity of blood granulocytes was instead estimated to be substantially higher, with about $\mu = (210 \pm 100) \times 10^{-3}$ Pa×s [40].

This said, by taking into account the above mentioned literature experimental results which suggest that the measured mechanical features of cells can oscillate within wide ranges, the sensitivity analyses of the frequency response of single-cell units have been performed by making variable the overall cell Young modulus, the viscosity of the cytosol and the nucleus size in a way to cover the whole range spanned by the literature biomechanical data for different cell lines. Except for the information here utilized for parametrically describing the cell stiffness, the remaining physical data used for the analytical simulations are mainly referred to those suggested in [103].

Thus, with respect to the notations already introduced to describe the key parameters in the proposed generalized SLK visco-elastic model, all the analyses have been conducted by using vibration velocity amplitude of the medium $v_{m0} = 0.12$ ms^{-1} , derived for plain progressive wave with acoustic intensity of 1 W cm^{-2} to which is associated an intensity $I = 0.5\rho_m c v_{m0}^2$, with speed of sound $c = 1500$ ms^{-1} at room temperature [86]. The mass density of the medium has taken to be that of water at room temperature, the nucleus being considered 30% more dense than the environment, as generally assumed in literature [97].

In particular, the analyses have been performed by making reference to six representative viscoelastic schemes, say Voigt, Maxwell, SLK and three further generalized SLK models modified by respectively placing in position 1, 2 and 3 spring-pots with $\alpha = 0.5$, all enhanced by introduc-

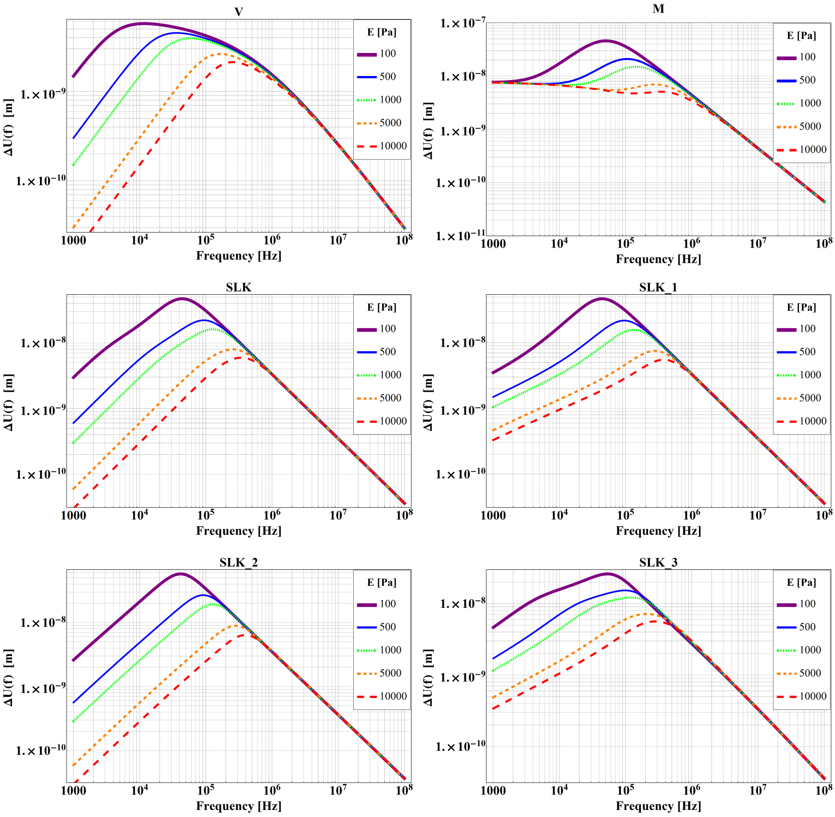

Figure 2.2: Sensitivity analysis for the frequency response of the cyclic displacement amplitude of a spherical object ($R = 1\ \mu$m) with respect to its surroundings with low viscosity ($\mu = 10^{-3}\,Pa \times s$) and varying Young modulus ($E = 100, 500, 1000, 5000, 10000\,Pa$): (**V**) Voigt; (**M**) Maxwell; (**SLK**) Standard Linear Kelvin; (**SLK_1**) generalized Standard Linear Kelvin with springpot in position 1, (**SLK_2**) 2 and (**SLK_3**) 3, with $\alpha = 0.5$.

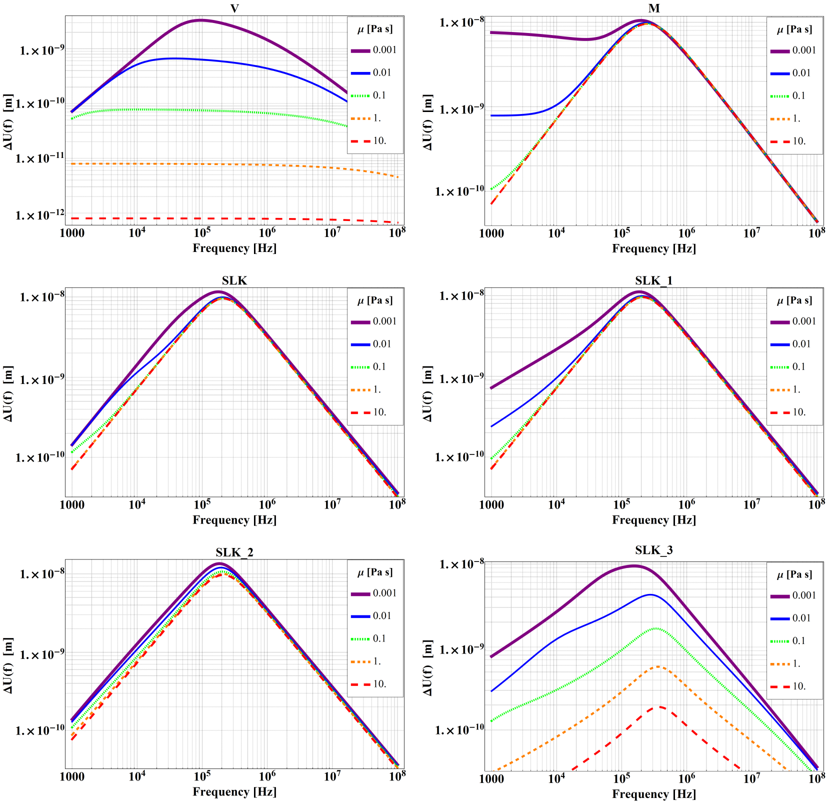

Figure 2.3: Sensitivity analysis for the frequency response of the cyclic displacement amplitude of a spherical object ($R = 1\,\mu m$) with respect to its surroundings with stiffness ($E = 2100\,Pa$) and varying viscosity ($\mu = \left[10^{-3} \sim 10\right]\,Pa \times s$): (**V**) Voigt; (**M**) Maxwell; (**SLK**) Standard Linear Kelvin; (**SLK_1**) generalized Standard Linear Kelvin with spring-pot in position 1, (**SLK_2**) 2 and (**SLK_3**) 3, with $\alpha = 0.5$.

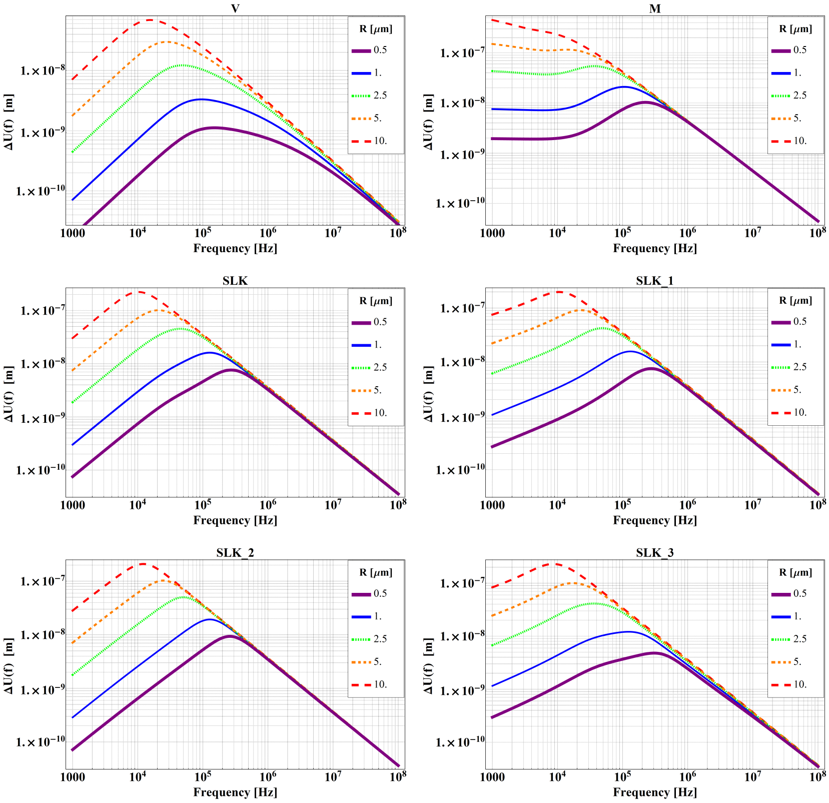

Figure 2.4: Sensitivity analysis for the frequency response of the cyclic displacement amplitude of a spherical object with respect to its surroundings with stiffness ($E = 2100\,\mathrm{Pa}$) viscosity ($\mu = 10^{-3}\,\mathrm{Pa}\times\mathrm{s}$) and varying size of the object ($R = 0.1, 1, 5, 10, 20\,\mu\mathrm{m}$): (**V**) Voigt; (**M**) Maxwell; (**SLK**) Standard Linear Kelvin; (**SLK_1**) generalized Standard Linear Kelvin with spring-pot in position 1, (**SLK_2**) 2 and (**SLK_3**) 3, with $\alpha = 0.5$.

ing the effects of *virtual friction* and *added mass*.

The analytical results have been obtained by making use of the symbolic code Wolfram Mathematica®and have been plotted in the frequency domain of interest for possible applications in biomedical engineering, that is $1\,\mathrm{kHz} \leq f \leq 100\,\mathrm{MHz}$, showing the frequency response of the systems in terms of relative displacement amplitude, $|\Delta U|$, which represents, in the time domain, the amplitude of the US induced relative oscillations between cell nucleus and environment.

The most significant results are all summarized in Figures 2.2, 2.3 and 2.4, where cell stiffness, viscosity and nucleus size have been separately assumed as varying over the ranges experimentally reported in the scientific studies, in each group of sensitivity analyses keeping fixed the other complementary parameters and choosing for them the most common values encountered in the literature, that is the Young modulus $E = 2100\,\mathrm{Pa}$ [23], the mean nucleus radius $R = 1\,\mu\mathrm{m}$ [20] and the viscosity of the water $\mu = 10^{-3}\,\mathrm{Pa}\times\mathrm{s}$, [103].

In particular, in Figure 2.2 the frequency response of the relative displacement between environment and the embedded spherical object representing the cell nucleus, with radius $R = 1\,\mu\mathrm{m}$, is shown by assuming low viscosity (i.e. $\mu = 10^{-3}\,\mathrm{Pa}\times\mathrm{s}$) and varying cell stiffness through five selected Young moduli, coherently deduced by literature and ranging from $E = 100\,\mathrm{Pa}$ to $E = 10\,\mathrm{kPa}$. Analogously, Figures 2.3 and 2.4 illustrate again the results in terms of displacement amplitude versus frequency, for the six viscoelastic models, respectively assuming stiffness fixed to $E = 2100\,\mathrm{Pa}$ and varying viscosity (choosing five values in the range $\mu = 10^{-3}\,\mathrm{Pa}\times\mathrm{s}$ to $\mu = 10\,\mathrm{Pa}\times\mathrm{s}$) and nucleus radii spanning the actual physical range, that is from $R = 0.5\,\mu\mathrm{m}$ to $R = 10\,\mu\mathrm{m}$.

The analytical outcomes obtained from the sensitivity analyses allow to highlight some relevant preliminary remarks which guide the subsequent simulations performed by specializing the viscoelastic models in order to discriminate mechanical frequency responses of healthy and cancer cells. In particular, the most significant results can be summarized in the following points.

First of all, some relevant qualitative behaviors can be recognized in the results shown in Figures 2.2, 2.3 and 2.4, all represented by plotting relative displacement amplitude versus frequency, that is: *i.* increasing peak frequencies and associated decreasing maximum displacements as stiffness of the system grows up (see Figure 2.2), *ii.* decreasing maximum displacement peaks with moderate frequency shifts as viscosity increases, with some slight differences in Voigt and SLK_3 models that leave however unaltered the trend, as shown in Figure 2.3, *iii.* increasing maximum displacement peaks with decreasing of corresponding frequencies as cell sizes grow (i.e. the nucleus radii increase), as illustrated in Figure 2.4. Importantly, with the exception of the sole limit cases (extremely large or small cell nuclei, significantly low elastic moduli and highest viscosity values), in all the investigated models, the results show that the peak frequency and the corresponding maximum vibrational amplitudes $|\Delta U|$ can be recognized to lie within the range $10^4 \sim 10^6$ Hz, an interval coherent with that found in the experiments by [66] and [80], which thus authorizes to think of obtaining resonance-like responses by stimulating cells by means of ultrasounds.

In agreement with Or and Kimmel outcomes [103], the obtained results derived by conducting the simulations with different viscoelastic models, where Young moduli variation has been additionally taken into account, confirm that mechanical (e.g. ultrasound-induced) vibrations $|\Delta U|$ are mostly comparable or greater than spontaneous thermal fluctuations. This happens for both the case of purely elastic solid, where - according to Ohshima and Nishio [102] - the Mean Square Displacement with respect to its equilibrium position can be analytically assumed to obey the equation $\langle u_{T,e}^2 \rangle = \dfrac{k_B T}{\pi R G}$, and viscous media, in which the Mean Relaxation Distance is $\langle u_{T,v} \rangle = \dfrac{2R^2 \rho_{ob} v_0}{9\mu}$ [72], where k_B is the Botzmann constant, T is the absolute temperature and v_0 is the initial velocity. To prove this numerically, it is sufficient to verify that, by making variable in the ranges of interest the cell nucleus radii and both the elastic and the viscous moduli appearing in the equations above recalled, the codomain of the square root of the Mean Square Displacement is $(2 \times 10^{-10}, 9 \times 10^{-9})$ and the codomain of the Mean Relaxation Distance is $(6 \times 10^{-15}, 2 \times 10^{-8})$, the upper bounds of both the intervals giving values comparable with or smaller than the peaks of mechanical vibrations amplitudes theoretically obtained from the sensitivity analyses (see Figures 2.2, 2.3 and 2.4).

Moreover, it has been experimentally demonstrated that cyclic loads at low frequencies, associated to strain levels in the range $(10^{-2}, 10^{-1})$, may induce mechanical and configurational alterations or rupture in living cells (see Table 1. in [103]). Analogous effects can be also observed at relatively high frequencies, in the case of ultrasound-stimulated cells, as experimentally shown by [80] and [99]. In particular, Mizrahi et al

[99] show that these physical changes are caused by very small strains (10^{-5}) at ultrasonic frequencies (10^6 Hz) and are close to those caused by relatively large strains (10^{-1}) at physiological frequencies (10^0 Hz). With respect to the present work, by taking into account the relative displacement peaks between cell nucleus and environment obtained from analytical results, a rough estimate of the equivalent uniaxial strain can be calculated as $\varepsilon \propto \dfrac{|\Delta U|}{(10 \times R)}$. Therefore, by considering that cell nuclei may vary within the range $\left(2 \times 10^{-7}, 10^{-5}\right)$ m and vibrational displacement amplitudes are found ranging from 10^{-9} m to 10^{-7} m (with the exception of the extreme cases of fluid-like behaviors), strains from 10^{-5} up to 10^{-1} can be reached. As a consequence, at the ultrasound frequencies (and/or by increasing the US radiation intensity), after a few seconds of exposure, cell configurational alterations or disruptions due to fatigue-like phenomena might be actually expected.

Importantly, the peak frequencies theoretically obtained by means of the implemented viscoelastic models may span from tens kHz to one MHz, both the frequency extreme values of this interval being involved as critical frequencies at which it has been experimentally observed that cells show relevant biological responses as a result of prevailing mechanical effects on thermal ones [66, 118].

Further details of the results can be however traced in the Figure's captions.

2.3 FREQUENCY-BASED DETECTION OF CANCER AND HEALTHY CELLS AT SINGLE-CELL LEVEL

On the basis of the sensitivity analyses, it has been above demonstrated - by means of theoretical arguments - that single-cells, modeled through different elementary viscoelastic systems, exhibit frequencies (from tens to hundreds kHz) associated to oscillation magnitude peaks which confirm that mechanical resonance-like phenomena induced by ultrasounds can be prevailing with respect to thermal fluctuations, a fact that also suggests that the cell structural response can be recognized as a candidate to play a key role to explain some experimentally observed biological effects [66, 80, 99, 118].

On the other hand, as recalled above, independent literature results have in the last years shown that, regardless of measurement techniques and cell lines, cancer cells are always significantly softer than their healthy counterparts, a fact ascertained among biologists (see Table 4). Given that there are very few common factors shared by tumor cells (this is the main reason of the success of molecular markers) this stiffness discrepancy between normal and tumor cells constitutes an extremely relevant property.

With the aim of both gaining information about the possibility of mechanically targeting healthy and cancer cells and quantitatively estimating the frequency bands at which detection could be in principle realized, in the present section the viscoelastic schemes, already utilized above for the sensitivity analyses, are specialized with reference to the stiffness values actually experimentally measured and reported in the literature for a number of healthy and cancer cell lines (see Table 4). In particular, as an example, Figure 2.5 illustrates how benign and tumor mesothelial cells extracted from carcinoma of the lung [23] would behave in terms of relative displacement amplitude versus frequency. The outcomes show that, in all the six examined viscoelastic models, the difference in stiffness between the cells results to be sufficient for recognizing corresponding significant frequency shifts defined as in-frequency distances between the resonance-like oscillation magnitude peaks. Importantly, a relevant difference is also reflected in the graphics of the obtained results in terms of relative displacement amplitudes, which would in principle ensure the possibility of selectively targeting tumor cells if - for example by means of ultrasounds - the radiation is applied at a prescribed intensity and at a frequency close to the *resonance-like* frequency of the cancer single-cell system, an effect amplified by the fact that, due to the above recalled frequency shift, the normal cell always exhibits a smaller displacement amplitude at the tumor critical frequency.

To stress this aspect, Figure 2.6 collects - in form of histograms - all the theoretical outcomes obtained by making reference to the viscoelastic properties experimentally measured in numerous independent literature works for six healthy and cancer cell lines (see Table 4). In particular, the results are summarized by highlighting - for each cell line - the difference of frequencies at which the oscillation amplitude peak occurs, in both cancer and healthy cells and averaging the results - for sake of simplicity - over each viscoleastic scheme adopted for performing the simulations. The bar-chart confirms the possibility of observing relevant differences, in terms of resonance-like frequencies, in comparing cancer and healthy cell mechanical responses, a fact registered for all the cell lines examined and regardless of the implemented viscoelastic model, and occurring at frequencies always compatible with LITUS.

Finally, by keeping in mind possible practical uses for targeting tumor

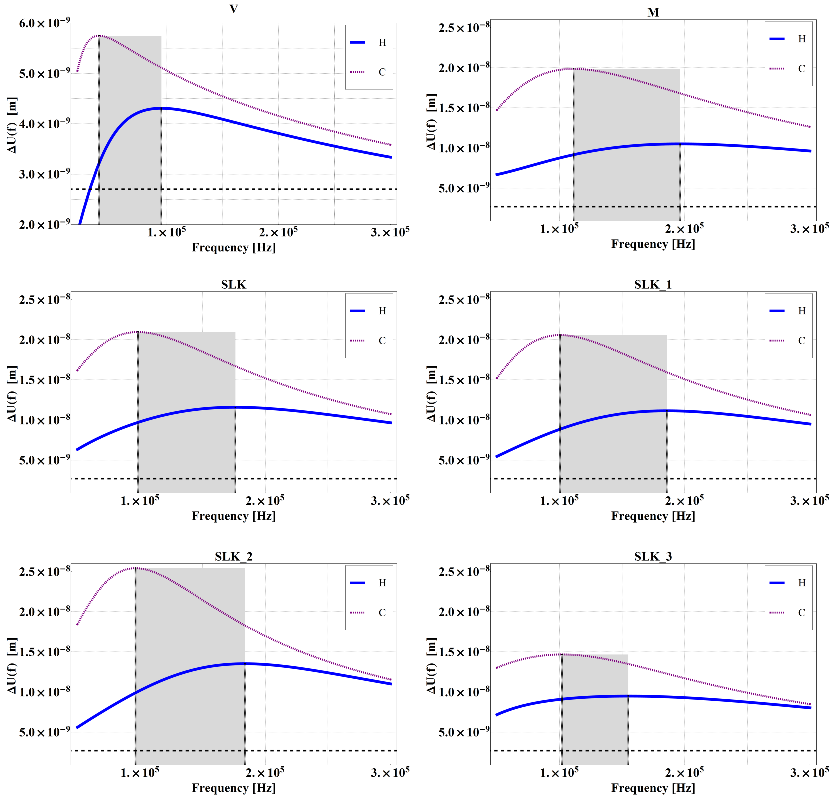

Figure 2.5: Frequency response, in terms of relative displacement amplitude vs frequency, of Healthy (H) and Cancer (C) mesothelial cells extracted from carcinoma of the lung, simulated through the proposed viscoelastic schemes: ($R = 1\,\mu m$; $\mu = 10^{-3}\,Pa \times s$; measured cancer Young modulus:$E = 560\,Pa$; measured healthy Young modulus: $E = 2100\,Pa$). The six graphics are reffered to the following models: (**V**) Voigt; (**M**) Maxwell; (**SLK**) Standard Linear Kelvin; (**SLK_1**) generalized Standard Linear Kelvin with spring-pot in position 1, (**SLK_2**) 2 and (**SLK_3**) 3, with $\alpha = 0.5$. The grey regions highlight the difference in frequency between peaks in cancer and healthy cells. Dashed lines represent the displacement amplitudes corresponding to the thermal fluctuations, always smaller than the mechanical ones.

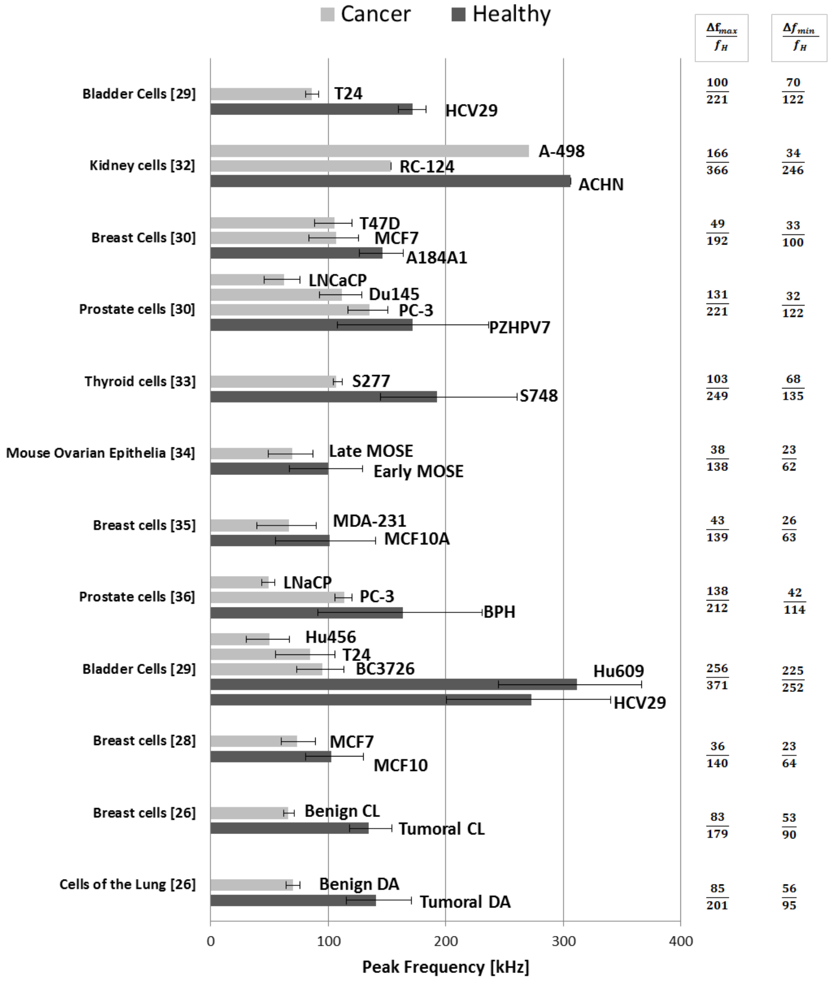

Figure 2.6: Bar-chart with synopsis of the theoretically derived in-frequency responses of healthy and cancer cells whose mechanical properties have been experimentally measured: the histograms compare peak frequencies for each tumor and normal cell line pair examined, by averaging over all the results obtained from the six viscoelastic schemes utilized. The first column reports the cell type and the corresponding literature reference from which the data are deduced; the last two columns give some quantitative results in terms of ratio between maximum ($\frac{(\Delta f)_{max}}{f_H}$) and minimum frequency shifts ($\frac{(\Delta f)_{min}}{f_H}$) over the reference resonance-like frequency of the healthy cell, for each cell line.

cells, the last columns in 2.6 report a synopsis of the most important quantitative results obtained from the performed analyses, showing that both the ratios $\frac{\Delta f}{f_H}$ between maximum and minimum frequency shifts $\Delta f = f_H - f_C$ over reference healthy resonance frequency f_H, (occurring in the cases at hand with respect to SLK_1 and Voigt viscoelastic models) would allow in principle to quantitatively discriminate the peak frequencies in a real case. As a matter of fact, the reference healthy frequencies f_H are indeed about $40 \sim 400$ kHz, while the frequency shifts oscillate between about $20 \sim 250$ kHz. This seems to explain the experimental findings in [80] and also to suggest that, for a practical (therapeutic) purpose, a biomedical device could be designed to selectively determine ultrasound-induced large vibrations in tumor cells, once wave frequencies were tuned from 25% to 60% of the reference healthy frequency.

2.4 ELEMENTAL NONLINEAR ELASTIC MODEL OF AN ADHERENT CELL

Influence of prestress and number of cytoskeleton filaments on the single-cell stiffness

With the aim of deriving the effect of the pre-stretch accumulated in the cytoskeleton filaments on the overall single-cell stiffness, in this section it is presented a simple non-linear elastic model of the cell structure in which the essential features responsible for the mechanical response of the ensemble (e.g., cytoskeleton protein filaments, cell nucleus and interface conditions with a rigid substrate –say the extra-cellular matrix, ECM) are taken into account, in this manner determining the cell elasticity via a *bottom-up* procedure.

To this purpose, let us consider the sketch in Figure 2.7. Therein, starting from a generally unknown initial stress-free configuration (Figure 2.7a), the cell is assumed to be in an actual prestretched configuration (say adherent to the ECM, as shown in Figure 2.7b), and then subjected to a small displacement of its nucleus (Figure 2.7c). In this scheme, as highlighted in the lateral view (see Figure 2.7), the cell cytoskeleton is modeled through a structure made of symmetrically and radially placed non-linear elastic filaments (or filament strands) anchored to the central nucleus and to the substrate through the focal adhesion points, in this

Investigator	Year	Cell Line	Stiffness [kPa] ± SD	
			Healthy	**Cancer**
1. Lekka et al. [83]	2012	Human Bladder HCV29	3.09 ± 0.42	
		Human Bladder T24		0.83 ± 0.27
2. Rebelo et al [115]	2013	Human Kidney non-tumorigenic RC-124	9.38	
		Human Kidney carcinoma A-498		7.41
		Human Kidney adenocarcinoma ACHN		2.48
3. Lekka et al. [82]	2012	Human Prostate non-tumorigenic PZHPV7	3.09 ± 0.28	
		Human Prostate metastatic carcinoma LNCaP		0.45 ± 0.21
		Human Prostate metastatic carcinomaa Du145		1.36 ± 0.42
		Human Prostate adenocarcinoma PC-3		1.95 ± 0.47
		Human Breast Normal A184A1	2.26 ± 0.56	
		Human Breast Cancer T47D		1.20 ± 0.28
		Human Breast Adenocarcinoma MCF7		1.24 ± 0.46
4. Prabhune et al [113]	2012	Human Thyroid S748	$2.211 \sim 6.879$	
		Human Thyroid anaplastic carcinoma S277		$1.189 \sim 1.365$
5. Ketene et al [70]	2012	Mouse Early Ovarian surface Epithelia MOSE		0.549 ± 0.281
		Mouse Late Ovarian surface Epithelia MOSE		1.097 ± 0.632
6. Nikkhah et al [100]	2010	Human Breast normal mammary epithelium MCF10A	1.13 ± 0.84	
		Human Breast metastatic tumor MDA-231		0.51 ± 0.35
7. Faria et al [41]	2008	Human Prostate Benign BPH	2.797 ± 0.491	
		Human Prostate adenocarcinoma PC-3		1.401 ± 0.162
		Human Prostate metastatic carcinoma LNCaP		287 ± 52
8. Lekka et al [81]	1999	Human Epithelial normal Hu609	9.7 ± 3.6	
		Human Epithelial normal HCV29	7.5 ± 3.6	
		Human Epithelial cancerous Hu456		1.0 ± 0.6
		Human Epithelial cancerous T24		0.8 ± 0.4
		Human Epithelial cancerous BC3726)		0.3 ± 0.2
9. Li at al [85]	2008	Human Breast Epithelial non malignant MCF10	1.15 ± 0.52	
		Human Breast Epithelial malignant (MCF-7)		0.614 ± 0.237
10. Cross et al. [23]	2007	Human Lung Benign carcinoma	2.10 ± 0.79	
		Human Lung Tumoral carcinoma		0.56 ± 0.09
		Human Brest Benign ductal adenocarcinoma	1.93 ± 0.50	
		Human Brest Tumoral ductal adenocarcinoma		0.5 ± 0.08

Table 4: Actual stiffness for different lines of healthy and cancer cells, measured by means of several techniques, as precised in the references reported in the first column.

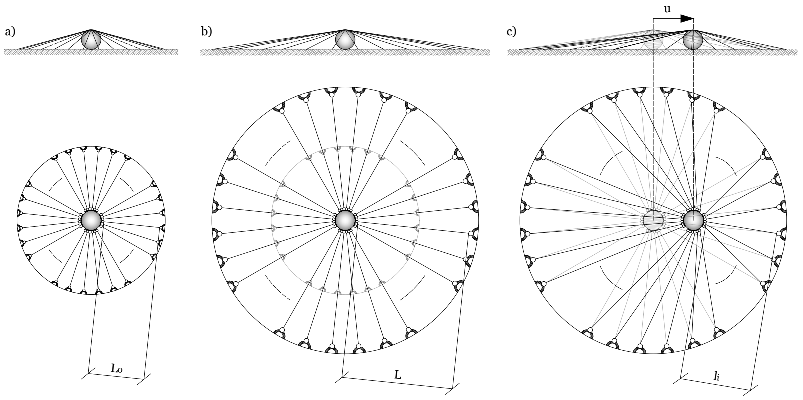

Figure 2.7: Cartoon –with plan and lateral views– of the elemental cell cytoskeleton structure: a) initial (stress-free) unknown configuration; b) adherent cell with non-linearly prestretched/prestressed filaments (reference configuration); c) *small-on-large* cell deformation induced by nucleus displacement (current configuration)

way implicitly assuming that the cell membrane follows the overall geometry of the model. Also, for sake of simplicity, the entire kinematics is projected in the horizontal plane (say the plane defined by the focal adhesion points), so neglecting the minor effects of stress and strain aliquots associated to the out-of-plane filament elongations caused by the cell stretching. In particular, a reference prestretch (denoted by λ_p) characterizes the deformed configuration in which the nucleus is constrained by n elastic strings –representing the actin filaments– arranged uniformly around the nucleus and identified by an angle $\phi_{j0} = j\frac{2\pi}{n}$.
To find how the cell structure influences the overall cell stiffness when its filaments are prestressed, by making reference to a *small-on-large* approach, the nucleus is displaced of u in an arbitrary (say horizontal) direction: as a consequence, maintaining prescribed the focal adhesion points, each filament will result to be stressed to follow the nucleus and the corresponding Piola-Kirchhoff stress tensor can be generally written as

$$\mathbf{P}_j = \begin{pmatrix} P_{Lj} & 0 & 0 \\ 0 & P_{Tj} & 0 \\ 0 & 0 & P_{Tj} \end{pmatrix} \tag{2.33}$$

where –for the *-jth* filament– P_{Lj} denotes the longitudinal stress component and P_{Tj} is the transverse stress one, in this case to be set equal to zero. Once the force f_u to be applied to the nucleus for obtaining the displacement u is determined, the related equivalent tangent stiffness can be formally derived as follows

$$K_{eq} = \left.\frac{\partial f_u}{\partial u}\right|_{u=0} \tag{2.34}$$

Obviously, the force f_u – the resultant of the axial forces of the n filaments (see Figure 2.8) – will depend on u, the prestretch λ_p of each single filament, the initial stiffness (related to the stress-free configuration), the geometrical parameters, the number n of filaments and the constitutive assumption, say the type of hyperelastic law chosen fot the strings. Therefore, one has

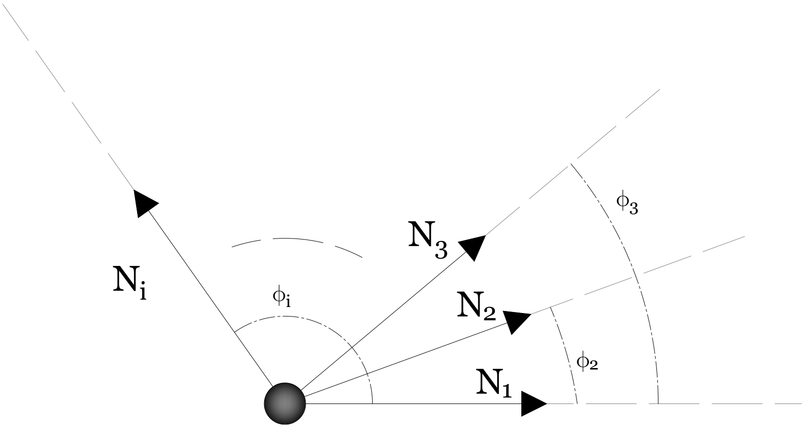

Figure 2.8: Illustration of how the axial forces kindled in each string contribute to the equilibrium of the nucleus: the angles ϕ_j are referred to the actual (displaced) nucleus position.

$$f_u + \sum_{j=1}^{n} N_j \cos(\phi_j) = 0 \tag{2.35}$$

where $N_j = P_{Lj}A$ is the contribute of the *-jth* filament due to the longitudinal stress times the reference cross-section area $A = A_j$ and ϕ_j is the angle of the *-jth* filament in its current configuration.

The constitutive model for the strings is here fixed by following [61], in the case of compressible Neo-Hookean solids in which the Strain Energy Density Function (SEDF) is written in terms of the first invariant, I_1, of the right Cauchy-Green tensor $\mathbf{C} = \mathbf{F}^T\mathbf{F}$ (chosen as measure of the deformation) which in the so-called coupled form – where the isochoric and volumetric parts are interacting – is given by:

$$\Psi_{NH} = \frac{G}{2}(I_1 - 3) + \frac{G}{2\beta}\left(J^{-2\beta} - 1\right) \quad \text{with} \quad \beta = \frac{\nu}{1 - 2\nu} \tag{2.36}$$

where $J = det\mathbf{F}$ and G and ν denote the shear modulus and the Poisson's ratio, respectively. The principal stresses will hence depend on the principal stretches in the form

$$P_j = \frac{\partial \Psi_{NH}}{\partial \lambda_j} \tag{2.37}$$

and furthermore

$$P_{Lj} = G\left(\lambda_{Lj} - \frac{\left(\lambda_{Lj}\lambda_{Tj}^2\right)^{\frac{2\nu}{2\nu-1}}}{\lambda_{Lj}}\right), \tag{2.38}$$

$$P_{Tj} = G\left(\lambda_{Tj} - \frac{\left(\lambda_{Lj}\lambda_{Tj}^2\right)^{\frac{2\nu}{2\nu-1}}}{\lambda_{Tj}}\right) \tag{2.39}$$

Algebraic manipulations lead to observe that prescribing uniaxial stress states in each filament ($P_{Tj} = 0$) reduces to impose $\lambda_T = \lambda_L^{-\nu}$, finally obtaining the longitudinal stress as follows

$$P_{Lj} = G\lambda_{Lj}\left(1 - \lambda_{Lj}^{-2(1+\nu)}\right) \tag{2.40}$$

The total stretch in the generic *-jth* filament strand can be multiplicatively written as:

$$\lambda_{Lj} = \lambda_p \lambda_{uj} \tag{2.41}$$

in which $\lambda_p = \dfrac{L}{L_0}$ is the initial prestretch related to the current filament length L referred to the initial configuration L_0 –whose values are here assumed to be the same for all the elements due to the symmetry of the initial cell shape – λ_{uj} being the stretch of the *-jth* string due the displacement u and explicitly given by

$$\lambda_{uj} = \frac{\sqrt{L^2 \sin^2\phi_j + (L\cos\phi_j - u)^2}}{L} \tag{2.42}$$

where

$$\begin{aligned} \sin\phi_j &= \frac{L\sin\phi_{j0}}{\sqrt{L^2\sin^2\phi_{j0} + (L\cos\phi_{j0} - u)^2}}, \\ \cos\phi_j &= \frac{L\cos\phi_{j0} - u}{\sqrt{L^2\sin^2\phi_{j0} + (L\cos\phi_{j0} - u)^2}} \end{aligned} \tag{2.43}$$

Finally, by substituting eqs (2.40) and (2.35) into (2.34), after some further algebraic manipulations, one obtains the stiffness K which varies with the displacement u as follows

$$K = -GA\lambda_p \sum_{j=1}^{n} \Bigg[(1 + (1+2\nu)\lambda_p^{-(1+2\nu)} \lambda_{uj}^{-2(1+\nu)}) \cos\phi_j \frac{\partial \lambda_{uj}}{\partial u} - \\ (\lambda_{uj} - \lambda_p^{-2(1+\nu)} \lambda_{uj}^{-(1+2\nu)}) \sin\phi_j \frac{\partial\ \phi_j}{\partial u}) \Bigg] \tag{2.44}$$

from which one finally has

$$K_{eq} = K\Big|_{u=0} = GAL^{-1}\lambda_p \sum_{j=1}^{n} (1 + \lambda_p^{-2(1+\nu)} (\nu + (1+\nu)\cos 2\phi_{j0})) \tag{2.45}$$

that represents the analytical form –explicitly depending on both the geometrical and mechanical parameters– of the tangent stiffness of the adherent single-cell structure, associated to the imposed displacement u. It is worth to notice that, from (2.45) and for an arbitrary couple of filaments with prescribed angles ϕ_{j0} and $\phi_{j0} + \pi$ respectively, the prestretch influences the stiffness in a non linear way, whose form depends on the Poisson'ratio ν. It is then natural to ask if the stiffness is monotonic with the prestretch. By calculating the derivative of the *j-th* addend (and its coaxial) in K_{eq}, say K_{eqj}, with respect to λ_p and equating it to zero, one finds

$$\frac{\partial K_{eqj}}{\partial \lambda_p} = GAL^{-1} \cos\phi_{j0}\lambda_p \left(1 + (1+2\nu)\lambda_p^{-2(1+\nu)}\right) = 0 \tag{2.46}$$

whose in closed-form solution is

$$\lambda_p = |1 + 2\nu|^{\frac{1}{1+\nu}} \tag{2.47}$$

which gives compatible (positive) stretches for any angle ϕ_{j0} and Poisson ratios belonging to the classical thermodynamically consistent range $]-1, \frac{1}{2}[$.

From the biomechanical point of view, this enough counter-intuitive result implies that, as the stiffness varies with increasing prestretches, a minimum must be found (see Figure 2.9) and thus –at least in principle– during a monotonic stretching of the substrate or in searching optimal cytoskeleton configuration, an adherent cell could find minimal energy positions at *nonzero* strains as well.

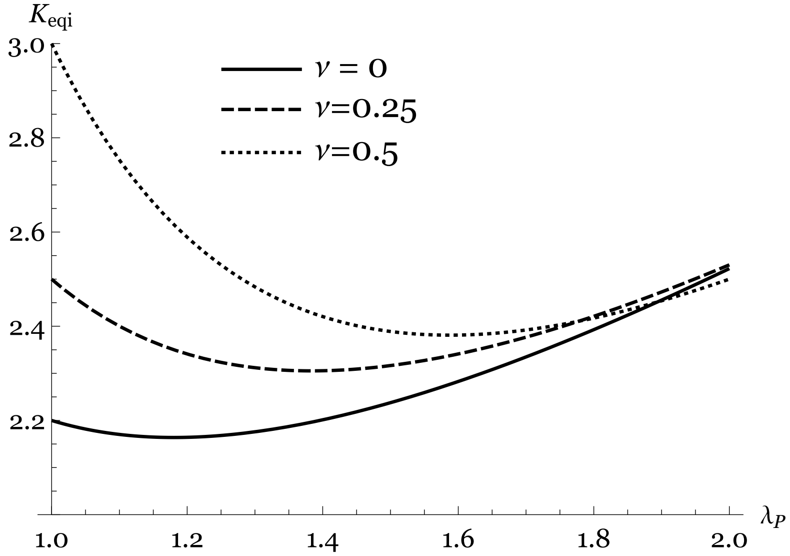

Figure 2.9: Plot of the dimensionless contribution of a filament to the cell stiffness as function of the prestretch: note that –for different Poisson's ratio values– a minimum is always highlighted.

Identification of the model parameters to describe actual cell stiffness

The above nonlinear elastic model has been introduced to quantitatively estimate the effect of prestress and number of filaments on the overall stiffness of an adherent (prestretched) single cell. With reference to the experimentally measured cell stiffness values (see for a synoptic frame the tables in [44]) and by making use of (2.45), it is possible to determine the equivalent overall elastic Young modulus of the cell in an arbitrary prestretched configuration, E_{eq}, by considering incompressibility condition –that is $G \simeq \frac{E}{3}$, G being the first Lamé modulus– as follows (the symbol $C_{0G} = 6\pi GR$ will be afterwards used for the stiffness)

$$E_{eq} \simeq \frac{3K_{eq}}{6\pi R} \tag{2.48}$$

where R represents the cell nucleus radius, as reported by [103]. This expression –which will be used in the following viscoelastic schemes– implicitly takes into account the prestretch as well as the number of filaments, all these parameters being included in K_{eq}. As a consequence, the formula furnishes a direct first estimation of the equivalent cell Young modulus E_{eq} –once all the mechanical and geometrical parameters are known– but, because of its elementary structure, it can be also used to identify the number of "active" cytoskeleton elements in an experimental measurement, as well as to determine the average prestress of an adherent cell.

In Figure 2.10 are illustrated the results of the parametric analyses conducted on the equivalent stiffness for three values of the Poisson's ratio of the filaments ($\nu = 0, 0.25, 0.5$), initial filament length L_0 equal to 50 μm and circular cross sections with diameters of 7 nm, all these values being coherent with the literature data. In particular, the equivalent cell Young moduli of a cell have been carried out by both considering 75 active protein filaments for a single cell strand, making variable the prestretch (see Figure 2.10a), and complementary prescribing a prestretch ($\lambda_p = 1.3$), thus plotting the cell stiffness against the number of filaments (see Figure 2.10b). Both the graphics show how the whole range of elastic moduli measured through different techniques and reported in the literature for a vast class of cell lines ([44]) can be obtained with a good agreement, modulating the prestretch and the number of "active" filaments within experimentally documented intervals. An instructive numerical example can be easily done by considering the case of cell stiffness measured by Cross et al [22] for human healthy cells and corresponding abnormal carcinoma of the lung, estimated about 2100 Pa and 560 Pa, respectively. In this case, setting $\nu = 0.4$, the stiffer value associated to the healthy cells can be obtained through the proposed model by assuming a prestretch $\lambda_p = 1.32$ and considering $n = 75$ active protein filaments, the cancer cell elastic modulus being caught by merely reducing to about 26 the number of active filaments to simulate possible lower levels of polymerization in the cytoskeleton structure of cancer cells to facilitate squeezing and metastatic migration abilities.

THE RESONANCE HYPOTHESIS IN ADHERENT CELLS: THE ROLE OF PRESTRETCH AND NUMBER OF ACTIVE CYTOSKELETON FILAMENTS

With reference to the (one-degree of freedom) visco-elastic schemes presented in Section 2.1 in which the the in-frequency response of single-cell systems has been in detail analyzed through sensitivity analyses aimed to gain information about positioning and magnitude of the response peaks for envisaging possibilities of exploiting the stiffness discrepancies experimentally observed between healthy and tumor cells for

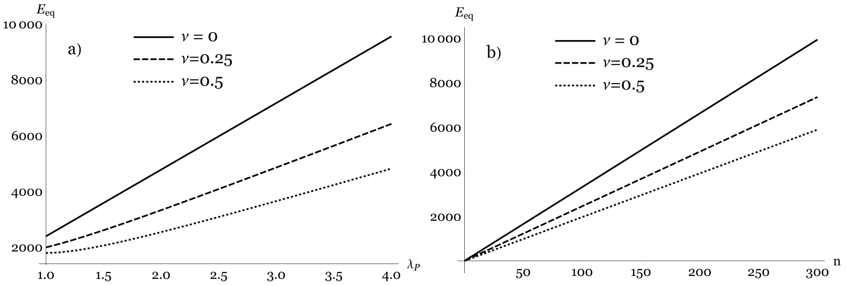

Figure 2.10: Parametric analyses for the equivalent Young modulus of a single-cell system for different Poisson's ratios: a) elastic stiffness versus prestretch with fixed number of active filaments (75); b) elastic stiffness versus number of (active) filaments, with prescribed prestretch value ($\lambda_p = 1.3$).

mechanically targeting and selectively attacking cancer cells. To make this It has been explored the in-frequency responses of a wide class of viscoelastic single-cell paradigms, by *ad hoc* introducing a new generalized *fractional derivative*–based SLK model and constructing the related analytical solutions, whose results were referred to ranges of mechanical properties and physical parameters actually measured at single-cell level and reported in the consolidated literature.

However, when dealing with living systems, the measures of stiffness can be significantly affected by intrinsic structural changes of the biological matter, for example by the reorganization dynamics guided by polymerization-depolymerization processes which change the internal configuration of the cytoskeleton, so regulating adhesion and migration cell capabilities and in turn provoking non homogeneous cell deformations and changes in stiffness ([3, 9, 116]), with Young's moduli also oscillating from about 100 Pa to 10 kPa ([11, 22, 23, 41, 70, 81–83, 85, 100, 113, 115]).

Nevertheless, the vast majority of the experimental data somewhat considers stiffness of "round" (suspended) cells and –at the best authors knowledge– no many efforts have been devoted, from the modeling standpoint, to mechanically relate the overall change of cell stiffness to its stretched configuration, as well as to the average number of active/assembled cytoskeletal filaments.

Therefore, by starting from the literature experimental results and taking into account the ranges within which actual measured mechanical features of cells can oscillate, the overall stiffness –determined from the proposed elemental non-linear elastic single-cell model– has been introduced into the fractional derivative–based SLK scheme. In this way, the cell visco-elastic behavior explicitly depends, among other geometrical and physical parameters, upon the stiffness resulting from the number of active cytoskeletal filaments, their prestretch level due to possible adherent configurations, as well as from the *round shape*–associated cell Young modulus, directly related to the cell line and to the cell (i.e. healthy or cancer) state.

To highlight the possibility of following the above described strategy for representing the whole range of the experimentally measured single-cell mechanical properties, in both suspended and adherent conditions, also demonstrating that viscoelaatic response peaks still fall within frequencies intervals of ultrasound which would still preserve the possibility of of selectively inducing resonance-like phenomena in cells ([44]), sensitivity analyses have been thus *ad hoc* performed by making variable the overall intrinsic round-shaped cell Young modulus, the prestretch and the number of active micro-filaments, the cytosol viscosity and the nucleus size being prescribed and set equal to average values, in this manner covering the entire range of the mechanical data given in the literature for many cell lines investigated.

By essentially following data and methods already introduced in [44] and with respect to the notations proposed for the generalized SLK visco-elastic systems, the analyses reported below have been conducted by assuming medium vibration velocity magnitude $v_{m0} = 0.12$ ms^{-1}, determined in case of plain progressive waves characterized by acoustic intensity of 1 W cm^{-2} and associated intensity $I = 0.5\rho_m c v_{m0}^2$, $c = 1500$ ms^{-1} being the speed of sound at room temperature ([86]) at which mass density of the medium has been also assumed to be coincident with that of the water, the nucleus –as reported in ([97])– being considered about 30% more dense than the environment.

More specifically, the performed analyses have been referred to six selected viscoelastic schemes, that is the enhanced Voigt, Maxwell and SLK ones and further three generalized fractional derivative–based SLK models constructed by positioning in the sections 1, 2 and 3 spring-pots with $\alpha = 0.5$ (see Figure 2.1), in all the cases also taking into account *added mass* and *virtual friction* effects. Additionally, the elastic modulus G appearing in the fractional derivative–based models implicitly takes into account the cell configuration (suspended and adherent) through prestretch and number of active filaments determined by eqs. (2.45) and (2.48). The theoretical outcomes have been carried out by making the calculations using the symbolic commercial code Wolfram Mathematica®([**Wolfram2003**]) and the results have been repre-

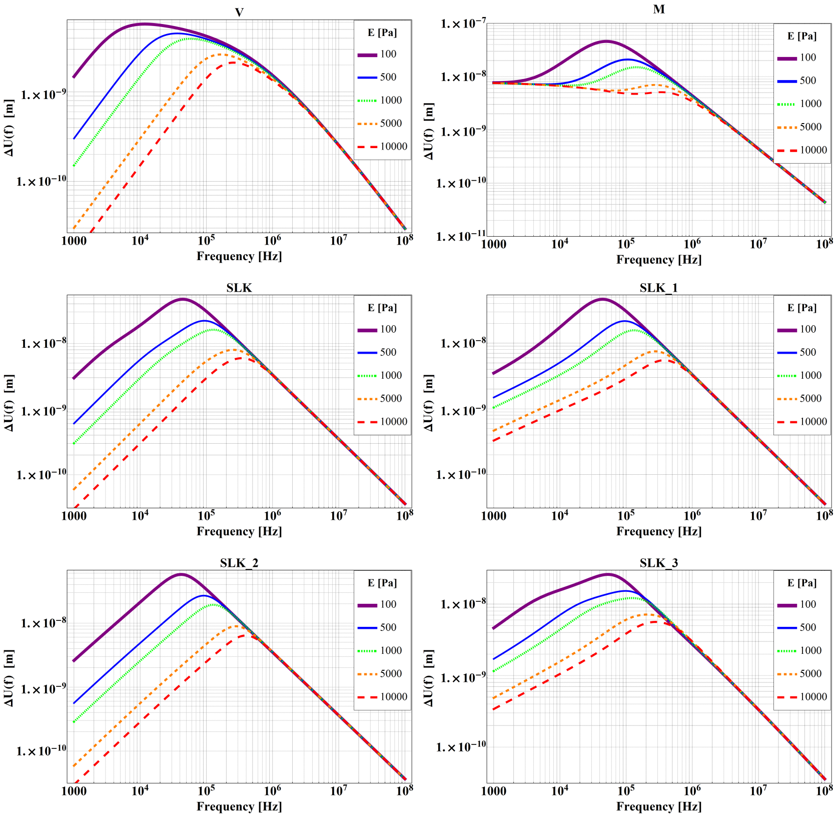

Figure 2.11: Sensitivity analysis for the frequency response of the cyclic displacement amplitude of a spherical object ($R = 1\ \mu m$) with respect to its surroundings with prescribed viscosity ($\mu = 10^{-3}\, Pa \times s$) and varying Young modulus ($E = 100, 500, 1000, 5000, 10000\, Pa$): (**V**) Voigt; (**M**) Maxwell; (**SLK**) Standard Linear Kelvin; (**SLK_1**) generalized Standard Linear Kelvin with spring-pot in position 1, (**SLK_2**) 2 and (**SLK_3**) 3, with $\alpha = 0.5$.

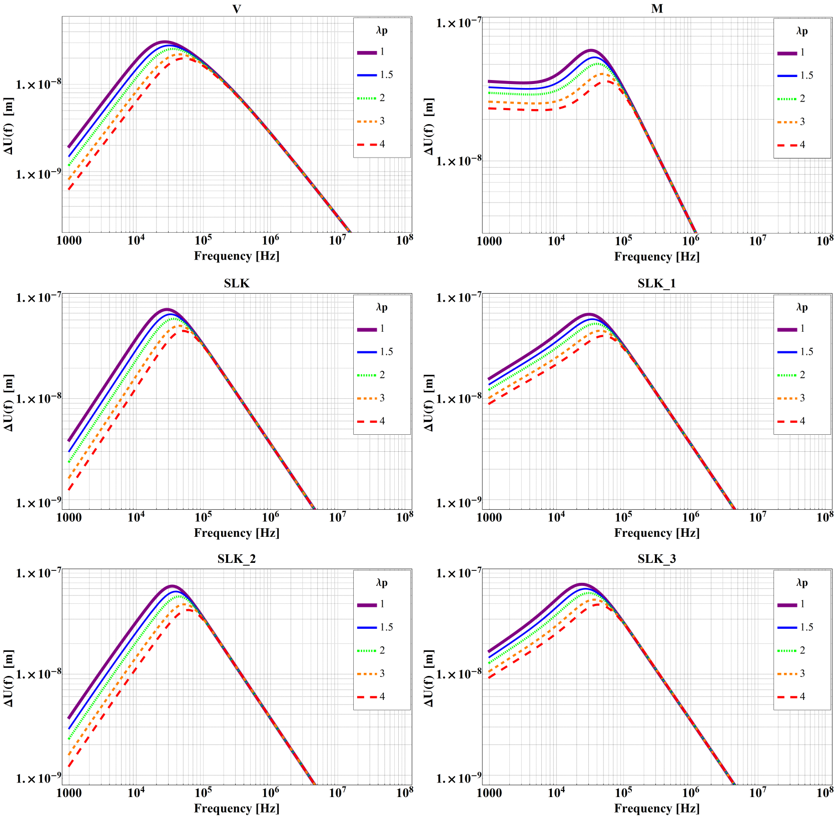

Figure 2.12: Sensitivity analysis for the frequency response of the cyclic displacement amplitude of a spherical object ($R = 1\ \mu$m) with respect to its surroundings with prescribed viscosity ($\mu = 10^{-3}\,Pa \times s$), tangent Young modulus ($E = 2.6 \times 10^9 Pa$) and Poisson ratio ($\nu = 0.4$) of the microfilaments, for a fixed number of active filaments ($n = 50$), varying the level of prestretch ($\lambda_p = 1, 1.5, 2, 3, 4$): (**V**) Voigt; (**M**) Maxwell; (**SLK**) Standard Linear Kelvin; (**SLK_1**) generalized Standard Linear Kelvin with spring-pot in position 1, (**SLK_2**) 2 and (**SLK_3**) 3, with $\alpha = 0.5$.

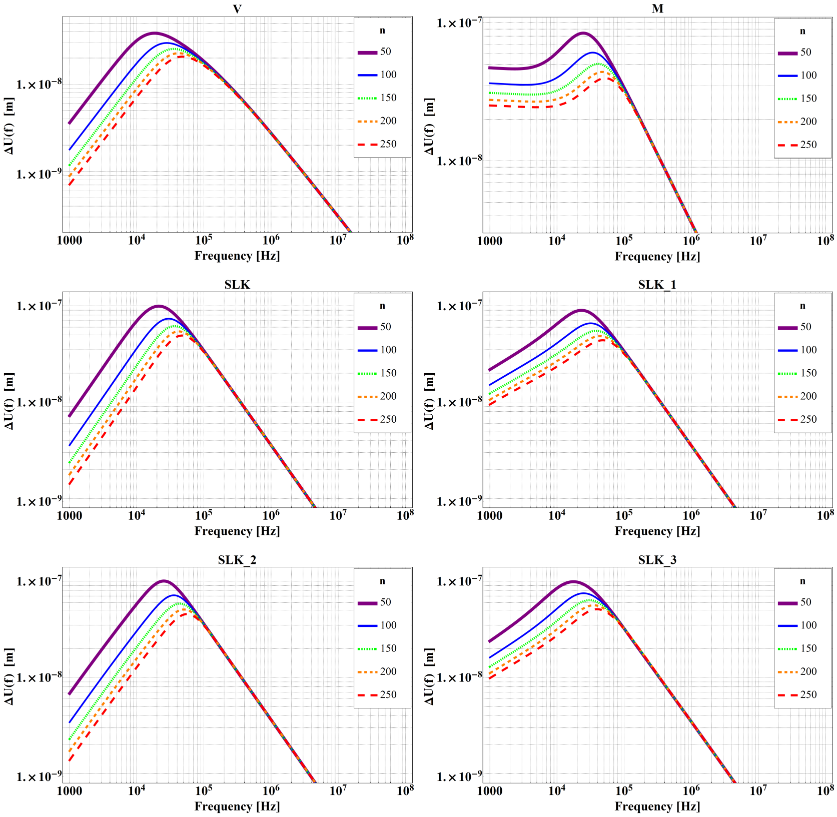

Figure 2.13: Sensitivity analysis for the frequency response of the cyclic displacement amplitude of a spherical object ($R = 1\ \mu$m) with respect to its surroundings with prescribed viscosity ($\mu = 10^{-3}\,Pa \times s$), tangent Young modulus ($E = 2.6 \times 10^{9} Pa$) and Poisson ratio ($\nu = 0.4$) of the microfilaments, for a fixed level of prestretch ($\lambda_p = 1.3$), varying number of active microfilaments ($n = 50$, 100, 150, 200, 250): (**V**) Voigt; (**M**) Maxwell; (**SLK**) Standard Linear Kelvin; (**SLK_1**) generalized Standard Linear Kelvin with spring-pot in position 1, (**SLK_2**) 2 and (**SLK_3**) 3, with $\alpha = 0.5$.

sented in the domain of the frequencies within the interval most interesting for biomedical applications, i.e. $1\,\mathrm{kHz} \leq f \leq 100\,\mathrm{MHz}$. In particular, the main attention is paid to the in-frequency system responses plotted in terms of maximum relative displacement $|\Delta U|$, in the time domain representing the magnitude of relative oscillations between environment and cell nucleus, induced by ultrasound.
Figures 2.11, 2.12 and 2.13 collect the most relevant results from the analytical models: therein, cell stiffness, prestrech intensity and number of filaments have been assumed to vary within intervals compatible with experimental findings, keeping fixed the other complementary parameters and choosing for them the most common literature values, i.e. Young modulus $E = 2100\,\mathrm{Pa}$ ([23]), cell nucleus radius $R = 1\,\mu\mathrm{m}$ ([20]) and viscosity of the water $\mu = 10^{-3}\,\mathrm{Pa}\times\mathrm{s}$ ([103]).
Figure 2.11 in particular illustrates the cell in-frequency response in terms of relative displacement, by parametrically making variable the cell stiffness from $E = 100\,\mathrm{Pa}$ to $E = 10\,\mathrm{kPa}$, coherently with data ranges reported in the experimental literature. Similarly, Figures 2.12 and 2.13 show the results for the six viscoelastic models chosen, by plotting again displacement amplitude against frequency and respectively setting the tangent Young modulus ($E = 2.6 \times 10^9 Pa$) and Poisson ratio ($\nu = 0.4$) of the microfilamts, the viscosity $\mu = 10^{-3}\,\mathrm{Pa}\times\mathrm{s}$ and making variable the prestretch λ_p and the number n of cytoskeleton filaments.
The outcomes obtained from the sensitivity analyses confirm both qualitative trends and quantitative results already found in [44], with growing peak frequencies and associated decreasing displacement amplitudes as the overall cell stiffness grows up as a consequence of the increase of the intrinsic Young moduli of the (round) cells (see Figure 2.11), as well as when the cell stiffening is induced by its adherent configuration, a situation here modeled by increasing the tensile pre-stresses in the cytoskeletal elements and the number of prestretched filaments (see Figures 2.12 and 2.13). Also, in all the analyzed single-cell systems, the results highlight that the maximum vibrations $|\Delta U|$ and associated peak frequencies always fall within the interval $10^4 \sim 10^6$ Hz, a range coherent with that experimentally established by several works (see, for instance, [80] and [66]) that still authorizes –at least in principle– to think of obtaining resonance-like responses by stimulating single cells by means of ultrasounds. Importantly, for all the viscoelastic schemes, the obtained results confirm that US-induced mechanical vibrations, $|\Delta U|$, are mostly comparable (or greater than) spontaneous thermal fluctuations if both calculated in limit situations of pure elastic media –where MSD (the Mean

Square Displacement) is $\langle u_{T,e}^2 \rangle = \dfrac{k_B T}{\pi R G}$ ([102])– and pure viscous systems, where MRD (the Mean Relaxation Distance) is $\langle u_{T,\eta} \rangle = \dfrac{2R^2 \rho_{ob} v_0}{9\mu}$ ([72]), k_B being the Botzmann constant, T the absolute temperature and v_0 the initial velocity. It can be in fact numerically verified that the MSD maximum square root is of the order of $10^{-9}m$ while MRD can oscillate between $10^{-15}m$ and $10^{-8}m$, in both the cases leading to values smaller than (or at most comparable with) the vibration amplitude peaks obtained theoretically from the above mentioned parametric analyses (see Figures 2.11, 2.12 and 2.13).

2.5 ENHANCED 3D-CIRCUS TENT MODEL FOR THE CELL INCORPORATING THE PRE-STRETCH OF THE CELL-MEMBRANE

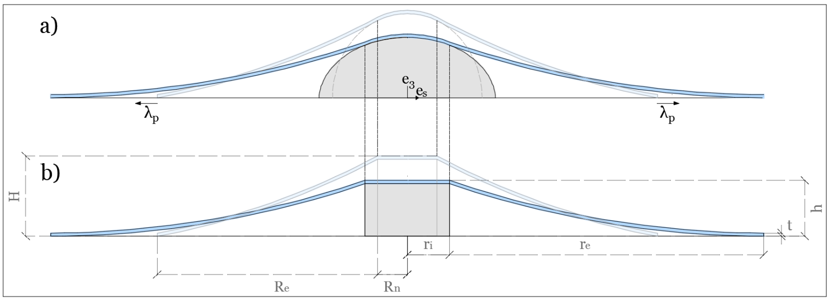

Figure 2.14: Cartoon of an adherent cell (a)), in the unkown rest and prestretched configuration, and its axysimmetric schematic idealization (b)). The nucleus, for sake of simplicity, is assumed to be a cylinder with radius r_i and height h in the prestretched configuration. The membrane is modeled as an annulus with external radius r_e and thickness t. The effect of prestretch it to compress the nucleus.

With the aim of enhancing the model presented in Section 2.4 and including the effects of the pre-stretch accumulated in the membrane coupled with the finite deformation of the nucleus on the overall *out of plane stiffness*, in this section it is presented a 3D circus tent-like model where a non linear hyper elastic analysis has been conducted starting from some recent analytic and experimental results regarding the stiffness tuning effect of Dielectric Elastomer diaphragm device followed by the application of a Electrical Field [24, 27, 88]. In fact in the work by Cugno et al. [24] it has been provided an analytical solution for the out of plane stiffness tuning effect in a elastomeric membrane due to the change induced by an external electrical field on internal stress. This solution has been the starting point to characterize the non linear mechanics of the cell membrane coupled with the deformation of the nucleus.
As previously mentioned in literature when dealing with living systems, the measures of stiffness can be significantly affected by intrinsic structural changes of the biological matter, for example by the reorganization dynamics guided by polymerization-depolymerization processes, which change the internal configuration of the cytoskeleton in this way regulating adhesion and migration cell capabilities and in turn provoking nonhomogeneous cell deformations and changes in stiffness ([3, 9, 116]), with Young's moduli also oscillating from approximately 100 Pa to 10*kPa*

([11, 22, 23, 41, 70, 81–83, 85, 100, 113, 115]). In this perspective the model here presented could be useful, during a AFM experimental stiffness mapping to perform the inverse procedure to obtain the bio-mechanical estimates.
Making reference to Figure 2.14 the cell is considered in an axis-symmetric adherent situation where the nucleus, for sake of simplicity, is assumed to be a cylinder with radius r_i and height h in the prestretched configuration. The membrane is modeled as an annuls with external radius r_e and thickness t. In the cartoon (see Figure 2.14) is highlighted the effect of prestretch which tends to compress the nucleus inducing an alteration of the internal stress. The stiffness has been evaluated by means a *small on large strategy* considering a relatively small displacement superimposed in the prestretched configuration in correspondence of the nucleus in the out of plain direction $\mathbf{e}_3$

2.5.1 *Cell-Membrane*

2.5.1.1 *Kinematics and consitutive relation*

For the membrane, in the deformed state, the current configuration Ω has been considered as $\chi = \chi_0 \circ \chi_p$ that is decomposed as follows: (i) a uniform biaxial (pre)stretch $\mathbf{x}_p = \chi_p(\mathbf{X})$, that maps the membrane from the *reference configuration* Ω_0 to the *intermediate* one Ω_p, and (ii) a *pull out* of the internal radius of the annular membrane mapped by $\mathbf{x} = \chi_0(\mathbf{x}_p)$, due to the presence of the nucleus, which transfers the body to the *current configuration* Ω (see figure to be inserted). For convenience, three different coordinate systems (COOS) and orthonormal bases are used to represent the points of the body:

1. Cylindrical COOS in Ω_0, which describes material points in the reference stress-free configuration, spanned by the triad $\{\mathbf{E_s}, \mathbf{E}_\theta, \mathbf{E_3}\}$,
2. Cylindrical COOS in Ω_p with bases $\{\mathbf{e_s}, \mathbf{e}_\theta, \mathbf{e_3}\}$
3. Curvilinear COOS in Ω with covariant bases $\{\mathbf{e_l}, \mathbf{e}_t, \mathbf{e_n}\}$ that are tangent to the coordinate lines.

Therefore, the deformation gradient of the mapping χ can be multiplicatively decomposed as $\mathbf{F} = \mathbf{F}_0\mathbf{F}_p$. Here, $\mathbf{F}_p = diag\{\lambda_p, \lambda_p, \lambda_p^{-2}\}$ is the deformation gradient due to the prestretch while $\mathbf{F}_0$ corresponds to the out-of-plane deflection. The transverse stretch λ_p^{-2} is obtained by the incompressibility constraint $\det \mathbf{F}_p = 1$ and gives the intermediate membrane thickness $t_p = T/\lambda_p^2$.

The deformation mapping $\mathbf{x} = \chi_0(\mathbf{x}_p)$, adapted from the membrane theory previously presented in [88], is assumed in the following form:

$$\chi_0(\mathbf{x}_p) = \mathbf{x}_p - x_3\mathbf{e}_3 + \mathbf{u}_0 + (x_3 + q)\,\mathbf{e}_n, \tag{2.49}$$

where $\mathbf{u_0} = \mathbf{u}_0(s,\theta)$ is the displacement of a point with coordinates (s,θ) on the midplane (for which $x_3 = 0$), $\mathbf{e}_n$ is the unit vector normal to the deformed surface and $q(s,\theta,x_3)$ is the normal component of the displacement of points away from the midplane related to the deformed configuration. By definition, the function q (and its partial derivatives w.r.t. s and θ) must vanish on the midplane:

$$q(x_3 = 0) = \left.\frac{\partial q}{\partial s}\right|_{x_3=0} = \left.\frac{1}{s}\frac{\partial q}{\partial \theta}\right|_{x_3=0} = 0. \tag{2.50}$$

The covariant bases at a point on a surface parallel to the midplane in the current configuration may be expressed as

$$\mathbf{e}_s' = \mathbf{e}_s + \frac{\partial}{\partial s}\mathbf{u}_0, \quad \mathbf{e}_\theta' = \mathbf{e}_\theta + \frac{1}{s}\frac{\partial}{\partial \theta}\mathbf{u}_0 \text{ and } \mathbf{e}_n = \frac{\mathbf{e}_s' \times \mathbf{e}_\theta'}{\|\mathbf{e}_s' \times \mathbf{e}_\theta'\|}. \tag{2.51}$$

Noting that, for the membrane in the prestretched configuration, t_p becomes small with respect to the annular width, the deformation gradient $\mathbf{F}_0$ can be assumed homogeneous along the thickness and thus approximated as follows [88]:

$$\mathbf{F}_0 \simeq (\mathbf{F}_0)_{x_3=0} = \mathbf{I} - \mathbf{e}_3 \otimes \mathbf{e}_3 + \nabla\mathbf{u}_0 + \lambda_{n3}\mathbf{e}_n \otimes \mathbf{e}_3\,, \tag{2.52}$$

where $\lambda_{n3} = (1 + \partial q/\partial x_3)$ is hence independent from x_3. Because we are interested in the response of the device to a normal displacement imposed on the internal frame, we consider the deformation as axis-symmetrical. The resulting displacement $\mathbf{u_0}$ is then a function of the sole coordinate s and no displacement occurs in the θ direction:

$$\mathbf{u_0} = u_s(s)\mathbf{e}_s + u_3(s)\mathbf{e}_3 \,\text{and}\, q = q(s). \tag{2.53}$$

Substituting the expressions for $\mathbf{F}_p$ and $\mathbf{F}_0$ into $\mathbf{F}$, it is possible to write the right Cauchy-Green deformation tensor [55] as follows:

$$\mathbf{C} = \mathbf{F^T F} = diag\left\{\lambda_p^2\left[(u_s'+1)^2 + (u_3')^2\right], \frac{\lambda_p^2\,(u_s+s)^2}{s^2}, \frac{\lambda_{n3}^2}{\lambda_p^4}\right\}, \tag{2.54}$$

where the principal stretches are simply the square roots of its elements. Applying the incompressibility constraint yields the following expression for λ_{n3}:

$$\lambda_{n3} = \frac{s}{(u_s+s)\sqrt{(u_s'+1)^2+(u_3')^2}}\,. \tag{2.55}$$

To capture the nonlinear mechanics of the membrane, we treat it as an incompressible Neo-Hookean solid. The strain energy density function (eq. (1.74) in Chapter 1) is here reported, for sake of clarity, in terms of the principal stretches [61] as follows:

$$\Psi = \frac{1}{2}\mu_m\left(\lambda_s^2+\lambda_\theta^2+\lambda_3^2-3\right), \tag{2.56}$$

where μ_m, as well known, in order to converge to the Hooke's law at small strains, represent the shear modulus of the membrane measured for infinitesimal deformations taken about a third of the Young Modulus since the incompressible behavior.

2.5.1.2 *Variational Analysis*

The total potential energy written w.r.t. the intermediate (prestretched) configuration Ω_p is expressed as:

$$\Pi = \int_{\Omega_p}(\Psi)\,d\Omega_p = \int_{r_i}^{r_e}(\Psi)2\pi s t_p\,ds =: \int_{r_i}^{r_e}\mathscr{L}\,ds\,. \tag{2.57}$$

The Lagrangian density $\mathscr{L}$ corresponds to the potential energy per unit width of each concentric ring forming the annulus. The explicit expression for $\mathscr{L}$ is obtained from Equations (2.54) to (2.56), holds as follows

$$\begin{aligned}\mathscr{L} = \frac{\pi s T \mu_m}{\lambda_p^2}\Bigg\{ &\frac{s^2\,(u_3')^2}{\lambda_p^4\,(u_s+s)^2\,[(u_s'+1)^2+u_3'^2]^2}+\\ &\frac{s^2\,[u_s'+1)^2}{\lambda_p^4\,(u_s+s)^2\,[(u_s'+1)^2+u_3'^2]^2}+\frac{\lambda_p^2\,(u_s+s)^2}{s^2}+\lambda_p^2\,(u_s'+1)^2+\lambda_p^2\,(u_3')^2-3\Bigg\}\,.\end{aligned} \tag{2.58}$$

At static equilibrium, Π must be minimized w.r.t. the functions $\{u_s, u_s', u_3'\}$, which implies the following stationary conditions (i.e. Euler-Lagrange equations):

$$\frac{\partial\mathscr{L}}{\partial u_s}-\frac{\partial}{\partial s}\frac{\partial\mathscr{L}}{\partial u_s'}=0 \quad \text{and} \quad \frac{\partial}{\partial s}\frac{\partial\mathscr{L}}{\partial u_3'}=0\,. \tag{2.59}$$

the complete expressions being found in Equation (2.70). The solutions to the governing equations in ((2.59)) must satisfy the following set of boundary conditions:

$$u_s(s)|_{s=R_i} = 0 \quad u_s(s)|_{s=R_e} = 0 \quad u_3(s)|_{s=R_i} = \bar{u} \quad u_3(s)|_{s=R_e} = 0, \tag{2.60}$$

where $\bar{u}$ is the prescribed displacement of the shuttle, due to the presence of the nucleus.

Once the solution to ((2.59)) with boundary conditions ((2.60)) is obtained, by applying the *Castigliano's theorem* (or the *Crotti's theorem* in the generalized context of nonlinear elasticity) the relationship between the shuttle displacement $\bar{u}$ and the corresponding reaction force f_m, needed to induce the displacement, can be established. In fact, the force f_m is obtained from the following derivative of the total potential energy evaluated for the extremized potential $\Pi^* = \Pi(\mathbf{u}_\mathbf{0}^*)$ at static equilibrium:

$$f_m = \frac{\partial \Pi^*}{\partial \bar{u}}. \tag{2.61}$$

It is worth noting that F depends on the following set of parameters: $\{\lambda_p$, μ_m, R_i, $R_e\}$.

2.5.1.3 *Approximate Solution*

In order to obtain a closed-form approximation that relates the force f_m with the out of plane displacement $\bar{u}$, we use a *small-on-large* strategy. This is applicable by assuming that the displacements that can be experienced from an already highly deformed configuration are relatively small w.r.t the radial dimension of the membrane, thus employing a *first order incremental* approach. The kinematics introduced in the previous section is such that a further deformation is superimposed on the highly prestretched (intermediate) configuration Ω_p through the prescription of the displacement $\bar{u}$. Therefore, under the hypothesis that $\bar{u}$ is *relatively small*, and, consequently, the current configuration is not far from the intermediate configuration, a linear approximation of the kinematics can be used to predict incremental variations of the system response.

For sake of clarity, a displacement $\tilde{\mathbf{u}}_0$ can be defined by scaling $\mathbf{u}_0$ in (2.53) by a quantity $\eta \ll 1$, namely

$$\tilde{\mathbf{u}}_0 = \eta \mathbf{u}_0 = \eta \left(u_s \mathbf{e_s} + u_3 \mathbf{e_3} \right), \tag{2.62}$$

and use this field in place of $\mathbf{u}_0$ in the sequel.

By performing a Taylor expansion of the Euler-Lagrange equations in

(2.59) and keeping only first order terms w.r.t. η, one obtains the linearization of the problem upon the intermediate configuration. Next, by substituting relation (2.62) in (2.58), Eq. (2.59) implies the following "scaled" set of Euler-Lagrangian equations:

$$u_s'' + \frac{1}{s}u_s' - \frac{1}{s^2}u_s = 0 \quad \text{and} \quad u_3'' + \frac{1}{s}u_3' = 0\,. \tag{2.63}$$

Note that, as expected in axis-symmetric problems encountered in linear elasticity, the first order approximation of the problem does not depend on the constitutive behavior of the material when the boundary conditions are completely prescribed in terms of displacement.

As shown in (2.63) the system takes the form of a set of Euler-Cauchy differential equations that, with reference to boundary conditions in (2.60), leads to the following analytic solutions:

$$u_s(s) = 0 \quad \text{and} \quad u_3(s) = \frac{\log(s) - \log(R_e)}{\log(R_i) - \log(R_e)}\bar{u}\,. \tag{2.64}$$

The force in (2.61) can be thus expressed, after some algebraic manipulations, as follows:

$$\begin{aligned} f_{ml} = -\frac{\pi T \bar{u} \mu_m}{\lambda_p^6 \log^2\left(\frac{r_i}{r_e}\right)} \Bigg\{ \log\left(\frac{\bar{u}^2 + r_e^2 \log^2\left(\frac{r_i}{r_e}\right)}{\bar{u}^2 + r_i^2 \log^2\left(\frac{r_i}{r_e}\right)} \right) + \\ \frac{\bar{u}^2\left(r_i^2 - r_e^2\right)\log^2\left(\frac{r_i}{r_e}\right)}{\left(\bar{u}^2 + r_e^2\log^2\left(\frac{r_i}{r_e}\right)\right)\left(\bar{u}^2 + r_i^2\log^2\left(\frac{r_i}{r_e}\right)\right)} + 2\lambda_p^6 \log\left(\frac{r_i}{r_e}\right) \Bigg\} \end{aligned} \tag{2.65}$$

2.5.2 *Cell-Nucleus*

The nucleus, as shown in Figure 2.14, has been modeled with an equivalent cylinder subjected to a uniform deformation with initial height H_n and transversal area A_n. In this simplification, the kinematics is completely described considering the following deformation gradient $\mathbf{F}_n = diag\{\lambda_L, \lambda_T, \lambda_T\}$ being λ_l and λ_t the longitudinal and transveral stretching.

To obtain the relationship that relates the force and the displacement in the longitudinal direction it has been considered in the framework of finite hyperelasticity, as already seen in Section 2.4, a compressible Neo-Hookean behavior (Equation (2.36)), for which prescribing an uniaxial stress state implies that $\lambda_T = \lambda_L^{-\nu}$ (see Section 2.4 for more details). Considering the hyperelastic constitutive Equation (1.55) and the definition of **P** (Equation (1.36)), the longitudinal force f_n will be the following

$$f_n = A_n P_{Lj} = A_n G_n \lambda_L \left(1 - \lambda_L^{-2(1+\nu_n)}\right) \tag{2.66}$$

2.5.3 *Coupling*

Considering the sketch of the model in Figure 2.14, at static equilibrium the reaction force f_m needed to bring the membrane in the current configuration, where in the internal frame it is prescribed a displacement $\bar{u} = h$, has to be balanced with the force f_n to induce a change in height in the nucleus ($h = \lambda_l H$, being h the eight at static equilibrium) that is $f_m - f_n = 0$. It has been shown in Equation (2.65) that f_m depends on the geometrical-constitutive parameters (μ_m, r_e), the prestretch of the membrane (λ_p) as well as the unknown internal radius of the cylinder representing the nucleus in the current configuration (r_i) and it current unknown height ($h = \lambda_L H$). The internal radius r_i is fixed by the incompressibility constraint assumed for the nucleus that is $r_i = R_0 / \sqrt{\lambda_l}$. Taking into account the Equations (2.65) and (2.66) one obtains an implicit solution of the problem at hand, namely

$$\pi \lambda_l \mu_n R_n^2 \left(1 - \lambda_l^{-2(\nu_n+1)}\right) - \frac{\pi H T \lambda_l \mu_m}{\lambda_p^6 \log^2\left(\frac{R_n}{r_e\sqrt{\lambda_l}}\right)} \left\{ 2\lambda_p^6 \log\left(\frac{R_n}{r_e\sqrt{\lambda_l}}\right) \right. \\ \left. \log\left(\frac{\lambda_l \left(r_e^2 \log^2\left(\frac{R_n}{r_e\sqrt{\lambda_l}}\right) + H^2\lambda_l^2\right)}{R_n^2 \log^2\left(\frac{R_n}{r_e\sqrt{\lambda_l}}\right) + H^2\lambda_l^3}\right) \right\} = 0 \tag{2.67}$$

In Figure 2.15 it is shown how the longitudinal stretch λ_l varies w.r.t. the prestretch λ_p of the membrane in order to respect the equilibrium. The plot has been obtained by substituting reasonable values for the geometrical-constitutive parameters of the cell ([50, 60]).

Once the solution of this equation is found with respect λ_l, it is possible to derive formally the equivalent tangent stiffness of the cell following a small on large strategy. It has been assumed that the relatively small displacement testing (for example, during a AFM stiffness mapping) is

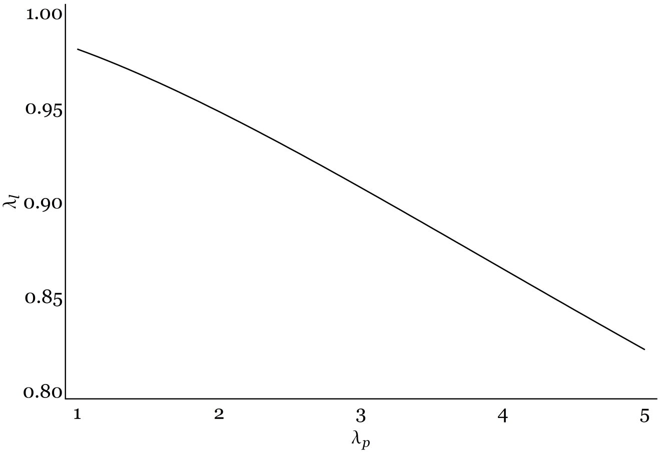

Figure 2.15: Longitudinal stretch λ_l vs prestretch λ_p that guarantee the equilibrium $f_n + f_m = 0$ with a specific choiche of the parameters: $\mu_m = 500\,Pa$, $\mu_n = 1000\,Pa, R_n = 500\,Pa, \nu_n = 0.49, H = 10\,\mu m, R_n = 1\,\mu m$, $r_e = \lambda_p \times 5\,\mu m$, $T = \lambda_p^2 \times 10\,nm$

performed in correspondence of the nucleus. In this perspective the stiffness tested will be the stiffness of the cylinder affected, however, by the current status of stretch depending, in turn, on the deformation of the membrane. The out of plane stiffness of the cell takes the form:

$$K_3 = \left.\frac{\partial f_n}{\partial v}\right|_{v=0} \tag{2.68}$$

where v is displacement (in the direction $\mathbf{e}_3$) imposed to evaluate the cell stiffness incorporating nucleus and membrane elasticity. The current longitudinal stretch $\lambda_l = \lambda_v \widehat{\lambda}$, being $\widehat{\lambda}$ the stretch solution of Equation (2.67) (coupled with the geometrical-constitutive parameters and prestretch of the membrane) and $\lambda_v = \left(1 + \frac{v}{\widehat{\lambda} H}\right)$ the superimposed stretch due to the displacement v. Thus, following Equation (2.66) the out-of-plane stiffness of the cell becomes

$$K_3 = \frac{\pi \mu_n R_n^2}{H} \left[1 - (2\nu_n + 3)\,\widehat{\lambda}_l^{\,-2(\nu_n+1)}\right] \tag{2.69}$$

Figure 2.16 shows how varies the equivalent out-of-plane stiffness of the cell with the prestretch changes. As expected, is found how the different status (adhesion, suspension, migration) of the cell characterized by different levels of polymerization-depolymerization processes, and thus different levels of the prestretch, affects the measures of cell stiffness.

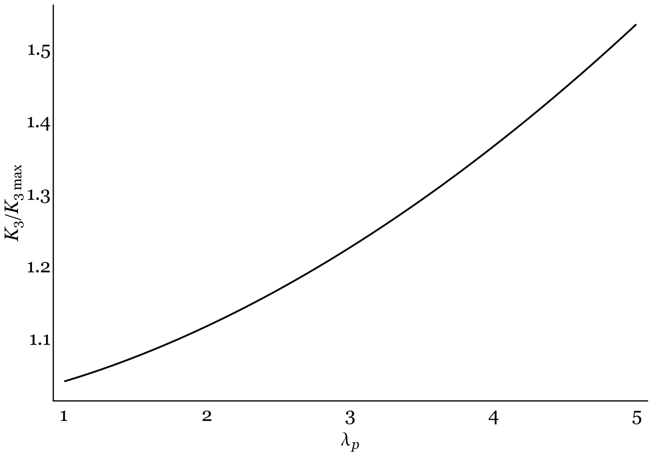

Figure 2.16: Normalized out of plane cell stiffness to the unstretched stiffness of the nucleus K_3/K_{30} vs prestretch λ_p with a specific choiche of the parameters: $\mu_m = 500\,Pa$, $\mu_n = 1000\,Pa$, $R_n = 500\,Pa$, $\nu_n = 0.49$, $H = 10\,\mu m$, $R_n = 1\,\mu m$, $r_e = \lambda_p \times 5\,\mu m$, $T = \lambda_p^2 \times 10\,nm$

APPENDIX:EULER-LAGRANGIAN EQUATION IN EXPLICIT

To minimize $\mathscr{L}$ in Equation (2.59), since is function of (u_s,u_s',u_3), the following set of Euler-Lagrangian equations have to be imposed equal to zero:

$$\begin{aligned}\frac{\partial\mathscr{L}}{\partial u_s}-\frac{\partial}{\partial s}\frac{\partial\mathscr{L}}{\partial u_s'}=\frac{2\pi T\mu_m}{\lambda_p^6}\Bigg\{&-\lambda_p^6\left(u_s'+1\right)+\frac{\lambda_p^6\left(u_s+s\right)}{s}+\frac{2s^2u_3'^2\left(u_s'+1\right)}{\left(u_s+s\right)^2\left[\left(u_s'+1\right)^2+u_3'^2\right]^3}-\\&\frac{s^2\left(u_s'+1\right)}{\left(u_s+s\right)^2\left[\left(u_s'+1\right)^2+u_3'^2\right]^2}-\frac{s^3}{\left(u_s+s\right)^3\left[\left(u_s'+1\right)^2+u_3'^2\right]}-s\lambda_p^6u_s''\\&\frac{s\left(2\left(u_s'+1\right)\left(2s\left(u_s+s\right)u_3'u_3''+\left(su_s'-u_s\right)\left(\left(u_s'+1\right)^2+u_3'^2\right)\right)\right)}{\left(u_s+s\right)^3\left(\left(u_s'+1\right)^2+u_3'^2\right)^3}+\\&\frac{s^2\left(u_s+s\right)\left(3\left(u_s'+1\right)^2-u_3'^2\right)u_s''}{\left(u_s+s\right)^3\left(\left(u_s'+1\right)^2+u_3'^2\right)^3}\Bigg\}.\end{aligned} \tag{2.70}$$

$$\begin{aligned}\frac{\partial}{\partial s}\frac{\partial\mathscr{L}}{\partial u_3'}=\frac{2\pi T\mu_m}{\lambda_p^6}\Bigg\{&\frac{3s^3\left(u_3'\right)^4u_3''}{\left(u_s+s\right)^2\left(\left(u_s'+1\right)^2+u_3'^2\right)^4}+\frac{s^2\left(u_3'\right)^3\left(s\left(2u_s'-1\right)-3u_s\right)}{\left(u_s+s\right)^3\left(\left(u_s'+1\right)^2+u_3'^2\right)^3}+\\&su_3''\left(\lambda_p^6-\frac{s^2\left(u_s'+1\right)^2}{\left(u_s+s\right)^2\left(\left(u_s'+1\right)^2+u_3'^2\right)^3}\right)+\lambda_p^6u_3'-\frac{s^3u_3'}{\left(u_s+s\right)^3\left(\left(u_s'+1\right)^2+u_3'^2\right)^3}\\&\frac{s^2u_3'\left(s\left(4s\left(u_s'+1\right)u_s''+\left(2u_s'+3\right)\left(u_s'\right)^2\right)-u_s\left(u_s'+1\right)\left(3u_s'-4su_s''+3\right)\right)}{\left(u_s+s\right)^3\left(\left(u_s'+1\right)^2+u_3'^2\right)^3}\Bigg\}\end{aligned} \tag{2.71}$$

3

MECHANICAL MODELLING OF COLLECTIVE BEHAVIOR OF CELLS

3.1 INTRODUCTION

In this chapter, preliminary results and some first models will be presented to investigate the role that mechanics plays in collective cell behaviors. Collective behavior refers to the emergence of complex migration patterns over scales larger than those of the individual elements constituting a system. It plays a pivotal role in biological systems in regulating various processes such as gastrulation, morphogenesis and tissue organization [14]. Wolgemuth et al. [78] suggested that wound healing is predominantly a mechanical process that is modified, but not produced, by cell-cell signaling. Coherent angular rotation of epithelial cells, occuring during many vital physiological processes including tissue morphogenesis and glandular formation, has been replicated by Mandar et al [122] by a cell-centered based mechanical model in which units are polarized, motile, and interact with the neighboring cells via harmonic forces. Starting from the above mentioned literature, a continuum nonlinear viscoelastic model (upper convected Maxwell model) incorporating the dynamics of liquid crystals has been studied and numerical simulations have been performed in order to reproduce recent experimental biological evidences for collective behavior of cells such as gastrulation.

3.2 CELL-CENTERED DISCRETE MODEL FOR COLLECTIVE BEHAVIOR

With reference the work by Mandar et al. [122] here is presented the discrete modeling of a coherent motion of mono-layer sheets of epithelial cells by a cell-center mechanical model. In fact Epithelial and endothelial cells that line various cavities and the vasculature in our bodies, are tightly connected to each other and exist as sheets. Upon confinement in two-dimensional geometries, these cells exhibit rotational motion, which has also been observed *in vivo* and implicated in physiological processes. However, how this rotational motion is achieved remains unclear. In Mandar et al. [122] is shown that a simple rule wherein preferred direction of motion (i.e., polarization) of cells tends to align with the direction of their velocity is sufficient to induce such coherent movement in confined geometries. It has also shown that the number of cells within the confinement, the size of the tissue, cell motility and physical properties of the cell and cell-cell connections regulate this coherent motion, and the pattern of invasion when the confinement is relaxed. A interested reader can find more details in the results and discussion in the work above mentioned ([122]).

3.2.1 *Computational model*

An epithelial sheet is comprised of a group of cells that are connected to each other via cadherin bonds to form a monolayer. Many experimental observations have demonstrated that cells in this network are persistently motile, and upon reaching a critical density show collective migration behavior [112]. Presence of front-rear polarity axis is known to be essential for migrating cells. This polarity axis manifests in migrating cells in different forms like: *(i)* increased actin activity in the front and formation of actin structures such as lamellipodia, *(ii)* localization of the microtubule organizing center (MTOC) at the front of the nucleus with microtubule growth towards the leading edge, *(iii)* gradients in cell-ECM adhesion, and *(iv)* establishment of front-rear gradients in the activity of GTPases such as Rac/Cdc42 [87]. Cell polarity is actively maintained and constantly steered by complex mechano-chemical processes governed by cell-cell and cell-ECM interactions [10, 17]. A surprisingly simple upshot of these complex processes in terms of mechanical observables is that, in epithelial sheets such as MDCK tissue, the polarization of constituent cells is closely oriented with the principal direction of stress as well as with their average velocity [26, 124]. Keeping these experimental observations in mind, it has utilized a simple model to explore how mechano-chemical properties of individual cells impact their collective behavior in confined epithelial sheets.

For modeling the collective mechanics of cells, we have adopted a ‘cell center-based mechanics model’ with cells represented as discrete points at their center of mass [89, 106, 123]. As shown in Figure 3.1, the whole epithelial tissue is represented as a continuous sheet with cell-cell cadherin junctions represented by simple harmonic springs [89, 123]. Each cell is assumed to exert an attractive or repulsive force on its neighbor-

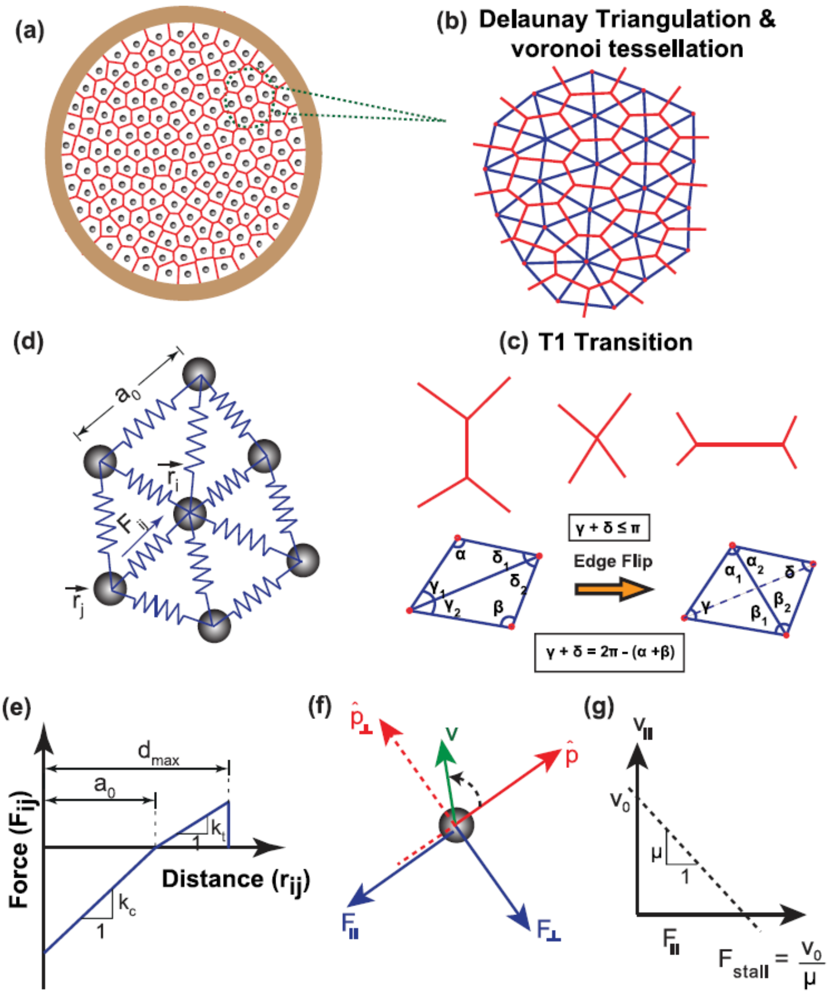
(a)
(b) Delaunay Triangulation & voronoi tessellation
(d)
a_0
$\vec{r}_i$
F_{ij}
$\vec{r}_j$
(c) T1 Transition
γ + δ ≤ π
Edge Flip
α
$δ_1$
$δ_2$
$γ_1$
$γ_2$
β
$α_1$
$α_2$
δ
γ
$β_1$
$β_2$
γ + δ = 2π - (α +β)
(e)
d_{max}
a_0
k_t
1
Force (F_{ij})
Distance (r_{ij})
k_c
1
(f)
$\hat{p}_\perp$
v
$\hat{p}$
$F_\parallel$
$F_\perp$
(g)
$v_\parallel$
v_0
μ
1
$F_\parallel$
$F_{stall} = \frac{v_0}{μ}$

Figure 3.1: A schematic of cell center model depicting the arrangement of cells and the forces acting on them. (a) A 2-D monolayer of epithelial cells, confined inside a circular geometry is considered with cells represented as points at their center. (b) Delaunay triangulation (blue) has been used to model cell—cell connectivity, which finds the nearest neighbors of each point and form the connectivity array accordingly. Because of the greater clarity it affords and better connection with the experimental geometry, Voronoi tessellation (topological dual of Delaunay triangulation) is used for visualization of cells.

(continued)

Figure 3.1: (c) When two originally connected cells move apart and form new neighbors, the connectivity of the system is updated using Delaunay triangulation. This connectivity update automatically takes T1 transitions into account. (d) Enlarged view of a representative cell i, along with its connection to neighboring cells. The position vector of this cell center is denoted by $\mathbf{r_i}$ and position vector of its j^{th} neighbor is denoted by $\mathbf{r_j}$. The blue arrow indicates the force, $\mathbf{F_{ij}}$ acting between cells i and j. The total force acting on i^{th} cell is the sum of the contributions from all the connecting neighbors. (e) The interaction between two adjacent cells is either compressive or tensile, depending upon the relative deformation of connecting spring with respect to its undeformed length, a_0. Here compressive and tensile stiffness of each spring is represented by kc and kt, respectively. While kc mimics the bulk cell stiffness, kt mimics cell-cell cohesivity. It is assumed that if the deformation of any spring is greater than d_{max}, the cell-cell connection is broken and there is no force transfer between these two cells. (f) Force acting on each cell is resolved along anti-parallel ($\mathbf{F}_{||}$) and perpendicular($\mathbf{F}_{\perp}$) to the direction of the cell's polarization($\widehat{\mathbf{p}}$). Here $\mathbf{v}$ denotes the velocity vector on each particle. (g) Velocity profile in the direction of polarization as a function of $\mathbf{F}_{||}$.

ing cells depending on the relative deformation of springs with respect to their undeformed length, a_0 and stiffness, k. The force acting on any cell at any time, t, is the sum of the contributions of all the connecting neighbors. Thus, if $\mathbf{r_i}$ represents the position of i^{th} cell, the net force exerted on that cell by neighbors (m, say) is given by

$$\mathbf{F}_i = \sum_{j \in neighbor} k(\left|\mathbf{r}_i - \mathbf{r}_j\right| - a_0)e_{ij} \tag{3.1}$$

where $e_{ij} = \frac{(\mathbf{r}_i - \mathbf{r}_j)}{\left|\mathbf{r}_i - \mathbf{r}_j\right|}$ represents the unit vector along the direction connecting the i^{th} cell with its j^{th} neighbor. Depending on the relative deformation of springs with respect to the natural length, the interaction potential can either be tensile or compressive. In order to avoid force transfer between distant neighbors, it is assumed that when the deformation of spring is greater than a threshold, d_{max}, no force transfer occurs between those two cells. Thus the value of spring stiffness for the entire range of deformation can be written as:

$$k = \begin{cases} 0, & if \left|\mathbf{r}_i - \mathbf{r}_j\right| - a_0 > d_{max} \\ kt, & if\, 0 \leq \left|\mathbf{r}_i - \mathbf{r}_j\right| - a_0 \leq d_{max} \\ kc, & if \left|\mathbf{r}_i - \mathbf{r}_j\right| - a_0 \leq 0 \end{cases} \tag{3.2}$$

In the above expression, k_c and k_t represent the bulk cell stiffness and the stiffness of cell-cell adhesions (or cohesivity), respectively. Figure 3.1(e) illustrates the attractive/repulsive force acting on each cell. The cells are allowed to exchange their neighbors, which are obtained by repeated Delaunay triangulation [84, 106]. For a given set of cell centers, Delaunay triangulation provides a connectivity for cells that produces the least number of distorted triangles, i.e., triangles with least shear strain. Delaunay triangulations are dual to Voronoi tessellations (Figure 3.1(b) and Figure 3.1(c)) and the Voronoi polygon for a given cell center can be modeled to be the cell itself (see Materials and Methods in [122]).

In this model, cells are assumed to act as self propelled active particles [123], with their inherent motility (v_0) representing the speed with which they move in the absence of any external force. The preferential direction of cell's motion (i.e., polarization) is represented by the vector $\widehat{\mathbf{p}}$, which is a coarse-grained representation of the front-rear polarization in a motile cell [87]. As cells move over a viscous substrate with mobility μ, the drag force acting in the opposite direction of motion balances the internal forces. If $\mathbf{r}_i$ is the position vector of i^{th} cell, its velocity at time t can be written as:

$$\mathbf{v}_i = \frac{d\mathbf{r}_i}{td} = v_0\widehat{\mathbf{p}} + \mu\mathbf{F}_i \tag{3.3}$$

Similar to the procedure followed elsewhere [123] and as motivated earlier, we assume that the cell's polarization vector tends to orient with its velocity vector as per the following equation:

$$\frac{d\widehat{\mathbf{p}}_i}{dt} = \xi(\widehat{\mathbf{p}}_i \times \widehat{\mathbf{v}}_i \cdot \widehat{\mathbf{e}}_z)\widehat{\mathbf{p}}_i^{\perp} \tag{3.4}$$

3.2.2 *Results*

3.2.2.1 *Coherent rotationof cells confined in circular geometry*

Various theoretical studies modeling the behavior of cells on micropatterned substrates have established the emergence of coherent rotation of cells under confined conditions [84, 123]. Similar to these studies, our model also shows the emergence of a persistent mode of rotation for a group of cells (N = 140) when confined on a circular substrate $\left(kc = kt = 10, x = 1, v0 = 1, \mu = 1\right)$ (See for instance S1 Video by Mandar et al. [122]).While the theory of active elastic systems attributes the onset of rotational motion to energy transfer to the lowest modes [42], a systematic analysis of this phenomenon in the context of epithelial sheets

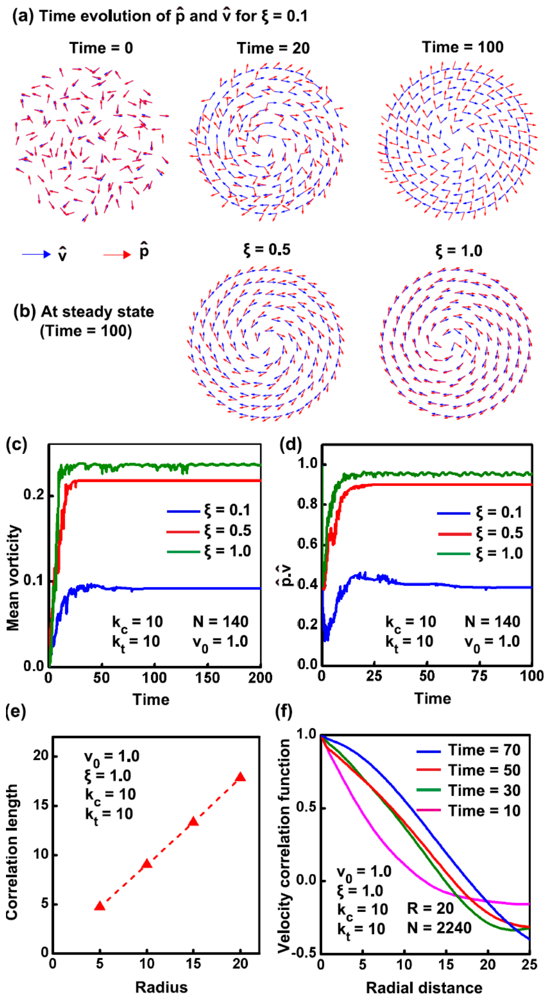

Figure 3.2: Coherent rotation of cells on circular geometry. (a) The time evolution of polarization vector, $\widehat{\mathbf{p}}$ and velocity vector $\widehat{\mathbf{v}}$ is shown for $\xi = 0.1$. The evolution rule for polarization is chosen in such a way that, from an initial random orientation, $\widehat{\mathbf{p}}$ will try to orient along velocity vector with time. (b) The coordination between $\widehat{\mathbf{p}}$ and $\widehat{\mathbf{p}}$ is decided by the parameter ξ. The higher the value of ξ, higher is the tendency of $\widehat{\mathbf{p}}$ to orient along $\widehat{\mathbf{v}}$. The orientation of $\widehat{\mathbf{p}}$ and $\widehat{\mathbf{v}}$ at steady state for $\xi = 0.5$ and $\xi = 1$ are also shown. (c) Mean vorticity for systems with different $\xi = 0.5$ is plotted as a function of time. (d) The tendency of polarization vector to orient with velocity vector is shown by the plot between $\widehat{\mathbf{p}} \cdot \widehat{\mathbf{v}}$ and time. As the value of ξ increases, value of $\widehat{\mathbf{p}} \cdot \widehat{\mathbf{v}}$ approaches 1, indicating perfect alignment between two vectors. (e) A plot of velocity correlation length for varying system size shows that correlation length equal to the confinement size. (f) A plot of correlation function with time shows that the velocity correlation length increases with time, till the coherent rotation sets in.

remains to be performed. Using our model, we demonstrate that rotation is indeed the preferred mode of motion for tissues confined in circular geometries — this mode of CAM is very different than that observed in bacterial suspensions [130] (also see S2 Text by Mandar et al.[122]). Fig. 3.2(c) illustrates the quantification of this rotational motion in terms of mean vorticity of the system (See Materials and Methods in [122]). After an initial transient mode, cells start to rotate steadily as evidenced by the constant value of the mean vorticity of the system (Figure 3.2(a)). The greater the value of ξ, higher is the tendency of polarization vector to reorganise and align along the velocity vector, resulting in faster initiation of coherent rotation of cells (Figure 3.2(b)). Fig. 3.2(d) emphasizes this by plotting the scalar product of polarization vector and velocity vector $\widehat{\mathbf{p}} \cdot \widehat{\mathbf{v}}$ as a function of time. From the figure it is seen that, as the value of ξ increases, coordination between $\widehat{\mathbf{p}}$ and $\widehat{\mathbf{v}}$ is builds up faster resulting in a faster approach to steady state of motion. We would also like to emphasize that, for larger values of ξ, the time scale for polarization evolution can be faster than the relaxation of a few long wavelength radial modes (see S2 Text and S3 Video in [122]). In this case, some long wavelength radial modes can be sustained during the coherent rotation and the tissue can exhibit radial movements that are similar to those observed by Deforet et al. [29]. Additionally, as the confinement radius R for the tissue increases, these radial movements become prominent even at lower values of ξ (S2 Text and S19 Video by [122]). This is because, larger the system size, lower is the stiffness of long wavelength radial modes, and hence slower is their decay. This behavior of increasing radial velocity for the tissue with increasing confinement size is also observed by Deforet et al. in their experiments (see SI Fig. 4 of Ref. [29]).

It was reported by Doxzen et al that, for tissues with confinement size greater than the velocity correlation length ($\approx 200m$), there was no onset of CAM within the observation window of around 48 hours [35]. However, we find from our simulations that irrespective of tissue size (R), the tissue always reaches the steady state of coherent rotation (see Figure 3.2). In other words, we find that the steady state velocity correlation length is set by the size of the confined tissue. However, the time required to reach the steady state is higher for larger tissues (see 3.2e, f). This increase in the time required to reach the steady state may be attributed to the presence of a greater number of long wavelength modes for the larger system, as described above. The presence of these modes would interfere with the transfer of cellular motility to the rotational mode.We can reconcile our simulation results with the experimental observations by noting that, as the time required for setting the coherent motion is greater for larger tissues, the tissue is likely to be perturbed by certain unknown factors (e.g., cell proliferation) in that additional time. The resulting mechanical and polarization perturbations may, therefore, further delay the onset of coherence with respect to the experimental time window, or make CAM infeasible. We predict that in the absence of perturbations, even a large confined tissue can undergo CAM. These predictions differ from the observation of finite velocity correlation lengths of around 10 cell lengths in unconfined tissues (e.g. Refs. [26, 110]), wherein different boundary conditions (e.g., leader cells, high cable tension, etc) are likely to lead to qualitatively different behavior from that of confined tissues. Collectively, these results illustrate the effect of confinement in inducing coherent angular motion. Under in vivo conditions, such confinement may be provided by non-motile cells [58] possessing higher substrate frictions than motile cells (see S4 Text and S3 and S4 Figs, S4–S11 Videos by [122]). Under these conditions, the efficiency of coherent motion is dictated by the ratio of substrate frictions between the two cell types.

3.2.2.2 *Cell crowding leads to fluidisation of tissue*

As the presence of a rotational mode of migration under confinement is well established by now, we focused our attention in understanding the characteristics of that motion in detail. Studies by Doxzen et. al. have shown that the movement of small circular tissues under confinement is similar to solid body rotations with angular velocity ω equal to $\frac{4v_0}{3R}$, where R is the radius of circle [35]. Further, the linear relationship between velocity and radial distance for rotating cell collectives obtained by multiple research groups support the argument of solid body rotations [35, 84]. However, what factors influence this solid-like tissue behavior has not been addressed. Here, we show that cell density is one such parameter dictating the nature of tissue behavior. As shown in S1 Video in [122], at lower cell densities, system behaves as an elastic solid with negligible neighbor changes and a linear velocity versus radial distance relationship (Figure 3.4(a)). Increase in number of cells in the system while keeping the size R constant, i.e., increase in cell density, leads to an interesting phenomena. Increase in cell density alters the nature of the velocity versus radial distance relationship and induces a transition from solid-like behavior ($N = 140$) to that like a fluid ($N = 170$). Specifically, with increase in cell density, the linear velocity versus radial distance

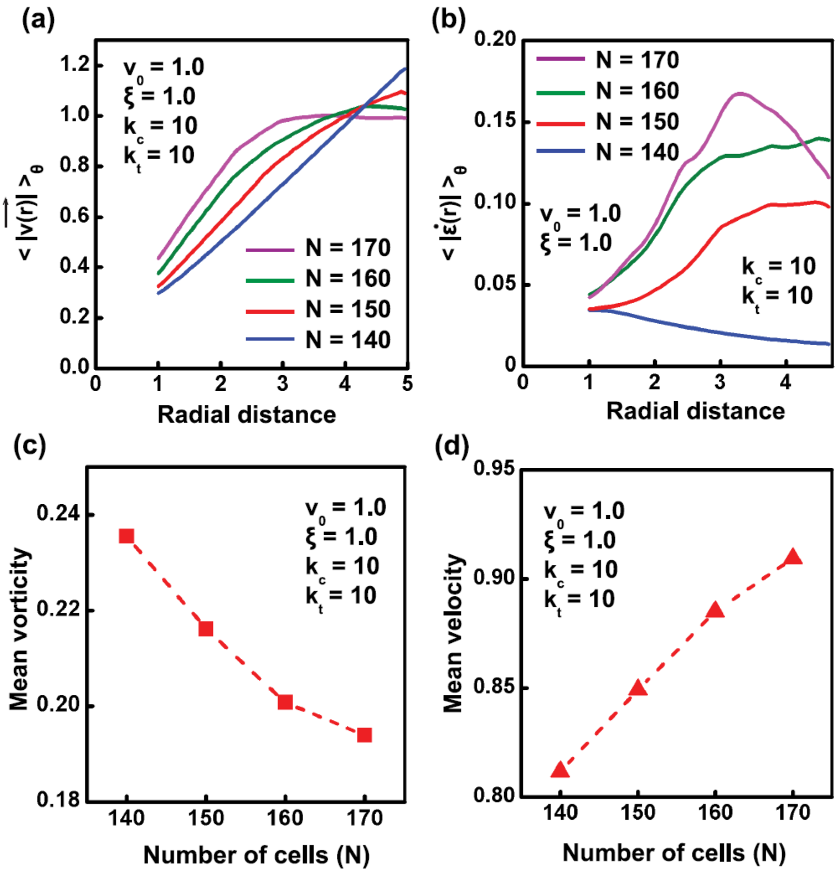

Figure 3.4: Cell crowding leads to fluidisation of tissue. (a) The relationship between velocity and radial distance is examined for varying number density. Keeping the values of other parameters same as in previous simulations, the absolute velocity, $|v|$ averaged over time, after the system reaches steady state, is plotted as a function of radial distance for varying number of cells $N = 140, 150, 160, 170$. As the number density of system increases, the velocity-radial distance curve become less linear, indicating the presence of shear in the system. (b)Variation of principal shear strain rate along the radial distance plottedas a function of number density. Increase in shear rate with number density illustrates the fluidisation of tissue induced by cell density. (c) Vorticity of system decreases with increase in cell density.(d)Without considering the effect of contact inhibition, mean velocity of the system increases with number density.

curve becomes more saturating. At the highest cell density ($N = 170$), the velocity plateaued to $v_0 = 1$ at the edges. One of the probable reasons for this change is the large shear that the system experiences at such densities, as evident from the relative sliding of cells past each other (S2 Video in [122]). Quantification of the shear strain rate ($\dot{\varepsilon}_{xy}$) from the rate of deformation tensor as $\dot{\varepsilon}_{xy} = \frac{1}{2}\left(\frac{\partial u}{\partial y} + \frac{\partial v}{\partial x}\right)$ was performed to obtain additional insight into the magnitudes of shear experienced by the cells at various cell densities. A plot showing the variation of principal shear strain rate as a function of radial distance shows that with increase in cell number, the shear in the system also increases (Figure 3.4(b)). Collectively, the above numerical results indicate that the number density of cells alters the behavior of system; i.e, at lower cell densities, system behaves like an elastic solid and at higher cell densities, system becomes more fluid-like.

While studying the effect of cell crowding on the nature of coherent rotation, we assumed that the motile cell speed or the fraction of motile cells is not modified by cell density. Consequently, we find that the mean speed of the cells in the tissue increases with cell density (Figure 3.4(d)). This finding follows from our observation in Figure 3.4(a) wherein upon increase in cell density, the tissue fluidises, as a result of which more and more layers of the tissue move with speeds comparable to $v_0 = 1$. On the other hand, when the tissue behaves elastically (for $N = 140$), the tissue rotates as a rigid body with cell speed comparable to v_0 at the edges, but

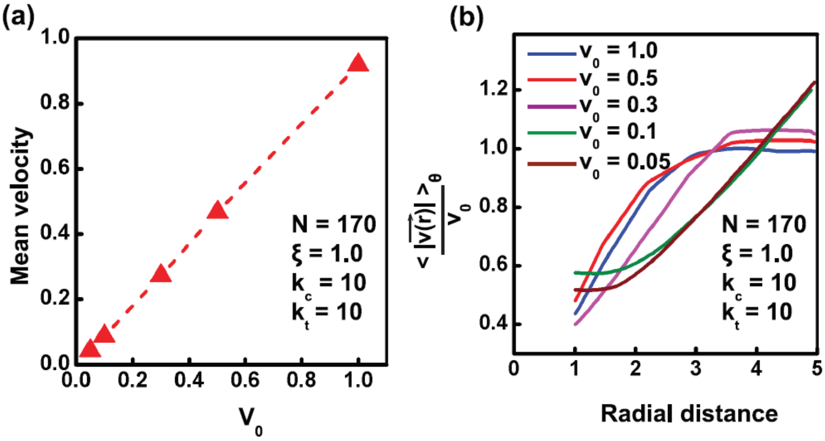

Figure 3.6: Cell motility dictates the fluidized behavior of tissue. (a)Mean velocity for varying values of cell motility (v_0).(b)Normalized velocity-radial distance

significantly lower speed of cells in the interior. However, while studying the effect of cell density on velocity profile of the over-confluent tissue, the condition of contact inhibition observed experimentally [91] has not been taken into account. To mimic the condition of contact inhibition for a denser system, and reconcile the experimental observations of decrease in mean velocity with increase in number density [35], we have considered the following cases: (i) due to crowding, the self-propelled speed of cells can be smaller on account of cells forming smaller lamellipodia [35] (see Figure 3.6(a)), or (ii) due to crowding, a fraction of cells are possibly not motile. Both of these effects are feasible due to contact inhibition of motility in crowded tissues. For both cases, as expected, we observed reduction in mean cell speeds. Additionally, we can also see from Figure 3.6(b) that the tissue shows fluidisation for value of v_0 as low as 0.3; only at really low $v_0 = 0.1$ does it recover back its elastic behavior. Thus, for appropriate values of v_0 at large N, we can observe lower mean cell speeds, concurrently with a fluid-like behavior for the overall tissue.

3.2.2.3 *Effect of tissue size, cell stiffness and cell cohesivity on tissue fluidisation*

The continuum modeling performed in [122] gives a simple expression for maximum shear strain (stress) in the tissue that is

$$\tau_{max} = \frac{v_0 \rho R}{12\mu} \quad \text{and} \quad \varepsilon_{max} = \frac{v_0 \rho R(1+\nu)}{12\mu E h} \tag{3.5}$$

being E, ν and h are, respectively, the Young's modulus, Poisson's ratio,and thickness for the sheet. This equation gives also further insights into the possible behavior of the tissue. For example, this expression predicts that a tissue with larger R has greater shear strain, and is hence more susceptible to cross over the critical strain threshold and exhibit fluidisation. To test this prediction, we performed simulations with increasing R, such that the number density of cells in the tissue was very close to the number density for the case $R = 5$, $N = 130$, where the tissue rotates as a solid. It can be seen from Figure 3.8(a) that, though there is no fluidisation for $R = 5$, for larger R, the tissue behaves in an increasing fluid-like manner—more and more layers of tissue were observed to move with velocity close to $v0 = 1$. Thus, tissue can undergo fluidisation solely due to the influence of system size. The relatively larger values of cell speeds at lower radial distance is due to radial movement of cells, and is possibly related to the dominance of radial modes with increasing system size.

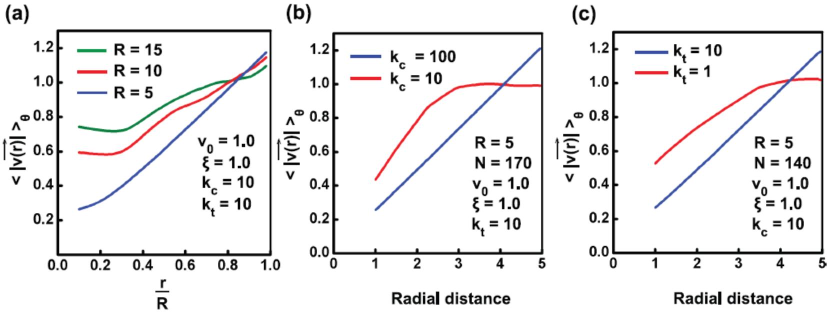

Figure 3.8: Tissue size, cell stiffness and cell cohesivity influence the fluid-like behavior of tissue. (a)The relationship between velocity and radial distance is examined for three systems with varying radius, while keeping the number density approximately same for all. The number of cells in the systems are taken as $N = 1170, 520, 130$ for $R = 15, 10, 5$, respectively. The values of other parameters are chosen as that of the previous simulations. It is observed that, while keeping the number density constant, with increase in system size, the velocity versus radial-distance profile become less linear as more number of cells tend to move with a velocity comparable to v0; this shows the presence of shear strain rate in the system.(b)Increase in cell stiffness by increasing the value of compressive stiffness (k_c) of a system will make the system stiff and resulting rotational behavior will be more like a solid.(c) Reduction in cell cohesivity (k_t) leads to fluid-like tissue behavior.

Thus, even though Equation (3.5), does not exactly capture the tissue behavior with increasing system size, it provides us with pointers in the right direction, and concurrently exposes the shortcoming of describing the tissue as a solid-like material [35].
It can be noted from Equation (3.5) that, the shear strain is, as expected, inversely proportional to the tissue stiffness. This implies that tissues with stiffer cells (k_c) and greater cell-cell cohesivity (k_t) are less susceptible to cross over the critical strain threshold and more likely to exhibit solid-like behavior; the inverse would apply for tissues with softer cells. For the case $R = 5$, $N = 170$, increasing the stiffness k_c for a tissue from 10 to 100 results in a transition from fluid-like to solid-like coherent rotation of the tissue Figure 3.8(b). Similarly decreasing the value of cell cohesivity (k_t) also leads to fluid-like behavior of tissue. We can see from Figure 3.8(c) that for $N = 140$ when $k_t = k_c = 10$, then the velocity profile being linear is an indication of rigid body rotation. However, when k_t is decreased from 10 to 1 while keeping $k_c = 10$, then it is clearly seen that the tangential velocity as a function of radial position has saturating profile indicating fluidisation. Thus the stiffness and cohesivity of tissue cells can independently control the nature of coherent rotation for the confined tissue.

3.2.2.4 *Effect of removal of confinement: Cell stiffness and cell-cell cohesivity dictates invasion pattern from coherent motion*

Under *in vivo* conditions, the confinement assumed in our simulations, is generally provided by the surrounding extracellular matrix (ECM). For example, all epithelial tissues are surrounded by the basement membrane, which helps to maintain tissue organization and prevents cell invasion. However, the basement membrane is breached by epithelial cells which turn cancerous. Cancer cells are known to invade both as single cells and collectively [25, 47, 57]. Since coherent rotation is sensitive to the properties of cell-cell contacts (i.e., k_t and k_c, respectively) (see Figure 3.8), we hypothesize that, the initial coherent rotation dictated by the properties of cell-cell adhesions has a distinct bearing on the eventual invasion pattern, when confinement is removed. To test this hypothesis, we have studied the invasion patterns formed when a coherently moving group of cells break their boundaries and invade to the surrounding matrix. For doing this, three conditions were chosen with the following combinations of k_t and k_c to mimic different properties of cells and cell-cell adhesions: $kc = kt = 1$ (i.e., soft), $kc = 10$, $kt = 1$ (i.e., medium stiff), and

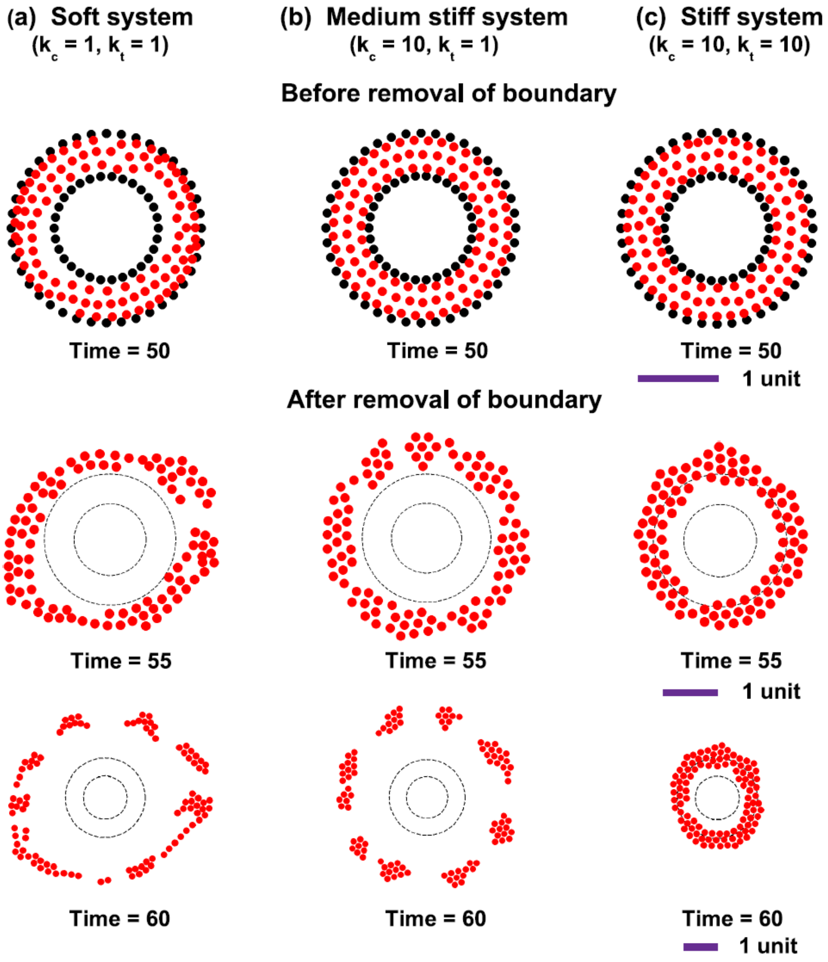
(a) Soft system
(k_c = 1, k_t = 1)
(b) Medium stiff system
(k_c = 10, k_t = 1)
(c) Stiff system
(k_c = 10, k_t = 10)
Before removal of boundary
Time = 50
Time = 50
Time = 50
1 unit
After removal of boundary
Time = 55
Time = 55
Time = 55
1 unit
Time = 60
Time = 60
Time = 60
1 unit

Figure 3.10: Cell stiffness and cohesivity dictate invasion pattern from coherent motion. Three different systems of cells are taken with different stiffness of cell-cell connections. Simulations for (a) a soft system with $k_c = 1$ and $k_t = 1$; (b) a medium stiff system with $k_c = 10$ and $k_t = 1$; (c) stiff system with $k_c = 10$ and $k_t = 10$. The number of cells in all the three cases are same and equal to 100. After reaching a steady state of rotation, confinement was removed at time, $t = 50$. The snapshots of cell migratory patterns at $t = 55$ and $t = 60$ are also shown. For the case of intermediate stiff system, cells migrate in clusters compared to softer system where cell invasion pattern is more scattered. At the highest stiffness, cells continue to rotate even after removal of boundary. The length scale for each set of figure is shown below them.

$kc = 10, kt = 10$ (i.e., stiff). The number of cells in each system was taken as 100 and the values of all other parameters were kept the same as that of other simulations.

Once coherent rotation was set up in all the systems, the confinement was relaxed at t = 50 to allow for invasion. Consistent with our hypothesis, the combination of k_c and k_t were found to directly influence the nature of coherent motion (Figure 3.10(a)-(c)). For the soft and medium stiff systems, the extent of invasion (i.e., radial position as function of time) remained the same. However, contrary to the *soft* case where cells scatter in all directions, for the *medium stiff* case, cells move radially outward as clusters which remain connected. For the *stiff* case, cells continue to rotate even after the removal of confinement. Together, these results demonstrate that the nature of coherent motion set by the extent of cell-cell cohesivity dictates the invasion pattern when confinement is removed. Also, the persistent rotation of stiff cells with stiff adhesions even after the removal of boundary shows that even though confinement is essential for the emergence of coherent rotation, depending upon the properties of the system, the presence of a confinement is not mandatory condition for the cells to continue in their coherent motion.

3.3 CONTINUUM MODEL FOR COLLECTIVE BEHAVIOR

Recently Lee and Wolgemuth [78] have hypothesized a dominant role for mechanics in wound healing, presenting a biophysical description of the collective migration of epithelial cells during wound healing based on the basic motility of single cells and cell-cell interactions. This model quantitatively captures the dynamics of wound closure and reproduces the complex cellular flows that are observed. These results suggest that wound healing is predominantly a mechanical process that is modified, but not produced, by cell-cell signaling. Here it will be presented essentially the Wolgemuth [78] model that is the starting point used to show the preliminary results of the continuum model for collective behavior. A strategy to enhance the model will be also presented in the following.

3.3.1 *Mechanical Model*

Inside a crawling eukaryotic cell, the actin cytoskeleton flows rearward at the front of the cell and forward at the rear of the cell [123]. Nascent and/or mature focal adhesions, which include integrin, link the cytoskeleton to the substrate or extracellular matrix (ECM) [4], and thereby convert the cytoskeletal flows into traction stresses that are applied to the substrate [12, 125, 130]. Like the actin velocity, the force that the cell exerts on the substrate is rearward at the front and forward at the rear; i.e., it is distributed like a dipole shows the traction stress inside a cell that is polarized along the direction $\mathbf{d}$ [12, 125, 130]. These dipole-distributed traction stresses, $\mathbf{T}_d$, lead to a net thrust force F that propels the cell at roughly constant velocity. The turnover rate of integrin inside focal adhesions is on order of a minute [32], and, therefore, integrin turnover is fast compared to the crawling speed of the cell, which allows us to treat the interaction between the cytoskeletal flows and the substrate as a resistive drag force that is proportional to the velocity, with drag coefficient ξ [69]. Epithelial cells that are in close contact can adhere to one another through cadherin molecules [74, 128]. The turnover of cadherin molecules in cell-cell adhesions is on the order of tens of minutes to an hour, which is significantly slower than the turnover rate of integrin in focal adhesions [128]. For timescales less than this turnover time τ_d,neighboring cells are effectively stuck together. A tissue of cells should therefore behave like an elastic solid on short timescales. On longer timescales, though, cadherin turnover allows the cells to slide with respect to each other, and the bulk tissue should behave more like a fluid with viscosity η. Therefore, the stress between cells is maintained on times shorter than τ_d, but dissipates on longer timescales. Cells in monolayers overlap [84] and the initial 10–12 hours of the dynamics of wound healing are not dependent on cell division [29], so we do not track the density in our model. They assume, though, that changes in density are resisted by a different effective viscosity than shear displacements and define a volumetric viscosity $(\lambda - \eta/2)$. The intercellular stress sc can then be described with the Maxwell model,

$$\mathbf{T}_c + \tau_d \frac{\partial \mathbf{T}_c}{\partial t} + \mathbf{T}_c = \frac{\eta}{2}\left(\nabla \mathbf{v} + (\nabla \mathbf{v})^T + (\nabla \cdot \mathbf{v})\mathbf{I})\right) + \lambda(\nabla \cdot \mathbf{v})\mathbf{I} \quad (3.6)$$

which is a simple model for viscoelastic fluids, being **I** the identity matrix. Their choice of this cell-cell interaction model is justified by analyzing the behavior of two solid objects connected by spring-like adhesion molecules, which is based on a model for muscle cross-bridges developed by Lacker and Peskin [75] (See supplemental Text S1B of [78] for a complete description of how this model leads to the Maxwell model). For crawling cells, the resistive drag forces are large compared to the inertial terms. Therefore, the sum of all of the forces acting on a cell must be equal to zero. In our model, we consider four types of forces that act throughout the monolayer. First is the force produced by the intercellular stress that is described above Equation (3.6). The second force is due to the internal stresses that are generated inside single cells. This stress, which we denote by $\mathbf{T}_d$, includes the viscoelastic stress of the cytoskeleton, as well as the active stresses from actin dynamics and molecular motors, such as myosin. For our model, we consider that this stress is largely dipole-distributed along the polarization direction of the cell and set it equal to its average value, that is $\mathbf{T}_d = f_0 b \mathbf{d} \otimes \mathbf{d}$, where f_0 is the dipole force and b is the dipole length. The actin flow inside a cell interacts with the substrate through adhesions and produces the thrust force **F** against the substrate. Finally, motion of the cell with respect to the substrate is resisted by drag forces, which are also due to the cell-substrate adhesions. We average the internal forces that are generated by a cell and balance these with the average external applied forces on the cell, which provides a mean-field dynamic equation governing the flow of the cells (for complete details, see Text S1A of [78]:

$$\nabla \cdot (\mathbf{T}_c + \mathbf{T}_d) + \mathbf{f} - \xi \mathbf{v} \quad (3.7)$$

where $\mathbf{f} = \mathbf{F}/A$ is the thrust force per unit area, and A is the area of a cell. In this model, we assume that the magnitude of the thrust force is a constant. The velocity $\mathbf{v}$ in Equation (3.7) defines the average local velocity of the cells in the monolayer. They consider two torques that act to determine cellular orientation. First, the polarization of the cells combined with the cell elasticity favor alignment of neighboring cells. When neighboring cells are not aligned, there is a restoring torque that acts to align them. Therefore gradients in the orientation produce an elastic torque similar to the torque on a nematic liquid crystal. For this model, we use a single Franck constant, K, to describe the magnitude of the elastic restoring torque. Second, a resistive drag torque impedes the reorientation of the cells and is proportional to the time rate of change of the orientation vector. The re-orientational dynamics are then similar to that for nematic liquid crystals [28]:

$$\xi_r \left[\frac{\partial \mathbf{d}}{\partial t} + (\nabla \mathbf{d})\mathbf{v} - \frac{1}{2}(\nabla \times \mathbf{v}) \times \mathbf{d} \right] = K \nabla^2 \mathbf{d} \tag{3.8}$$

Here ξ_r is a drag coefficient, and $\mathbf{v}$ is the velocity field for the cells. The second term on the lefthand side represents changes in orientation due to advection. The third term represents rotation of the polarization due to the motion of the cells (see Text S1C of [78] for more details).

3.3.2 *preliminary results*

The above mentioned authors have shown how the dynamics presented in the Equations (3.6) to (3.8) were able to catch analytically for 1-D simplification and numerically using the Moving Boundary Node Method [48] the wound healing border progression found in the experiments, showing possibly non-uniform progression of the wound border and transient vortices. Near the boundary the cells do not always move perpendicular to the boundary and the boundary shows characteristics of a fingering instability. However, the fingering of the border that they observe in their simulations is not as pronounced as is sometimes observed in experiments (see [78] for more details).

With the aim to reproduce the collective coherent rotation behavior in confined tissues of cells highlighted in experiments during numerous biological processes, as during gastrulation, and reprlicated with a discrete model in [122], the continuum model presented through from Equations (3.6) to (3.8) has been used considering a circular fixed domain adopting the same choice for the parameters used in the simulation [78] and reported in the table 3.12. The simulation shown in Figure 3.13 has been performed using COMSOL Multiphysics with the Weak Form

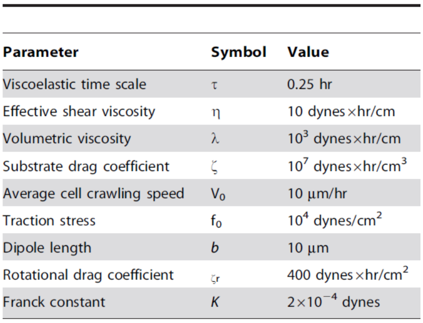

Parameter	Symbol	Value
Viscoelastic time scale	τ	0.25 hr
Effective shear viscosity	η	10 dynes×hr/cm
Volumetric viscosity	λ	10^3 dynes×hr/cm
Substrate drag coefficient	ζ	10^7 dynes×hr/cm^3
Average cell crawling speed	V_0	10 µm/hr
Traction stress	f_0	10^4 dynes/cm^2
Dipole length	b	10 µm
Rotational drag coefficient	ζ_r	400 dynes×hr/cm^2
Franck constant	K	2×10^{-4} dynes

Figure 3.12: Table of the parameters used by [78] and in the simulations. These are extimated from experiments or from simulaiton (see [78] for majior detail)

PDE tool considering a time dependent study. This preliminary solution has been carried out considering a zero stress initial condition a saddle like initial condition for the orientation of the director $\mathbf{d} = (\cos\theta, \sin\theta)$, boundary conditions $\mathbf{v}\cdot\widehat{\mathbf{n}} = 0$ and $\nabla\mathbf{d}\cdot\widehat{\mathbf{n}} = 0$, being $\widehat{\mathbf{n}}$ the normal to the boundary. Comparing this preliminary simulations with experimental observations [35] where MCDK has been plated and cultured in a disk exhibiting collective co-rotational behavior (see Figure 3.14), it is evident how is possible to reproduce this complex overall cells behavior by means of the model presented from Equations (3.6) to (3.8).

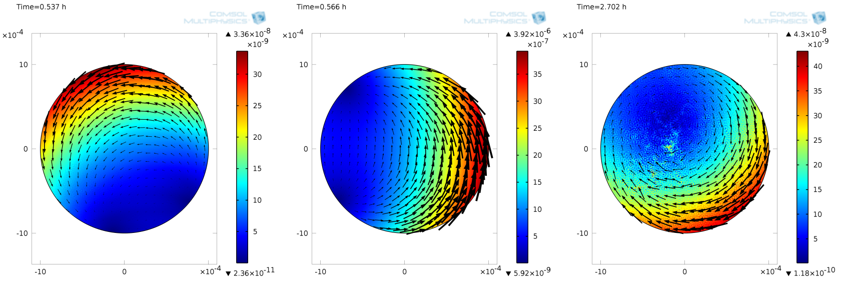

Figure 3.13: Preliminary results obtained with the parameters in Figure 3.12 in three diferent time istants.

Upper convective Maxwell viscoelastic model

A generalization of the viscoelastic model presented in Equation (3.6) could be hypothesized, considering a more *objective* time derivative in order to include the nonlinearities due to the large deformation showed

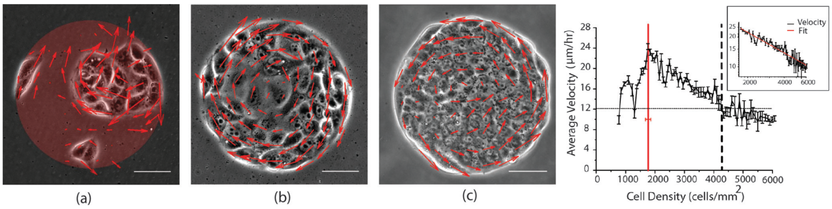
Average Velocity (µm/hr)
28
24
20
16
12
8
4
0
0
1000
2000
3000
4000
5000
6000
Cell Density (cells/mm^2)
Velocity
Fit
25
20
15
10
2000
4000
6000

(a) (b) (c)

Figure 3.14: Figure from the work by Doxzen et al. [35]. MCDK has been plated and cultured in a disk exhibiting collective co-rotational behavior.

in the experiments. In this perspective the Mawxwell viscoelastic fluid can be substituted by the *Upper Convected Mawell model* as follows

$$\begin{gathered}\mathbf{T}_c + \tau_d \left[\frac{\partial \mathbf{T}_c}{\partial t} + \mathbf{v} \cdot \nabla \mathbf{T}_c - \left((\nabla \mathbf{v})^T \cdot \mathbf{T}_c + \mathbf{T}_c \cdot (\nabla \mathbf{v}) \right) \right] = \\ \frac{\eta}{2} \left(\nabla \mathbf{v} + (\nabla \mathbf{v})^T + (\nabla \cdot \mathbf{v}) \mathbf{I}) \right) + \lambda (\nabla \cdot \mathbf{v}) \mathbf{I}\end{gathered} \tag{3.9}$$

The introduction of the nonlinearities leads a grater complexity on the computational side. For this reason the numerical simulations are still an ongoing work and the strategy to find the solution will be followed for expample by implementing Hu-washizu like variational formulation.

4

IN PROGRESS EXPERIMENTAL ACTIVITY

In Chapter 2 it has theoretically demonstrated, at least in principle, the possibility to selectively attacking cancer cell by means ultrasound, exploiting the difference in stiffness -and thus the different resonance-like frequency of tumor and healthy cells. To experimentally prove this hypothesis and with the aim to develop bio-medical device to administrate LITUS for targeting e selectively attacking cancer cells an ongoing laboratory activity is in progress in the laboratories of the Institute of the Applied Sciences and Intelligent Systems "ISASI- Eduardo Caianiello" of the National Research Council (CNR). In the following sections some preliminary results and the experimental setup are presented.

4.1 STATE OF ART

In this section the work by Geltmeier et al. [50] appeared in literature recently will be illustrated. Although the are some experimental evidences on the biological effect of the ultrasound treatment [16, 38, 62, 79, 80, 118], to date this work is the first which exploits the difference in stiffnessm between normal MCF10 and cancerous MCF7 breast cells that would provide the possibility of selectively targeting and attacking cancerous cell by means Low Intensity Ultrasound theoretically proposed in Chapter 2. In particular, Geltmeier et al. have combined in silico FEM (finite element method) analyses and in vitro assays to bolster the significance of low-frequency ultrasound for tumour treatment.

4.1.1 *FEM Validation*

From the FEM analysis simulating the AFM experiments reported in the literature (Li et al [85]), validation of the assumed cell material parameters was obtained. In this sense, the reaction force-deformation relationship for the different material parameter combinations for nucleus and cytoplasm were calculated from the FE results and compared with the reference curves determined experimentally for the lowest and highest AFM loading rates ($1 Hz$ and $0.03 Hz$, respectively) (Figure 4.1A).

Young’s modulus reference values for cytoplasm, and nucleus for the modal analysis were chosen from the best possible match of the validation simulations with the experimental curve at an AFM loading rate of $1\,Hz$. These were $0.7\,kPa$ and $7\,kPa$ for MCF10A cells and $0.47\,kPa$ and $4.7\,kPa$ for MCF7 cells, respectively. The minimum elasticity values for cytoplasm and nucleus to be used in the modal analysis were defined from fitting with the minimal experimental loading rate of $0.03\,Hz$. For both compartments, $0.25\,kPa$ were calculated for MCF10 cells and $0.15\,kPa$ for MCF7 cells.

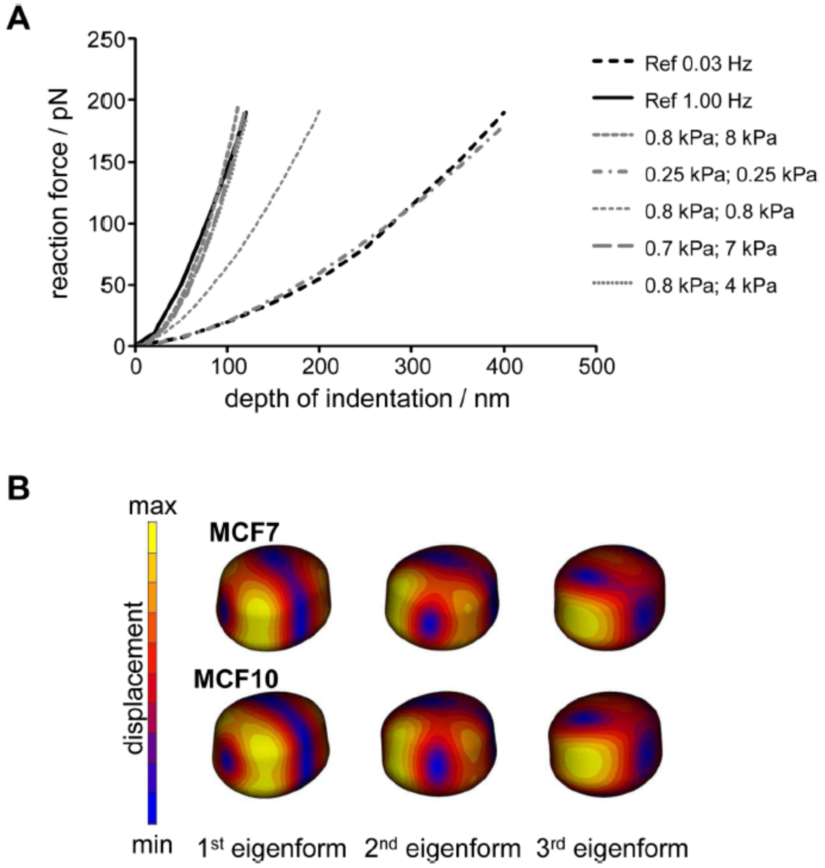

Figure 4.1: Depth of indentation for MCF10A cells in water[50](A). Calculated reaction force–deformation curves for different parameter sets for Young’s modulus of cytoplasm and nucleus (first and second value in parenthesis) for cell type MCF10A compared to reference curves from the literature (Li et al, 2008). (B) Displacements of the first three eigenforms for MCF7 and MCF10A cells in water.

4.1.2 *Modal Analysis (FEM)*

In the next step, a modal analysis was performed using reference values for the stiffness of cytoplasm and nucleus which were obtained from the above-mentioned validation studies. The modal analysis was used to characterize the eigenoscillation behaviour of the structure without external excitation. The identified mode shapes and natural frequencies provide evidence regarding what form and with which frequency the structure oscillates freely on the sole basis of its mass and stiffness as well as under defined fixation conditions. The modal analysis was used to predict the first natural frequencies and eigenforms of MCF7 and MCF10A cells for a large number of variations with respect to geometry, material and boundary conditions. An example of the shape of the deformed cells for the first three modes is shown in Figure 4.1B comparing MCF-7 and MCF10A cells. Slight differences could be observed between both cell types in the cell deformations.

With respect to the natural frequencies determined, cell dimensions, Young's modulus of cytoplasm and nucleus as well as the embedding conditions showed the greatest influence on the shift of the natural frequencies as shown in Figure 4.2. The material characteristics of the nucleus and cytoplasm showed a clear influence on the natural frequencies of both cell lines (Figure 4.2A). The material parameters were defined according to the results of the validation. The softer model with the minimum Young's modulus for cell plasma and nucleus reduced the resonance frequencies up to 50% for both cell types. The size of the cell also had a large impact on the level of the natural frequency (Figure 4.2B). Compared with the average size, the minimum cell size increased the natural frequency by up to 20%; and for the maximum cell size, the resonant frequency was reduced by up to 40%. A similar influence of cell size was also found for MCF10A cells (data not shown). The thickness of the actin cortex had only marginal effects on the natural frequencies; absence of any actin cortex caused a reduction of the resonant frequencies by 10% (Figure 4.2C). Compared to a cell in water, the natural frequencies for a cell embedded in an agar solution increased by 50% to 60% (Figure 4.2D). Reduction of the elasticity modulus of the agar solution from $50\,kPa$ to $25\,kPa$ led to a negligible reduction of these natural frequencies.

By comparing both cell lines, it could be concluded that the natural frequencies of the benign MCF10A cells were about 1.5 times higher than those of the malignant MCF7 cells due their smaller dimensions and higher stiffness.

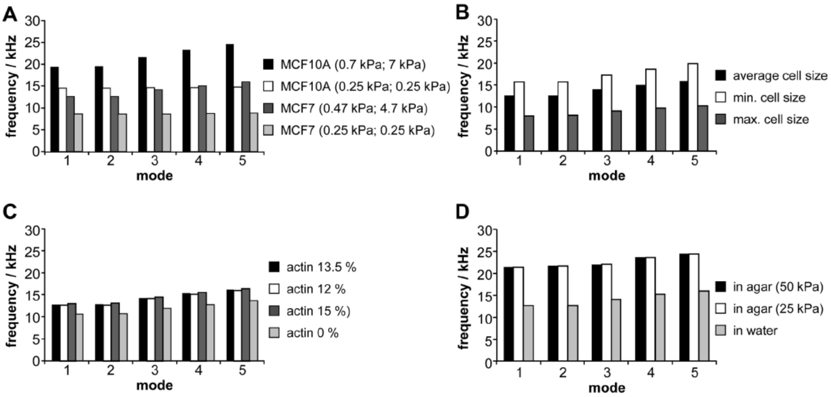

Figure 4.2: Influence of (A) material properties (Young's modulus for cytoplasm and nucleus are as first and second value in parenthesis), (B) cell dimensions, (C) thickness of the actin cortex in percent of the cell radius, and (D) cell embedding (Young's modulus for agar in parenthesis) on natural frequencies of MCF10A cells (A) or MCF7 cells (A-D).

4.1.3 *Harmonic vibration analysis*

As a result of a harmonic analysis, an amplitude frequency response can be determined that delivers resonance frequencies and the corresponding amplitudes. For the analysed cell models of minimum, mean, and maximum cell dimensions of both cell types, the range of excitation frequency was defined from the initial natural frequency up to 60 kHz. Cell type and dimension showed a great influence on the amplitude frequency response. A typical amplitude frequency response diagram is shown in Figure 4.3 for a MCF7 cells and MCF10A cells of minimum dimension. The depicted amplitude's frequency response showed significant peaks at those frequencies at which oscillation forms were excited by the ultrasonic pressure. The first peak for MCF7 cells rose at $21\,kHz$ in contrast to $34\,kHz$ for MCF10A cells. Especially this first maximum resonance amplitude of MCF7 cells amounted to more than three times the maximum cell length, indicating huge stress on cellular integrity. The first resonance frequencies of MCF7 cells of mean dimension were also significantly lower than those of MCF10A cells. In contrast, the differences between the resonance frequencies and the amplitudes were smaller for the maximum cell dimensions of both cell lines (data not shown).

Compared to being embedded in water, the resonance frequencies for cells embedded in agar were significantly higher. The significant reso-

nance amplitudes for the cell in agar solution were in the frequency range from $29\,kHz$¯$39\,kHz$ (data not shown).
The influence of ultrasonic pressure and the damping coefficient on the amplitude could be considered as being linear proportional and reverse proportional, respectively. The resonance frequencies remained constant (data not shown).

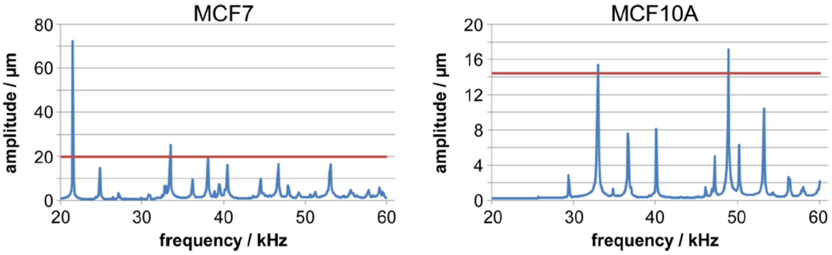

Figure 4.3: Harmonic vibration analysis of (A) MCF7 and (B) MCF10A cells (minimal sizes for both cell types) with external hydrostatic pressure in a frequency range of 20 kHz up to 60 kHz showing the displacement amplitudes. The red horizontal lines depict the maximum cell size which allows the amplitudes with the cell dimension to be compared.

4.1.4 *Ultrasonic irradiation of MCF7 and MCF10A cells*

For experimental validation of the in silico-determined resonance frequencies of MCF7 and MCF10A, specific equipment for ultrasonic irradiation was constructed. An ultrasound actuator consisting of a piezoceramic and a petri dish with a duroplastic ring in its centre as reaction vessel (——S1A Fig—-) was triggered by a function generator and an amplifier. Each ultrasound actuator was characterised for its specific frequency response in the range from $20\,kHz$ up to $60\,kHz$ over the whole reaction area of $130mm^2$. Since every glass petri dish possessed only certain specific resonance frequencies, a particular petri dish/actuator combination was used for each tested ultrasonic frequency.

4.1.5 *Selective toxicity of MCF7 cells at* $24.5\,kHz$ *under 2D and 3D culture conditions*

MCF7 cells and MCF10A cells were irradiated with different ultrasonic frequencies each with four specific intensities ($0.3\,W/cm^2$, $0.7\,W/cm^2$,

$1W/cm^2$, and $1.65W/cm^2$). Irradiation with $24.5kHz$ induced a significant increase in cell death of MCF7 cells in contrast to untreated cells (Figure 4.4A) resulting in up to 12.5% ± 2.2% dead cells with $1.65W/cm^2$ ($p = 0.007$ vs. untreated cells). No cytotoxicity could be observed for MCF10A cells at the same frequency (Figure 4.4A). Treatment with $29.4kHz$ or $43.6kHz$ resulted in a significant increase of MCF10A cells being killed ($29.4kHz$: 5.5% ± 0.8% in untreated cells to 14.7% ± 2.4% with $1W/cm^2$, $p = 0.01$; $43.6kHz$: 3.4% ± 0.8% in untreated cells to 12.4% ± 2.6% with $1W/cm^2$, $p = 0.03$) but only marginally of MCF7 cells (—S2A and S2B Fig—); no effect was seen in either cell line after irradiation with $51.2kHz$ (—S2C Fig—). In order to more accurately reflect the in vivo situation in the next setting, 3D cell growth techniques were used by culturing cells on alginate beads using the BioLevitator system. As additional cell line MDA-MB-231 (breast tumour, derived from metastatic site) was used. Treatment with $24.5kHz$ again resulted in a significant increase in cell death of both malignant cell lines (Figure 4.4B) with a maximum after use of $1W/cm^2$ (MCF7: 17.0% ± 1.6% in untreated cells to 41.4% ± 4.2% with $1W/cm^2$, $p = 0.02$; MDA-MB-231: 6.1% ± 1.8% in untreated cells to 24.3% ± 2.8% with $1W/cm^2$, $p = 0.01$). In contrast to the previous results, we also found an increase of dead MCF10A cells (12.3% ± 1.8% in untreated cells to 25.8% ± 3.9% with $1W/cm^2$, $p = 0.05$).

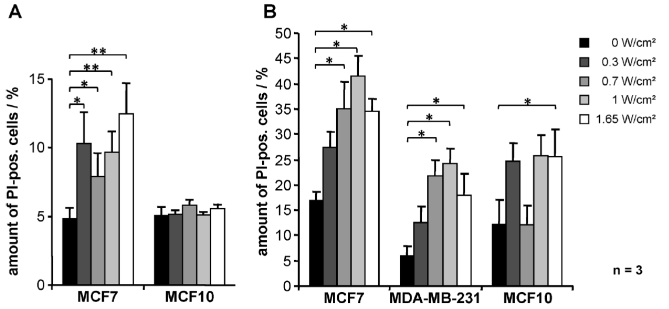

Figure 4.4: Increased death of MCF7 and MDA-MB-231 cells after irradiation with an ultrasonic frequency of $24.5kHz$. (A) Cells either cultivated in 2D culture or (B) growing in 3D culture on alginate beads (gems) were treated with $24.5kHz$ and four different intensities for $4min$; $1h$ later the proportion of dead cells (propidium iodide (PI) positive cells) was determined by FACS analysis. Results represent the means of data from eight (A) or three (B) independent experiments; the error bars represent the standard errors; p-values were calculated by the two-sided, paired Student's t-test with * p<0.05, ** p<0.01.

However, the selectivity for induction of death for MCF7 but not of MCF10A cells after treatment with $24.5\,kHz$ was corroborated by the results using real-time and label-free xCELLigence technology. Each cell type displays its own characteristic pattern which is expressed in the Cell Index (CI). Untreated MCF7 cells reached maximal impedance after 15 hours (Figure 4.5A). Whereas treatment with increasing intensities resulted in a shift of the maximum to later time-points, the cells did not reach confluence with $0.7\,W/cm^2$ during the observation period; after treatment with $1.65\,W/cm^2$, no impedance could be measured at all, indicating that an insignificant number of cells survived ultrasonic treatment. In contrast, MCF-10 cells treated with increasing intensities and also $24.5\,kHz$ were only delayed in proliferation, and maximal impedance values were measured in all samples (Figure 4.5B).

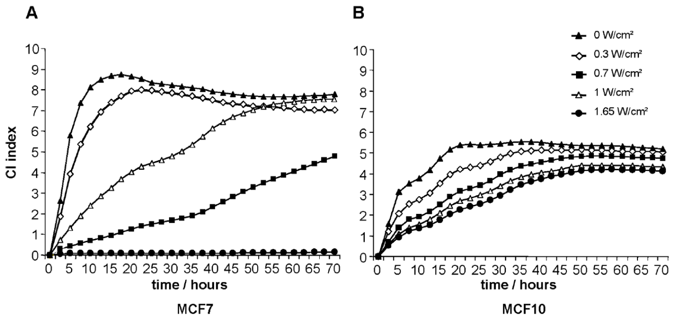

Figure 4.5: Decreased survival of MCF7 cells after irradiation with an ultrasonic frequency of $24.5\,kHz$ as determined by XCelligence (Roche).

4.1.6 *Increased cytotoxicity after fractionated ultrasonic irradiation*

Next, we examined if fractionated treatments by ultrasonic irradiation might result in enhanced cytotoxicity. Since repeated trypsinization of adherent MCF7 cells was not feasible, we used the suspension myeloid cell line HL60 for which we determined 24.9 kHz as the most effective frequency for cell killing. Cells were treated by ultrasonic irradiation up to three times at intervals of 3 h or 6 h. The number of viable cells was determined 1 h after each treatment. Even a singular treatment significantly reduced the number of viable cells to 60% (p = 0.0001) (Figure 4.6). Repeated ultrasonic irradiation resulted in a further substantial decrease of viable cells, most significant after threefold irradiation in intervals of 3 h (p = 0.02). Increasing the interval between two irradiations from 3 h to

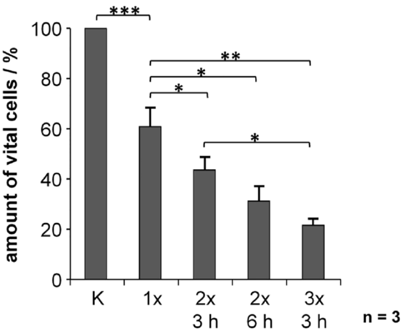

Figure 4.6: Decreased survival of HL60 cells after fractionated irradiation.HL60 suspension cells were treated by ultrasonic irradiation once, twice or three times at intervals of 3h (2x 3 h, 3x 3 h) or 6 h (2x 6 h). The number of vital cells was determined by FACS 1 h after each irradiation. (The number of vital cells of the untreated control was set as 100%.) Results represent the means of data fromthree independent experiments; the error bars represent the standard errors; p-values were calculated by the two-sided, paired Student's t-test with * p<0.05, ** p<0.01, *** p<0.001.

6 h showed a trend toward increased cytotoxicity with only 43% or 31% viable cells, respectively.

4.1.7 *Combination of ultrasonic irradiation and paclitaxel*

In another experiment, we evaluated if the effect of ultrasonic irradiation might be enhanced by a combination with chemotherapy. With this inmind,MCF7 cells were treated by ultrasonic irradiation with $23.22\,kHz$ and either $0.3\,W/cm^2$ or $1\,W/cm^2$ and subsequently cultivated for 48 hours with $100\,nM$ or $200\,nMof$ paclitaxel, one of the standard cytostatic drugs for treatment of breast cancer, (Figure 4.7) or else treated with paclitaxel followed by ultrasonic irradiation (—S3 Fig—). Monotherapy with either ultrasonic irradiation (Figure 4.7A) or paclitaxel (Figure 4.7B) resulted in a significant reduction of the numbers of vital cells to 63.9% ± 4.6% or 66.5% ± 2.8%, respectively ($p = 0.0002$ for $1\,W/cm^2$ vs. unirradiated control; $p < 0.0001$ for $200\,nM$ vs. unirradiated control). A further significant decrease with only 47.9% ± 4.5% of vital cells was achieved after combining ultrasonic irradiation with $1\,W/cm^2$ and $200\,nM$ paclitaxel ($p = 0.0007$ for combination vs. ultrasonic monotherapy; $p = 0.002$ for combination vs. $200\,nM$ paclitaxel monotherapy) (Figure 4.7C). The results of the combination treatment in the opposite order (paclitaxel followed by ultrasonic irradiation) showed similar effects (—-S3 Fig—-). We again found a significant enhancement of the effects (reduction of proportion of surviving cells) of both monotherapies (67.1% ± 4.8% after irradiation with $1\,W/cm^2$ or 69.8% ± 6.8% treatment with $200\,nM$ paclitaxel) in their combination to only 47.9% ± 5.5% (p = 0.0003 combination vs. ultrasonic monotherapy with $1\,W/cm^2$; $p = 0.0008$ combination vs. $200\,nM$ paclitaxel monotherapy) (—S3A–S3C Fig—).

For both regimens, the comparison between monotherapy with 200 nM pactlitaxel and combination therapy with only $100\,nM$ and ultrasonic treatment revealed a significant decrease in vital cells in the combination treatment ($p = 0.02$ for ultrasonic treatment ($23.22\,kHz$, $1\,W/cm^2$) + $100\,nM$ paclitaxel; $p < 0.0001$ for $100\,nM$ paclitaxel + ultrasonic treatment ($23.22\,kHz$, $0.3\,W/cm^2$); $p = 0.01$ for $100\,nM$ paclitaxel + ultrasonic treatment ($23.22\,kHz$, $1\,W/cm^2$); all vs. $200\,nM$ paclitaxel).

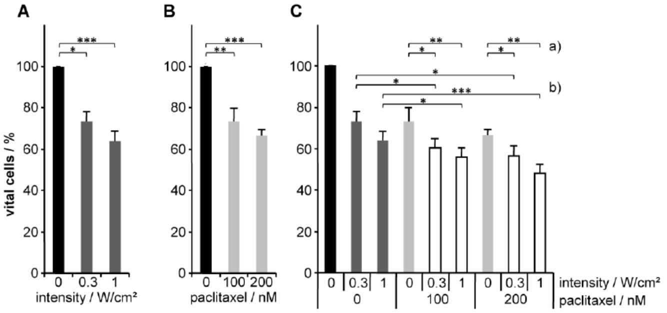

Figure 4.7: Treatment of MCF7 cells with either (A) ultrasonic irradiation with 23.22 kHz and two different intensities ($0.3\,\mathbf{W/cm^2}$ or $1\,\mathbf{W/cm^2}$, dark grey bars), (B) paclitaxel with 100 nM or 200 nM (light grey bars) or (C) combinations of both treatments (ultrasonic irradiation followed by paclitaxel treatment; white bars) with a) constant concentration of paclitaxel and different intensities of ultrasonic irradiation, and b) constant intensity and different concentrations of paclitaxel. Results represent the means of data from eight independent experiments; the error bars represent the standard errors; p-values were calculated by the two-sided, paired Student's t- test with * p<0.05, ** p<0.01, *** p<0.001.

4.2 PREPARATION OF THE EXPERIMENTAL SETUP (AT THE ISASI)

In the laboratory of the Institute of the Applied Sciences and Intelligent Systems "ISASI- Eduardo Caianiello" of the National Research Council (CNR) an ongoing work is focused for preparing an experimental setup with the aim to exploit the difference in resonance-like frequency due to the difference stiffness of cancer and healthy as shown in Section 2.3 and in the above mentioned studies. The work represents a preliminary validation status and in the following it will be presented the experimental setup used.

In particular in in this phase it has been investigated the integration of digital holography (DH) imaging and acoustic manipulation of microparticles in a 3D microfluidic environment. The ability of DH to precisely quantify and track the position of a floating sphere inside a microfluidic channel is used to measure the motion of an object trapped by a stationary pressure field generated through ultrasonic waves. The obtained displacement is compared with the numerically computed positions of the nodes of the standing wave, providing a direct verification of the theoretical expectations. Moreover, DH allows following the aggregation dynamics of trapped spheres in the planar direction. All together, the integration of DH and acoustophoresis is suggested as a powerful approach for precise design and implementation of accurate manipulation in advanced lab-on-chip microfluidic devices.

4.2.0.1 *Introduction*

Manipulation of particles in microchannels using ultrasound waves, commonly known as acoustophoresis, has attracted increasing attention in the past decade. Several applications have already been proposed in which acoustic radiation forces generated by ultrasonic waves were used to trap and manipulate objects in 3D. In fact, depending on the adopted geometry, the radiation forces can be exploited to different ends. They have been successfully employed to trap cells and particles, retaining them against a flow and promoting clusters formation [39], to move them to arbitrary positions in a controlled manner [19], to levitate or push them toward a surface [51, 121]. Moreover, acoustic forces demonstrated to be able to sort particles based on their size and density in a continuous flow setup [121].

In general, acoustophoresis proved to be a very effective tool to be incorporated in microfluidic-based lab-on-chip devices but, in order to optimize the design and implementation, a very precise calibration of the obtained pressure field is required [76].

This issue is even more pressing when dealing with soft samples, such as biological ones, which can be deformed by the application of ultrasonic pressures [64, 98].

In this case, a detailed calibration of the system is of paramount importance and, in turn, it could provide an alternative contact-less approach to apply and measure forces to single cells and biological specimens, with respect to standard nanotechnology-based actuators [2].

Several strategies have already been proposed, but an ultimate approach for acoustic forces calibration has not yet been assessed. Here the integration of Digital Holography (DH) with acoustic manipulation within a transparent microfluidic channel is proposed to precisely measure the 3D motion induced by the acoustic pressure field. This result provides a first step towards precise and direct calibration of the ultrasonic pressure field for quantitative biological applications. Moreover, the ability to control the particles' position in the microchannel is fundamental to validate the manipulation effectiveness.

Standard tracking techniques are based on quantitative analysis of video microscopy images [21] and are commonly employed for motion parallel to the microscope's focal plane. On the other side, multi-particle axial tracking is based on the interpretation of diffraction rings and can be obtained only after extensive calibration [13] or at the expenses of reduced spatial-temporal resolution or z-range [126].

Those limitations can be surmounted employing digital holography (DH) in microscopy. This powerful, label-free imaging technique furnishes quantitative phase-contrast maps (QPMs), while simultaneously allowing investigating dynamic processes [71] and tracking cells/particles migration in the sample volume [96]. In particular, it can be utilized to follow the displacements of all the multiple objects observable inside the field-of-view (FOV): the axial displacement are usually evaluated by refocusing criteria [96], while the lateral shifts can be computed by applying conventional video-tracking methods to the retrieved QPMs [93, 94, 96].

In this work, we employ DH fro assessing the 3D dynamic displacement and position of polystyrene microspheres subjected to ultrasonic standing waves. In particular, we make use a refocusing criteria, based on Tamura coefficient [92, 95], to monitor displacements along the optical axis ascribable to the action of PRF and SRF. Moreover, we study the degree of particles aggregation around nodes by a 2D image segmentation method.

4.2.1 *Experiments*

We employed 5 µm-radius polystyrene spheres dispersed in water, generating inside a microchannel different ultrasound standing waves. The study is articulated in two steps. In the first part, we demonstrate the ability of DH to track particle in 3D by monitoring height variations. We apply sequences of different standing waves, each with nodal planes at specific heights. For polystyrene microspheres in water, the PRF is dominated by the gradient of the squared acoustic pressure, driving the microspheres toward an acoustic pressure node (Eq.1). When different resonant frequencies are applied in a sequence, the microspheres move from one node to another. In this way, it is possible to modify the particles' height in a controlled manner. In the second part, we study the aggregation dynamics on particles ensembles, where a single ultrasound standing wave is applied and the particles' aggregation rate is monitored. We employ a Mach-Zehnder-based digital holographic microscopy setup, working in transmission mode (Figure 4.8a).

The emitted light of a laser (Coherent Inc., Sapphire SF, λ=488 nm) is divided into an object illumination wave (O) and a reference wave (R) by a 50:50 beam splitter (BS1). The former impinges orthogonally on the sample holder, described in details in the following section, and it is coupled into a microscope lens (MO) to enhance the lateral resolution. The reference wave is guided directly by a second beam splitter (BS2) to the image-recording device. On its path, a second MO is placed to compensate for the formation of circular aberration in the recorded image. Holographic off-axis geometry is achieved by a phase gradient of the reference wave front relative to the object wave front, which is obtained by a slight tilt of the beam splitter BS2. The optical path length difference has been adjusted in order to assure the formation of the interference pattern.

The interferogram formed by the superposition of the two waves is registered by a CMOS digital camera (IDS, UI-3370-CP) and transferred to an image processing system for the reconstruction and the evaluation of the digitized holograms. Regarding the sample holder, to generate the ultrasounds standing waves we employ the AFS module from LUMICKS. Its main element is a chip (see Figure 4.8b), consisting of two glass layers with a fluid channel inbetween and a piezo element on top. The chip is inserted in a custom-made holder that enables sample injection in the microchannel through a microfluidic system. As shown in Figure 4.8, the piezo-device is driven by a function generator (Tektronix, AFG3051C). In particular, we have employed sinusoidal signals with frequencies in the range of 7-15 MHz and peak-to-peak voltage up to a maximum of 7Vpp.

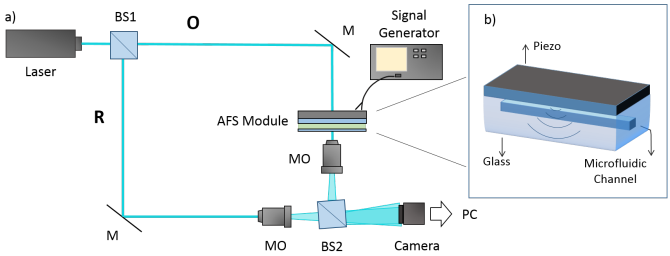

Figure 4.8: a) Mach-Zehnder setup for digital holographic microscopy in transmission mode. Laser: laser light source (λ=488nm); O: object wave; R: reference wave; BS1, BS2: non-polarizing beam splitter cubes; M: mirror; AFS Module: sample holder and ultrasound generator; MO: microscope lens; Camera: hologram recording device (CMOS image sensor); PC: computer. b) Detailed structure of the flow cell, consisting of two glass plates with a fluid chamber in between. For the ultrasound generation, a piezo plate is attached to the upper glass slide and connected to a signal generator.

4.2.1.1 *Data Analysis*

The polystyrene microspheres (PS) carboxylate-modified 4% solids, diameter 5.1 µm were purchased from Thermo Scientific. Their density at 20°C is of 1.055 g / cm3 and they have been dispersed in water and sonicated before being used. The information of the particles and medium composition have been used to calculate resonance frequencies and force profiles of the flow chamber by a one-dimensional model furnished by Lumicks [68].

We have concentrated our attention on two specific resonance frequencies, at 14.11MHz and 7.04MHz, based on their nodes position. In Figure 4.9 are reported the axial components of the radiation forces exerted by the two fields, calculated from the model employing the following definition:

$$F = -V\nabla\left[\frac{1-\kappa*}{4}\kappa_m p^2 - \frac{3}{4}\left(\frac{\rho*-1}{2\rho*+1}\right)\rho_m v^2\right] \tag{4.1}$$

where V is the microsphere volume, p is the acoustic pressure, v the acoustic velocity and $r*(=rp/rm)$ and $k*(=kp/km)$ are the density ratio and compressibility ratio between the particle and the medium, respectively [120].

The reported values are calculated using in both cases a driving signal with amplitude $V = 7Vpp$. However, the forces' intensities depend on the square value of the driving field amplitude, so they can be easily tuned to suit ones needs [68].

This force, called primary acoustic radiation force (PRF), acts in the direction of the ultrasound wave's propagation. Upon its action, the particles are pushed towards either the pressure nodes or antinodes, depending on their characteristics and that of the medium. In our case - polystyrene microspheres dispersed in water - the PRF is dominated by the gradient of the squared acoustic pressure, driving the microspheres toward an acoustic pressure node. Moreover, once the particles have reached their equilibrium plane, they start to form two dimensional aggregates due to the lateral component of the PRF. This process is also influenced by the existence of secondary radiation forces (SRF), caused by the sound field's scattering from the particles [39, 52]. We experimentally test theoretical results reported in Figure 4.9. We recorded videos of the changes in the spheres position upon application of sequences of different ultrasound standing waves. In the setup, a 20X microscope ob-

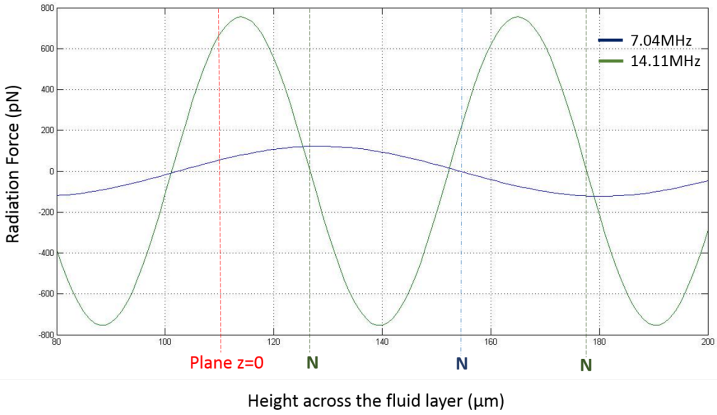

Figure 4.9: Primary radiation forces simulated profile inside the microchannel. The forces are generated by a driving signal with frequencies of $14.11\,MHz$ (green) and $7.04\,MHz$ (blu), and amplitude $V = 7Vpp$. The corresponding nodal planes (N) and the initial plane are highlighted.

jective is mounted in order to enhance the DH resolution capabilities along the z-axis [14]. Moreover, from the camera settings the region-of-interest (ROI) is restricted around a single microbead to increase the acquisition rate to 20 fps. A sequence of two frequencies, 7.04MHz and then 14.11MHz, has been applied. The piezo is driven with a peak-to-peak voltage of 5V. The signal amplitude has been chosen to minimize the impact of the lateral component of the PRF. In fact, the latter tends to move the particles in the x-y plane. We have observed that for higher driving voltage amplitudes, the resulting lateral component of the radiation force is intense enough to drive the microsphere outside the ROI during the video recording.

Initially the sample holder position is adjusted so that the sphere is in the focal plane. Following the application of the resonance frequencies' sequence, the microsphere moves towards available nodes, changing its axial position. Nevertheless, for each video frame, which is a holographic image of the sample, it is possible to apply a refocusing criterion method to track the position of the microsphere along the optical axis. We use the Tamura coefficient Td [92, 95] defined as:

$$T_d = \sqrt{\frac{\sigma\left(A_d\right)}{\mu\left(A_d\right)}} \tag{4.2}$$

where A_d is the amplitude reconstruction of the digital hologram calculated at distance d, $\sigma(\cdot)$ and $\mu(\cdot)$ are the standard deviation and average value operators, respectively. The refocusing criterion is obtained by solving the following optimization problem

$$d_{foc} = argmax\{T_d\} \tag{4.3}$$

where d_{foc} is the calculated microsphere position along the optical axis. We apply the Tamura criterion to the holographic recorded sequence of a single microsphere under the cascade of resonance frequencies 7.04MHz and then 14.11MHz. The resulting particle movement along the optical axis is depicted in Figure 4.10. The microsphere is initially suspended at about 100µm from the channel's bottom. This position is taken as the reference height, i.e. the axial position is assumed as 0 in Figure 4.10(a). When the first standing wave is generated at the time t1, the resulting primary acoustic radiation force traps the particle at the nearest nodal plane (at about 46 µm from the initial position).

Subsequently, the 14.11MHz resonance frequency is applied and the microsphere moves towards the nearest nodal plane, placed at z=75 µm.

Notice that in the first case the microbead needs about 7s from the instant in which the field is applied to reach the nodal plane. In the second case, the result is reached in less than a second. The difference is due not only to the different travelling distances, but also to the difference in the PRF's intensity in the two cases (see Figure 4.8).

On the other hand, to check the process of particle's aggregation, a single ultrasound standing wave is applied while the particles positions are monitored via DH. We have chosen to drive the piezo-device with the frequency of 14.11MHz, which results in the highest force intensities and thus has the strongest effect on the particles. The driving voltage has a 7Vpp amplitude.

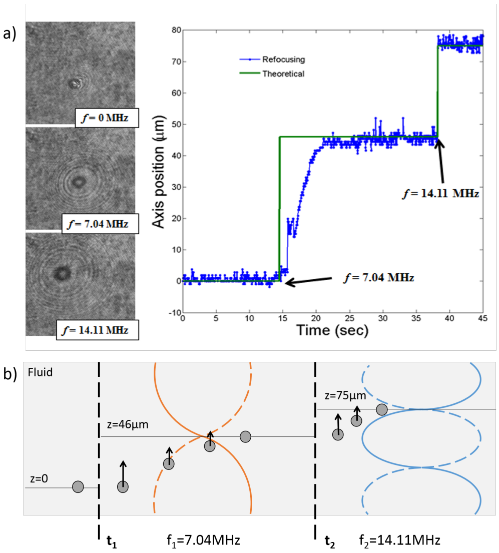

Figure 4.10: a) Changes in the particle's axial position upon application of two resonant frequencies, 7.04MHz and 14.11MHz, as reconstructed from the numerical refocusing of the holographic video. The three images in the left are the recorded holograms where the axial movement is clearly detectable b) Schematic depiction of the changes in the microspheres height.

In the setup a 10X MO is mounted, providing a FOV of about 650x650 μm2 and guaranteeing that a significant number of particles are imaged. Following the application of resonance frequency, the microspheres immediately move towards the first available node, then they start to form two-dimensional aggregates in the nodal plane. The whole process is recorded with an acquisition rate of 14 fps. Each video frame is a holographic image of the sample from which it is possible to obtain amplitude

or quantitative phase-contrast maps. In our case, the amplitude maps are extracted, as the microbeads are made of absorbing material. In case of transparent samples such as cells, QPM can be instead employed, fully exploiting the potentiality of DH.
We analyse the particles aggregation rate by measuring the number of clusters of microspheres in time and the number of microspheres per cluster in time. An image segmentation method based on thresholds is adopted for detecting separated regions of interest (ROIs). Each ROI contains a certain number of microspheres, thus an isolated microsphere is the simplest ROI. Therefore, we define the number of clusters as the number of ROIs, while the number of microspheres per cluster is defined as the area of the corresponding ROI divide by the ideal area of one microsphere. In Figure 4.11 is illustrated the results of the ROI extract method

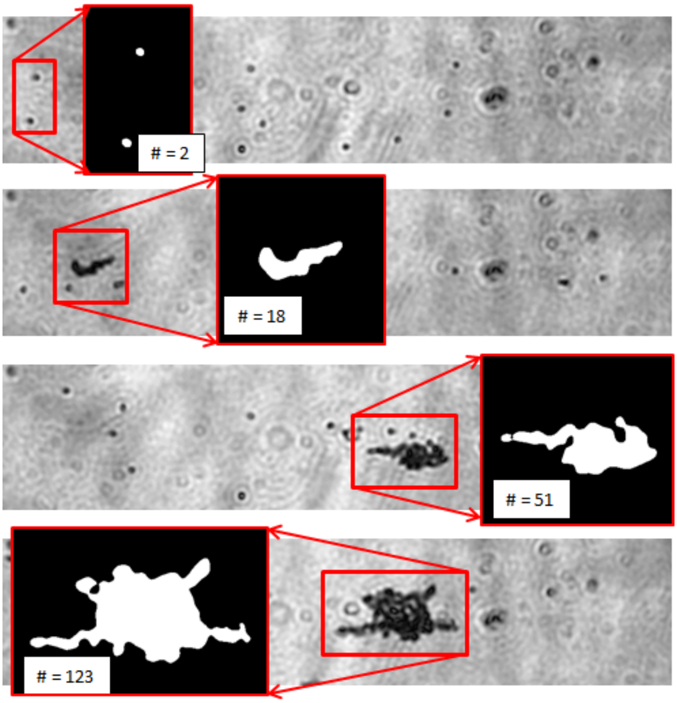

Figure 4.11: Four amplitude reconstructions of the holographic sequence. The red boxes highlight the results of the ROI extraction method where the estimated number of microspheres for the detected cluster is calculated.

applied to 4 amplitude reconstructions, while in Figure 4.12 the two plots of number of clusters/time and number of microspheres per cluster/time.

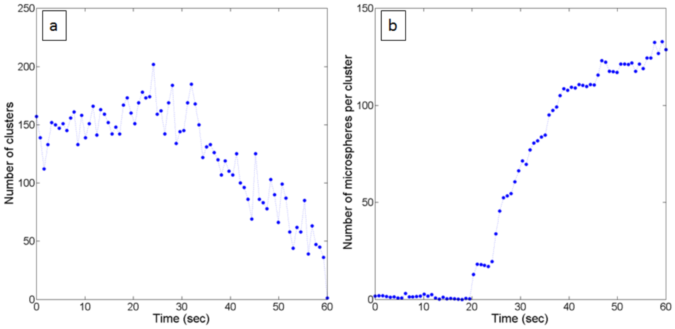

Figure 4.12: Estimation of (a) the number of clusters of microspheres in time and (b) the number of microspheres per cluster in time.

5

CONCLUSION & FUTURE PERSPECTIVE

Cancer is a genetic disorder that involves the transformation of benign body cells into malignant rapidly dividing cells through abnormal changes called hyperplasia and dysplasia. In hyperplasia, there is an increase of the number of cells that generally leaves organs or tissues normal when observed under a microscope; in dysplasia, the process is still accompanied by an altered proliferation program, but the cells look generally abnormal. However, rigorously speaking, hyperplasia and dysplasia may or may not become cancer, even if they represent propaedeutic steps toward cancer diseases.

Tumors are constituted by a complex mix of neoplastic (cancer) and normal (healthy) cells. At this scale, regardless the cell line, there are very few common factors in solid tumors: two of these are the overall abnormal growth of the tissues and the anomalous regression in cell differentiation, prodromal to cell spread and metastasis. To distinguish between anomalous malignant and benign cell growth is however often impossible in small tissues.

To date, in absence of alternative ways for recognizing and targeting cancer cells, molecular markers are widely employed to detect tumors. As a matter of fact, not-specialized, back-differentiated and generally potentially metastatic cells are in the vast majority of the cases excluded by this type of targeting, because molecular markers require to deal with highly specialized cells, normally less aggressive than the not-specialized counterparts. However, regression toward less specialized cell types nearly often camouflages cancer cells in normal less differentiated cells, a fact that generally forces to change markers.

After a preliminary introduction in Chapter 1 of the fundamentals of nonlinear mechanics and classical and fractional viscoelasticity, in Chapter 2 by exploiting some consolidated literature results that have demonstrated that tumor cells are significantly softer than the healthy ones, independently from the cell line and regardless of the measurement techniques utilized for determining the cell stiffness, the frequency response of single-cell systems has been investigated by using both consolidated and generalized spring-pot based viscoelastic schemes. After conducting a sensitivity analysis with respect to cells physical and geometrical parameters, the theoretical models have been finally specialized to cancer and healthy cells, whose mechanical properties were *ex vivo* or *in vitro* experimentally measured.

The results have shown that a mechanical-based way for targeting cancer and healthy cells may be actually envisaged. To this purpose, the theoretical outcomes have in fact highlighted that, for all the cell lines examined and independently from the viscoelastic scheme adopted to simulate the cells response, normal and tumor cells peak frequencies can be clearly distinguished. Importantly, they mosty fall within the range $(10^4, 10^6)$ Hz, an interval compatible with LITUS (Low Intensity Therapeutic UltraSound) already widely employed for medical applications. Peak frequency values outside this interval are found for the sole cases associated to extreme limit situations, that is both when the cells behave as fluid-like (Maxwell) viscoelastic materials and exhibit highest elastic modulus and/or large nucleus sizes (in this case the peak frequency tends to disappear) and when the cells behave as Voigt viscoelastic systems and contemporaneously are characterized by lowest stiffness or highest viscosity (in this case the peak frequencies move toward frequencies slightly lower than 10^4 Hz). It is worth to notice that both these theoretical limit situations are quite unrealistic, because they assume that essentially the cells would behave as a viscous fluid, in the first case the Maxwell model intrinsically representing a fluid-like material and in the second case the Voigt with high viscosity and low stiffness still representing a fluid-like behavior.

Although the outcomes are to date only theoretically derived, it is felt that - if the predictions were experimentally confirmed - the present study might open the way for envisaging alternative strategies for diagnosis and therapy of cancer diseases, both designing pioneering generations of mechanically-based tumor markers and *ad hoc* taking advantages from the resonance-like phenomena to selectively attack malignant cells. In this perspective an experimental activity is in act in the the laboratory of the Institute of the Applied Sciences and Intelligent Systems "ISASI- Eduardo Caianiello" of the National Research Council (CNR) (illustrated in Chapter 4). The activities have been to date limited to asses the experimental procedure and calibrate the setup. Subsequently analyzing cancer and healthy cell lines, ultrasounds will be applied at selected frequencies to prove the theoretical principle described in Chapter 2.

Furthermore, with the aim to enrich the modeling of single-cell systems, in Chapter 2 has also been considered the effect of the prestress (for instance, induced in protein filaments during cell adhesion) on the over-

all cell stiffness, finally determining its influence on the in-frequency response of the cell. To this end, a simple multiscale scheme that incorporates finite elasticity has been first proposed to include, by using a bottom-up homogenization procedure, suitable prestress-modified stiffness values into the viscoelastic single-cell models.
Successively, an enhanced 3-D *circus tent-like* model, which includes finite elasticity and involves prestretched filaments in the membrane as well as the deformation of the nucleus, has been introduced to better capture the actual effects of the cell configuration states on the overall *out of plane stiffness*. it has been constructed an analytical approach to find a solution of memebrane-nucleus coupled problem. The model proposed could be helpfully utilized in AFM experimental measurements when determining stiffness maps for example to give formulas for obtaining how actual prestress level in the cell membrane influence the overall cell elasticity.
To replicate more faithfully in-vivo behavior of cells, in Chapter 3, preliminary results and some first models have been presented to investigate the role that mechanics plays in *collective* cell behaviors, relevant in wound healing and embrogenesis processes (gastrulation). The introduction of the nonlinearities (upper convected Mawell model) leads a grater complexity on the computational side. For this reason the numerical simulations are still an ongoing work and the strategy to find the solution will be followed for expample by implementing Hu-washizu like variational formulation.

BIBLIOGRAPHY

[1] M. Abdolahad, Z. Sanaee, M. Janmaleki, S. Mohajerzadeh, M. Abdollahi, and M. Mehran. “Vertically aligned multiwall-carbon nanotubes to preferentially entrap highly metastatic cancerous cells.” In: *Carbon* 50.5 (2012), pp. 2010–2017. ISSN: 00086223. DOI: `10.1016/j.carbon.2012.01.001`. URL: `http://dx.doi.org/10.1016/j.carbon.2012.01.001http://linkinghub.elsevier.com/retrieve/pii/S0008622312000267`.

[2] Ida Ahmad and Mohd Ahmad. “Trends in characterizing single cell’s stiffness properties.” In: *Micro and Nano Systems Letters* 2 (2014), p. 8. ISSN: 2213-9621. DOI: `10.1186/s40486-014-0008-5`. URL: `http://www.mnsl-journal.com/content/2/1/8`.

[3] G Bao and S Suresh. “Cell and molecular mechanics of biological materials.” In: *Nature materials* 2.11 (2003), pp. 715–725. ISSN: 1476-1122.

[4] Markus Basan, Jens Elgeti, Edouard Hannezo, Wouter-jan Rappel, and Herbert Levine. “Alignment of cellular motility forces with tissue flow as a mechanism for efficient wound healing.” In: *Proceedings of the National Academy of Sciences of the United States of America* 110.7 (2013). URL: `http://www.pnas.org/cgi/content/long/110/7/2452`.

[5] Alfred Barnard Basset. *A Treatise on Hydrodynamics, with numerous examples*. Ed. by Cambridge University Press. Cambridge, 1888.

[6] Davide Bigoni. *Nonlinear Solid Mechanics Bifurcation Theory and Material Instability*. Cambridge: Cambridge University Press, 2012. ISBN: 9781107025417.

[7] G.W. Scott Blair and J.E. Caffyn. “An application of the theory of quasi-properties to the treatment of anomalous strain-stress relations.” In: *The London, Edinburgh, and Dublin Philosophical Magazine and Journal of Science* 40.300 (1949), pp. 80–94. ISSN: 1941-5982. DOI: `10.1080/14786444908561213`. URL: `http://www.tandfonline.com/doi/abs/10.1080/14786444908561213`.

[8] CE Brennen. *A review of added mass and fluid inertial forces.* January. 1982, p. 50. URL: `http://authors.library.caltech.edu/233/`.

[9] Claudia Brunner, Axel Niendorf, and Josef a. Käs. “Passive and active single-cell biomechanics: a new perspective in cancer diagnosis.” In: *Soft Matter* 5.11 (2009), p. 2171. ISSN: 1744-683X. URL: `http://xlink.rsc.org/?DOI=b807545j`.

[10] Danfeng Cai, Shann Ching Chen, Mohit Prasad, Li He, Xiaobo Wang, Valerie Choesmel-Cadamuro, Jessica K. Sawyer, Gaudenz Danuser, and Denise J. Montell. “Mechanical feedback through E-cadherin promotes direction sensing during collective cell migration.” In: *Cell* 157.5 (2014), pp. 1146–1159. ISSN: 10974172. DOI: `10.1016/j.cell.2014.03.045`. arXiv: `NIHMS150003`.

[11] Nathalie Caille, Olivier Thoumine, Yanik Tardy, and Jean-Jacques Meister. “Contribution of the nucleus to the mechanical properties of endothelial cells.” In: *Journal of Biomechanics* 35.2 (2002), pp. 177–187. ISSN: 00219290. DOI: `10.1016/S0021-9290(01)00201-9`. URL: `http://linkinghub.elsevier.com/retrieve/pii/S0021929001002019`.

[12] Brian A. Camley, Yunsong Zhang, Yanxiang Zhao, Bo Li, Eshel Ben-Jacob, Herbert Levine, and Wouter-Jan Rappel. “Polarity mechanisms such as contact inhibition of locomotion regulate persistent rotational motion of mammalian cells on micropatterns.” In: *Proceedings of the National Academy of Sciences* 111.41 (2014), pp. 14770–14775. ISSN: 0027-8424, 1091-6490. DOI: `10.1073/pnas.1414498111`. URL: `http://www.pnas.org/content/111/41/14770.full`.

[13] Andrew Campbell, Richard Archer, and Stephen Ebbens. “Preparation and 3D Tracking of Catalytic Swimming Devices.” In: *Journal of Visualized Experiments* 113 (2016). ISSN: 1940-087X. DOI: `10.3791/54247`. URL: `http://www.jove.com/video/54247/preparation-and-3d-tracking-of-catalytic-swimming-devices`.

[14] Stephanie S. Chang, Wei-hui Guo, Youngeun Kim, and Yu-li Wang. “Guidance of cell migration by substrate dimension.” In: *Biophysical journal* 104.2 (2013), pp. 313–21. ISSN: 1542-0086. DOI: `10.1016/j.bpj.2012.12.001`. URL: `http://linkinghub.elsevier.com/retrieve/pii/S0006349512050795http:`

`//www.ncbi.nlm.nih.gov/pubmed/23442853http://www.pubmedcentral.nih.gov/articlerender.fcgi?artid=PMC3552265`.

[15] Qiang Chen and Nicola M. Pugno. “Bio-mimetic mechanisms of natural hierarchical materials: A review.” In: *Journal of the Mechanical Behavior of Biomedical Materials* 19 (2013), pp. 3–33. ISSN: 17516161. DOI: `10.1016/j.jmbbm.2012.10.012`.

[16] Olga V Chumakova, Anton V Liopo, B Mark Evers, and Rinat O Esenaliev. “Effect of 5-fluorouracil, Optison and ultrasound on MCF-7 cell viability.” In: *Ultrasound in medicine & biology* 32.5 (2006), pp. 751–8. ISSN: 0301-5629. DOI: `10.1016/j.ultrasmedbio.2006.01.011`. URL: `http://www.ncbi.nlm.nih.gov/pubmed/16677934`.

[17] Caitlin Collins and W. James Nelson. “Running with neighbors: Coordinating cell migration and cell-cell adhesion.” In: *Current Opinion in Cell Biology* 36 (2015), pp. 62–70. ISSN: 18790410. DOI: `10.1016/j.ceb.2015.07.004`.

[18] G. Cottone, M. Di Paola, and M. Zingales. “Fractional mechanical model for the dynamics of non-local continuum.” In: *Advances in Numerical Methods*. Ed. by Nikos Mastorakis and John Sakellaris. Springer, 2009. Chap. 33, pp. 389–424. ISBN: 978-0-387-76482-5 (Print) 978-0-387-76483-2 (Online).

[19] C. R. P. Courtney, C.-K. Ong, B. W. Drinkwater, P. D. Wilcox, C. Demore, S. Cochran, P. Glynne-Jones, and M. Hill. “Manipulation of microparticles using phase-controllable ultrasonic standing waves.” In: *The Journal of the Acoustical Society of America* 128.4 (2010), EL195–EL199. ISSN: 0001-4966. DOI: `10.1121/1.3479976`. URL: `http://scitation.aip.org/content/asa/journal/jasa/128/4/10.1121/1.3479976`.

[20] Stephen C. Cowin and Stephen B. Doty. *Tissue mechanics*. Springer New York, 2007, pp. 1–682.

[21] John C Crocker and David G Grier. “Methods of Digital Video Microscopy for Colloidal Studies.” In: *JOURNAL OF COLLOID AND INTERFACE SCIENCE* 179 (1996), pp. 298–310. ISSN: 00219797. DOI: `10.1006/jcis.1996.0217`. arXiv: `96 [0021-9797]`.

[22] S.E. Cross, Y.-S. Jin, J. Tondre, R. Wong, J. Rao, and J.K. Gimzewski. "AFM-based analysis of human metastatic cancer cells." In: *Nanotechnology* 19.38 (2008), p. 384003. ISSN: 0957-4484. DOI: `10.1088/0957-4484/19/38/384003`. URL: `http://www.scopus.com/inward/record.url?eid=2-s2.0-51349158076{\&}partnerID=40{\&}md5=3a0f09a8e46f11a1ac2e47e44c24c0f6`.

[23] Sarah E Cross, Yu-Sheng Jin, Jianyu Rao, and James K Gimzewski. "Nanomechanical analysis of cells from cancer patients." In: *Nature nanotechnology* 2.12 (2007), pp. 780–783. ISSN: 1748-3395. DOI: `10.1038/nnano.2007.388`. URL: `http://www.ncbi.nlm.nih.gov/pubmed/18654431`.

[24] A Cugno, S Palumbo, L Deseri, M Fraldi, and Carmel Majidi. "Role of Nonlinear Elasticity in Mechanical Impedance Tuning of Annular Dielectric Elastomer Membrane." In: *submitted* (2017), pp. 1–18.

[25] A Cziròk, K Varga, E Méhes, and A Szabò. "Collective cell streams in epithelial monolayers depend on cell adhesion." In: *New Journal of Physics* 15.7 (2013), p. 075006. ISSN: 1367-2630. DOI: `10.1088/1367-2630/15/7/075006`. URL: `http://stacks.iop.org/1367-2630/15/i=7/a=075006?key=crossref.812706bef775c438250baf693201a8b3`.

[26] T Das, K Safferling, S Rausch, N Grabe, H Boehm, and J P Spatz. "A molecular mechanotransduction pathway regulates collective migration of epithelial cells." In: *Nat Cell Biol* 17.3 (2015), pp. 276–287. ISSN: 1476-4679. DOI: `10.1038/ncb3115`. URL: `http://www.ncbi.nlm.nih.gov/pubmed/25706233`.

[27] Sanjay Dastoor and Mark Cutkosky. "Design of dielectric electroactive polymers for a compact and scalable variable stiffness device." In: *2012 IEEE International Conference on Robotics and Automation*. April. IEEE, 2012, pp. 3745–3750. ISBN: 978-1-4673-1405-3. DOI: `10.1109/ICRA.2012.6224808`. URL: `http://ieeexplore.ieee.org/lpdocs/epic03/wrapper.htm?arnumber=6224808`.

[28] P.G. De Gennes and J Prost. *The physics of liquid crystals.* New York: Oxford University press, 1993. ISBN: 0198517858.

[29] M. Deforet, V. Hakim, H.G. Yevick, G. Duclos, and P. Silberzan. "Emergence of collective modes and tri-dimensional structures from epithelial confinement." In: *Nature Communications* 5 (2014).

ISSN: 2041-1723. DOI: `10.1038/ncomms4747`. URL: `http://www.nature.com/doifinder/10.1038/ncomms4747`.

[30] Gianpietro Del Piero and Luca Deseri. "On The Concepts of State and Free Energy in Linear Viscoelasticity." In: *Archive for Rational Mechanics and Analysis* 138.1 (1997), pp. 1–35.

[31] P. P. Delsanto, C. A. Condat, N. Pugno, A. S. Gliozzi, and M. Griffa. "A multilevel approach to cancer growth modeling." In: *Journal of Theoretical Biology* 250 (2008), pp. 16–24. ISSN: 00225193. DOI: `10.1016/j.jtbi.2007.09.023`.

[32] Ravi a Desai, Lin Gao, Srivatsan Raghavan, Wendy F Liu, and Christopher S Chen. "Cell polarity triggered by cell-cell adhesion via E-cadherin." In: *Journal of cell science* 122.Pt 7 (2009), pp. 905–11. ISSN: 0021-9533. DOI: `10.1242/jcs.028183`. URL: `http://www.pubmedcentral.nih.gov/articlerender.fcgi?artid=2720926{\&}tool=pmcentrez{\&}rendertype=abstract`.

[33] Luca Deseri, Mauro Fabrizio, and Murrough Golden. "The concept of a minimal state in viscoelasticity: New free energies and applications to PDEs." In: *Archive for Rational Mechanics and Analysis* 181 (2006), pp. 43–96. ISSN: 00039527. DOI: `10.1007/s00205-005-0406-1`.

[34] Luca Deseri, Mario Di Paola, Massimiliano Zingales, and Pietro Pollaci. "Power-law hereditariness of hierarchical fractal bones." In: *International Journal for Numerical Methods in Biomedical Engineering* 29 (2013), pp. 1338–1360. ISSN: 20407939. DOI: `10.1002/cnm.2572`.

[35] Kevin Doxzen, Sri Ram Krishna Vedula, Man Chun Leong, Hiroaki Hirata, Nir S. Gov, Alexandre J. Kabla, Benoit Ladoux, and Chwee Teck Lim. "Guidance of collective cell migration by substrate geometry." In: *Integrative Biology* 5.8 (2013), p. 1026. ISSN: 1757-9694. DOI: `10.1039/c3ib40054a`. URL: `http://xlink.rsc.org/?DOI=c3ib40054a`.

[36] Christopher C DuFort, Matthew J Paszek, and Valerie M Weaver. "Balancing forces: architectural control of mechanotransduction." In: *Nature reviews. Molecular cell biology* 12.5 (2011), pp. 308–319. ISSN: 1471-0072. DOI: `10.1038/nrm3112`. URL: `http://dx.doi.org/10.1038/nrm3112`.

[37] M Dundr and T Misteli. “Functional architecture in the cell nucleus.” In: *The Biochemical journal* 356.Pt 2 (2001), pp. 297–310. ISSN: 0264-6021. DOI: 10.1016/j.bbamcr.2008.09.007. URL: http://www.pubmedcentral.nih.gov/articlerender.fcgi?artid=1221839{\&}tool=pmcentrez{\&}rendertype=abstract.

[38] J W Ellwart, H Brettel, and L O Kober. “Cell membrane damage by ultrasound at different cell concentrations.” In: *Ultrasound in medicine & biology* 14.1 (1988), pp. 43–50. ISSN: 03015629.

[39] Mikael Evander and Johan Nilsson. “Acoustofluidics 20: Applications in acoustic trapping.” In: *Lab on a Chip* 12.22 (2012), p. 4667. ISSN: 1473-0197. DOI: 10.1039/c2lc40999b.

[40] E Evans and a Yeung. “Apparent viscosity and cortical tension of blood granulocytes determined by micropipet aspiration.” In: *Biophysical journal* 56.1 (1989), pp. 151–160.

[41] Elsa Correia Faria, Nan Ma, Ehsan Gazi, Peter Gardner, Mick Brown, Noel W Clarke, and Richard D Snook. “Measurement of elastic properties of prostate cancer cells using AFM.” In: *The Analyst* 133.11 (2008), pp. 1498–1500. ISSN: 0003-2654. DOI: 10.1039/b803355b.

[42] Eliseo Ferrante, Ali Emre Turgut, Marco Dorigo, and Cristian Huepe. “Elasticity-based mechanism for the collective motion of self-propelled particles with springlike interactions: A model system for natural and artificial swarms.” In: *Physical Review Letters* 111.26 (2013). ISSN: 00319007. DOI: 10.1103/PhysRevLett.111.268302.

[43] M. Fraldi and S. C. Cowin. “Inhomogeneous elastostatic problem solutions constructed from stress-associated homogeneous solutions.” In: *Journal of the Mechanics and Physics of Solids* 52 (2004), pp. 2207–2233. ISSN: 00225096. DOI: 10.1016/j.jmps.2004.04.004.

[44] M. Fraldi, A. Cugno, L. Deseri, K. Dayal, and N. M. Pugno. “A frequency-based hypothesis for mechanically targeting and selectively attacking cancer cells.” In: *Journal of The Royal Society Interface* 12.111 (2015), p. 20150656. ISSN: 1742-5689. DOI: 10.1098/rsif.2015.0656. URL: http://rsif.royalsocietypublishing
org/lookup/doi/10.1098/rsif.2015.0656.

[45] M Fraldi, A Cugno, A R Carotenuto, A Cutolo, N M Pugno, and L Deseri. "Small-on-Large Fractional Derivative Based Single-Cell Model Incorporating Cytoskeleton Prestretch." In: *Journal of Engineering Mechanics* (2016), p. D4016001. ISSN: 0733-9399. DOI: `10.1061/(ASCE)EM.1943-7889.0001178`. URL: `http://ascelibrary.org/doi/10.1061/(ASCE)EM.1943-7889.0001178`.

[46] Massimiliano Fraldi. "The mechanichal beauty of hierarchically organized living structures." In: *Scienza & Filosofia* 11 (2014), pp. 13–24. URL: `http://www.scienzaefilosofia.it/res/site70201/res679408{\_}02-FRALDI-11.pdf`.

[47] P. Friedl and K. Wolf. "Tumour-cell invasion and migration: diversity and escape mechanisms." In: *Nature reviews. Cancer* 3.5 (2003), pp. 362–74. ISSN: 1474-175X. DOI: `10.1038/nrc1075`. URL: `http://www.ncbi.nlm.nih.gov/pubmed/12724734`.

[48] Peter Friedl and Darren Gilmour. "Collective cell migration in morphogenesis, regeneration and cancer." In: *Nature Reviews Molecular Cell Biology* 10.7 (2009), pp. 445–457. ISSN: 1471-0072. DOI: `10.1038/nrm2720`. URL: `http://www.nature.com/doifinder/10.1038/nrm2720`.

[49] K. Fushimi and a. S. Verkman. "Low viscosity in the aqueous domain of cell cytoplasm measured by picosecond polarization microfluorimetry." In: *The Journal of cell biology* 112.4 (1991), pp. 719–25. ISSN: 0021-9525. URL: `http://www.pubmedcentral.nih.gov/articlerender.fcgi?artid=2288848{\&}tool=pmcentrez{\&}rendertype=abstract`.

[50] Annette Geltmeier, Beate Rinner, Dennis Bade, Katharina Meditz, Reiner Witt, Uwe Bicker, Catrin Bludszuweit-Philipp, and Patrick Maier. "Characterization of Dynamic Behaviour of MCF7 and MCF10A Cells in Ultrasonic Field Using Modal and Harmonic Analyses." In: *PLOS ONE* 10.8 (2015). Ed. by Yu-Jia Chang, e0134999. ISSN: 1932-6203. DOI: `10.1371/journal.pone.0134999`. URL: `http://dx.plos.org/10.1371/journal.pone.0134999`.

[51] P. Glynne-Jones, R.J. Boltryk, M. Hill, F. Zhang, L. Dong, J.S. Wilkinson, T. Brown, T. Melvin, and N.R. Harris. "Multi-modal particle manipulator to enhance bead-based bioassays." In: *Physics Procedia* 3.1 (2010), pp. 269–275. ISSN: 18753892. DOI: `10.`

`1016/j.phpro.2010.01.036`. URL: `http://linkinghub.elsevier.com/retrieve/pii/S1875389210000374`.

[52] Martin Groschl. “Ultrasonic Separation of Suspended Particles - Part I : Fundamentals.” In: *Acustica* 84.October 1997 (1998), pp. 432–447. ISSN: 00017884. DOI: `10.1109/ULTSYM.2001.991812`. URL: `http://www.ingentaconnect.com/content/dav/aaua/1998/00000084/00000003/art00006`.

[53] Caterina Guiot, Nicola Pugno, and Pier Paolo Delsanto. “Elastomechanical model of tumor invasion.” In: *Applied Physics Letters* 89 (2006). ISSN: 00036951. DOI: `10.1063/1.2398910`.

[54] Morton E. Gurtin. *An Introduction to Continuum Mechanics*. Ed. by Richard Bellman. New York: Academic Press, 1981. ISBN: 0-12-309750-9.

[55] Morton E. Gurtin, Eliot Fried, and Lallit Anand. *The Mechanics and Thermodynamics of Continua*. Cambridge: Cambridge University Press, 2010. ISBN: 9788578110796.

[56] Kristina Haase and Andrew E. Pelling. “Investigating cell mechanics with atomic force microscopy.” In: *Journal of The Royal Society Interface* 12.104 (2015), pp. 20140970–20140970. ISSN: 1742-5689, 1742-5662. DOI: `10.1098/rsif.2014.0970`. URL: `http://rsif.royalsocietypublishing.org/cgi/doi/10.1098/rsif.2014.0970`.

[57] Anna Haeger, Marina Krause, Katarina Wolf, and Peter Friedl. “Cell jamming: Collective invasion of mesenchymal tumor cells imposed by tissue confinement.” In: *Biochimica et Biophysica Acta - General Subjects* 1840.8 (2014), pp. 2386–2395. ISSN: 18728006. DOI: `10.1016/j.bbagen.2014.03.020`.

[58] Adrien Hallou, Joel Jennings, and Alexandre Kabla. “Cancer Metastasis: Collective Invasion in Heterogeneous Multicellular Systems.” In: *arXiv preprint* V (2014), p. 29. arXiv: `1501.0065`. URL: `http://arxiv.org/abs/1501.0006{\%}5Cnhttp://arxiv.org/abs/1501.0065`.

[59] S. Heyden and M. Ortiz. “Oncotripsy: Targeting cancer cells selectively via resonant harmonic excitation.” In: *Journal of the Mechanics and Physics of Solids* 92 (2016), pp. 164–175. ISSN: 00225096. DOI: `10.1016/j.jmps.2016.04.016`. arXiv: `1512.03320`. URL: `http://dx.doi.org/10.1016/j.jmps.2016.`

`04.016http://linkinghub.elsevier.com/retrieve/pii/S0022509615303161`.

[60] S. Heyden and M. Ortiz. "Investigation of the influence of viscoelasticity on oncotripsy." In: *Computer Methods in Applied Mechanics and Engineering* 314 (2017), pp. 314–322. ISSN: 00457825. DOI: `10.1016/j.cma.2016.08.026`. URL: `http://dx.doi.org/10.1016/j.cma.2016.08.026http://linkinghub.elsevier.com/retrieve/pii/S0045782516310210`.

[61] Gerhard A. Holzapfel. *Nonlinear solid mechanics: A continuum approach for engineering*. John Wiley & Sons, 2000, p. 455. ISBN: 047182304X.

[62] Hidemi Honda, Takashi Kondo, Qing-Li Zhao, Loreto B Feril, and Hiroshi Kitagawa. "Role of intracellular calcium ions and reactive oxygen species in apoptosis induced by ultrasound." In: *Ultrasound in medicine & biology* 30.5 (2004), pp. 683–92. ISSN: 0301-5629. DOI: `10.1016/j.ultrasmedbio.2004.02.008`. URL: `http://www.ncbi.nlm.nih.gov/pubmed/15183235`.

[63] Shiping Huang, Zhou Chen, Nicola Pugno, Qiang Chen, and Weifeng Wang. "A novel model for porous scaffold to match the mechanical anisotropy and the hierarchical structure of bone." In: *Materials Letters* 122 (2014), pp. 315–319.

[64] Jae Youn Hwang, Jihun Kim, Jin Man Park, Changyang Lee, Hayong Jung, Jungwoo Lee, and K. Kirk Shung. "Cell Deformation by Single-beam Acoustic Trapping: A Promising Tool for Measurements of Cell Mechanics." In: *Scientific Reports* 6 (2016), p. 27238. ISSN: 2045-2322. DOI: `10.1038/srep27238`. URL: `http://www.nature.com/articles/srep27238`.

[65] Yurii A Ilinskii, G Douglas Meegan, Evgenia A Zabolotskaya, and Stanislav Y Emelianov. "Gas bubble and solid sphere motion in elastic media in response to acoustic radiation force." In: *The Journal of the Acoustical Society of America* 117.4 Pt 1 (2005), pp. 2338–2346. ISSN: 00014966.

[66] Lennart D Johns. "Nonthermal effects of therapeutic ultrasound: The frequency resonance hypothesis." In: *Journal of Athletic Training* 37.3 (2002), pp. 293–299. ISSN: 10626050.

[67] Erika Jonieztz and Erika Jonietz. "The forces of cancer." In: *Science* 491.7425 (2012), S56–S57. ISSN: 0028-0836. DOI: `10.1038/491S56a`. URL: `http://www.nature.com/doifinder/10.1038/491S56a`.

[68] Douwe Kamsma, Ramon Creyghton, Gerrit Sitters, Gijs J L Wuite, and Erwin J G Peterman. "Tuning the Music: Acoustic Force Spectroscopy (AFS) 2.0." In: *Methods* 105 (2016), pp. 26–33. ISSN: 10959130. DOI: `10.1016/j.ymeth.2016.05.002`.

[69] Roland Kaunas, Shunichi Usami, and Shu Chien. "Regulation of stretch-induced JNK activation by stress fiber orientation." In: *Cellular Signalling* 18.11 (2006), pp. 1924–1931. ISSN: 08986568. DOI: `10.1016/j.cellsig.2006.02.008`.

[70] Alperen N. Ketene, Eva M. Schmelz, Paul C. Roberts, and Masoud Agah. "The effects of cancer progression on the viscoelasticity of ovarian cell cytoskeleton structures." In: *Nanomedicine: Nanotechnology, Biology and Medicine* 8.1 (2012), pp. 93–102. ISSN: 15499634. DOI: `10.1016/j.nano.2011.05.012`. URL: `http://dx.doi.org/10.1016/j.nano.2011.05.012http://linkinghub.elsevier.com/retrieve/pii/S1549963411001845`.

[71] Myung K. Kim. "Principles and techniques of digital holographic microscopy." In: *SPIE Reviews* 1.1 (2010), p. 018005. ISSN: 19463251. DOI: `10.1117/6.0000006`.

[72] Charles Kittel and Herbert Krocmer. *Thermal Physics*. 2nd editio. San Francisco: W. H. Freeman, 1980. ISBN: 0716710882.

[73] R. C. Koeller. "Applications of Fractional Calculus to the Theory of Viscoelasticity." In: *Journal of Applied Mechanics* 51.2 (1984), p. 299. ISSN: 00218936. DOI: `10.1115/1.3167616`. URL: `http://appliedmechanics.asmedigitalcollection.asme.org/article.aspx?articleid=1407520`.

[74] Nitin Kumar, Harsh Soni, Sriram Ramaswamy, and A K Sood. "Flocking at a distance in active granular matter." In: *Nature Communications* 5 (2014), p. 4688. ISSN: 2041-1723. DOI: `10.1038/ncomms5688`. arXiv: `arXiv:1402.4262v1`. URL: `http://www.nature.com/doifinder/10.1038/ncomms5688`.

[75] M. H. Lacker and Charles Peskin. "A mathematical method for the unique determination of cross-bridge properties from steady-state mechanical and energetic experiments on macroscopic mus-

cle." In: *Lectures on Mathematics in the Life Sciences* 16 (1986), pp. 121–153.

[76] Andreas Lamprecht, Stefan Lakämper, Thierry Baasch, Iwan A.T. Schaap, and Jürg Dual. "Imaging the position-dependent 3D force on micro beads subjected to acoustic radiation forces and streaming." In: *Lab Chip* 16 (2016), pp. 2682–2693. ISSN: 1473-0197. DOI: `10.1039/C6LC00546B`. URL: `http://pubs.rsc.org/en/Content/ArticleLanding/2016/LC/C6LC00546B`.

[77] L D Landau and E M Lifshitz. *Fluid Mechanics*. Ed. by McGraw-Hill. Vol. 6. Course of Theoretical Physics 1. Pergamon Press, 1987. Chap. Volume 6 o, p. 539. ISBN: 0080339336. DOI: `10.1007/b138775`. arXiv: `1003.3921v1`. URL: `http://www.springerlink.com/index/10.1007/b138775`.

[78] Pilhwa Lee and Charles W. Wolgemuth. "Crawling Cells Can Close Wounds without Purse Strings or Signaling." In: *PLoS Computational Biology* 7.3 (2011). Ed. by Andrew D. McCulloch, e1002007. ISSN: 1553-7358. DOI: `10.1371/journal.pcbi.1002007`. URL: `http://dx.plos.org/10.1371/journal.pcbi.1002007`.

[79] F Lejbkowicz, M Zwiran, and S Salzberg. "The response of normal and malignant cells to ultrasound in vitro." In: *Ultrasound in medicine & biology* 19.1 (1993), pp. 75–82. ISSN: 0301-5629. DOI: `10.1016/0301-5629(93)90020-O`.

[80] Flavio Lejbkowicz and Samuel Salzberg. "Distinct sensitivity of normal and malignant cells to ultrasound in vitro." In: *Environmental Health Perspectives* 105.SUPPL. 6 (1997), pp. 1575–1578. ISSN: 00916765. DOI: `10.1289/ehp.97105s61575`.

[81] M. Lekka, P. Laidler, D. Gil, J. Lekki, Z. Stachura, and A Z Hrynkiewicz. "Elasticity of normal and cancerous human bladder cells studied by scanning force microscopy." In: *European Biophysics Journal* 28.4 (1999), pp. 312–316. ISSN: 01757571. DOI: `10.1007/s002490050213`.

[82] Małgorzata Lekka et al. "Cancer cell detection in tissue sections using AFM." In: *Archives of Biochemistry and Biophysics* 518.2 (2012), pp. 151–156. ISSN: 00039861. DOI: `10.1016/j.abb.2011.12.013`.

[83] Małgorzata Lekka, Katarzyna Pogoda, Justyna Gostek, Olesya Klymenko, Szymon Prauzner-Bechcicki, Joanna Wiltowska-Zuber, Justyna Jaczewska, Janusz Lekki, and Zbigniew Stachura. “Cancer cell recognition - Mechanical phenotype.” In: *Micron* 43.12 (2012), pp. 1259–1266. ISSN: 09684328. DOI: `10.1016/j.micron.2012.01.019`. URL: `http://dx.doi.org/10.1016/j.micron.2012.01.019`.

[84] Bo Li and Sean X. Sun. “Coherent motions in confluent cell monolayer sheets.” In: *Biophysical Journal* 107.7 (2014), pp. 1532–1541. ISSN: 15420086. DOI: `10.1016/j.bpj.2014.08.006`.

[85] Q. S. Li, G. Y H Lee, C. N. Ong, and C. T. Lim. “AFM indentation study of breast cancer cells.” In: *Biochemical and Biophysical Research Communications* 374.4 (2008), pp. 609–613.

[86] David R Lide et al. *CRC Handbook of Chemistry and Physics*. 88th (Inte. Boca Raton, FL: CRC handbook of chemistry and physics, 2008.

[87] Etienne-Manneville S. Llense F. *Cell Polarity 1*. Ed. by Klaus Ebnet. Cham: Springer International Publishing, 2015. Chap. Front-to-r, pp. 115–146. ISBN: 978-3-319-14462-7. DOI: `10.1007/978-3-319-14463-4`. URL: `http://link.springer.com/10.1007/978-3-319-14463-4`.

[88] C. Majidi, R. E. Groff, and R. S. Fearing. “Analysis of Shaft-Loaded Membrane Delamination Using Stationary Principles.” In: *Mathematics and Mechanics of Solids* 13.1 (2007), pp. 3–22. ISSN: 1081-2865. DOI: `10.1177/1081286506068823`. URL: `http://mms.sagepub.com/cgi/doi/10.1177/1081286506068823`.

[89] Anastasios Marmaras, Ulrich Berge, Aldo Ferrari, Vartan Kurtcuoglu, Dimos Poulikakos, and Ruth Kroschewski. “A mathematical method for the 3D analysis of rotating deformable systems applied on lumen-forming MDCK cell aggregates.” In: *Cytoskeleton* 67.4 (2010), pp. 224–240. ISSN: 19493592. DOI: `10.1002/cm.20438`.

[90] MR R. Maxey and JJ J Riley. “Equation of motion for a small rigid sphere in a nonuniform flow.” In: *Physics of Fluids* 26.4 (1983), p. 883. ISSN: 00319171. DOI: `10.1063/1.864230`. URL: `http://scitation.aip.org/content/aip/journal/pof1/26/4/10.1063/1.864230http://scitation.aip.org/content/aip/journal/pof1/26/4/10.1063/1.864230$`

`\backslash$nhttp://link.aip.org/link/PFLDAS/v26/i4/p883/s1{\&}Agg=doi`.

[91] Roberto Mayor and Carlos Carmona-Fontaine. “Keeping in touch with contact inhibition of locomotion.” In: 20.6 (2010), pp. 319–328. ISSN: 09628924. DOI: `10.1016/j.tcb.2010.03.005`.

[92] P Memmolo, C Distante, M Paturzo, A Finizio, P Ferraro, and B Javidi. “Automatic focusing in digital holography and its application to stretched holograms.” In: *Optics letters* 36.10 (2011), pp. 1945–7. ISSN: 1539-4794. URL: `http://www.ncbi.nlm.nih.gov/pubmed/21593944`.

[93] Pasquale Memmolo, Andrea Finizio, Melania Paturzo, Lisa Miccio, and Pietro Ferraro. “Twin-beams digital holography for 3D tracking and quantitative phase-contrast microscopy in microfluidics.” In: *Optics Express* 19.25 (2011), p. 25833. ISSN: 1094-4087. DOI: `10.1364/OE.19.025833`.

[94] Pasquale Memmolo, Maria Iannone, Maurizio Ventre, Paolo Antonio Netti, Andrea Finizio, Melania Paturzo, and Pietro Ferraro. “On the holographic 3D tracking of in vitro cells characterized by a highly-morphological change.” In: *Optics express* 20.27 (2012), pp. 28485–93. ISSN: 1094-4087. URL: `http://www.ncbi.nlm.nih.gov/pubmed/23263084`.

[95] Pasquale Memmolo, Melania Paturzo, Bahram Javidi, Paolo A. Netti, and Pietro Ferraro. “Refocusing criterion via sparsity measurements in digital holography.” In: *Optics Letters* 39.16 (2014), p. 4719. ISSN: 0146-9592. DOI: `10.1364/OL.39.004719`. URL: `https://www.osapublishing.org/ol/abstract.cfm?uri=ol-39-16-4719`.

[96] Pasquale Memmolo, Lisa Miccio, Melania Paturzo, Giuseppe Di Caprio, Giuseppe Coppola, Paolo A. Netti, and Pietro Ferraro. “Recent advances in holographic 3D particle tracking.” In: *Advances in Optics and Photonics* 7.4 (2015), p. 713. ISSN: 1943-8206. DOI: `10.1364/AOP.7.000713`. URL: `http://www.osapublishing.org/viewmedia.cfm?uri=aop-7-4-713{\&}seq=0{\&}html=true`.

[97] C. Michelet-Habchi, S Incerti, P Aguer, Ph Barberet, E Gontier, T Guinefolleau, Ph Moretto, A. Pouthier, T Pouthier, and R W Smith. “3D imaging of microscopic structures using a proton

beam." In: *IEEE Transactions on Nuclear Science* 52.3 (2005), pp. 612–617. ISSN: 00189499. DOI: `10.1109/TNS.2005.851411`.

[98] Puja Mishra, Martyn Hill, and Peter Glynne-Jones. "Deformation of red blood cells using acoustic radiation forces." In: *Biomicrofluidics* 8.3 (2014). ISSN: 19321058. DOI: `10.1063/1.4882777`.

[99] Natalya Mizrahi, Enhua H. Zhou, Guillaume Lenormand, Ramaswamy Krishnan, Daphne Weihs, James P. Butler, David a. Weitz, Jeffrey J. Fredberg, and Eitan Kimmel. "Low intensity ultrasound perturbs cytoskeleton dynamics." In: *Soft Matter* 8 (2012), p. 2438. ISSN: 1744-683X. DOI: `10.1039/c2sm07246g`.

[100] Mehdi Nikkhah, Jeannine S. Strobl, Raffaella De Vita, and Masoud Agah. "The cytoskeletal organization of breast carcinoma and fibroblast cells inside three dimensional (3-D) isotropic silicon microstructures." In: *Biomaterials* 31.16 (2010), pp. 4552–4561. ISSN: 01429612. DOI: `10.1016/j.biomaterials.2010.02.034`. URL: `http://dx.doi.org/10.1016/j.biomaterials.2010.02.034`.

[101] P.G. Nutting. "A new general law of deformation." In: *Journal of the Franklin Institute* 191.5 (1921), pp. 679–685. ISSN: 00160032. DOI: `10.1016/S0016-0032(21)90171-6`. URL: `http://appliedmechanics.asmedigitalcollection.asme.org/article.aspx?articleid=1407520http://linkinghub.elsevier.com/retrieve/pii/S0016003221901716`.

[102] Y. N. Ohshima and I. Nishio. "Colloidal crystal: Bead-spring lattice immersed in viscous media." In: *Journal of Chemical Physics* 114.19 (2001), pp. 8649–8658. ISSN: 00219606. DOI: `10.1063/1.1366640`.

[103] Meir Or and Eitan Kimmel. "Modeling Linear Vibration of Cell Nucleus in Low Intensity Ultrasound Field." In: *Ultrasound in Medicine and Biology* 35.6 (2009), pp. 1015–1025. ISSN: 03015629. DOI: `10.1016/j.ultrasmedbio.2008.11.011`. URL: `http://www.ncbi.nlm.nih.gov/pubmed/19376638`.

[104] M. Pachenari, S.M. Seyedpour, M. Janmaleki, S. Babazadeh Shayan, S. Taranejoo, and H. Hosseinkhani. "Mechanical properties of cancer cytoskeleton depend on actin filaments to microtubules content: Investigating different grades of colon cancer cell lines." In: *Journal of Biomechanics* 47.2 (2014), pp. 373–379. ISSN: 00219290. DOI: `10.1016/j.jbiomech.2013.11.020`. URL:

http://dx.doi.org/10.1016/j.jbiomech.2013.11.020http://linkinghub.elsevier.com/retrieve/pii/S0021929013005721.

[105] Matthew J. Paszek et al. “The cancer glycocalyx mechanically primes integrin-mediated growth and survival.” In: *Nature* 511.7509 (2014), pp. 319–25. ISSN: 1476-4687. DOI: 10.1038/nature13535. URL: http://www.nature.com/doifinder/10.1038/nature13535$\backslash$nhttp://www.ncbi.nlm.nih.gov/pubmed/25030168.

[106] P Pathmanathan, J Cooper, a Fletcher, G Mirams, P Murray, James M Osborne, J Pitt-Francis, a Walter, and S J Chapman. “A computational study of discrete mechanical tissue models.” In: *Physical biology* 6.3 (2009), p. 036001. ISSN: 1478-3975. DOI: 10.1088/1478-3975/6/3/036001. arXiv: 67649966616. URL: http://www.ncbi.nlm.nih.gov/pubmed/19369704.

[107] Ron Pelrine and Roy Kornbluh. “Variable-Stiffness â€“ Mode Dielectric Elastomer Devices.” In: 61 (2008), pp. 192–201. DOI: 10.4028/www.scientific.net/AST.61.192.

[108] Ron Pelrine et al. “High-speed electrically actuated elastomers with strain greater than 100%.” In: *Science (New York, N.Y.)* 287.5454 (2000), pp. 836–9. ISSN: 1095-9203. DOI: 10.1126/science.287.5454.836. URL: http://www.ncbi.nlm.nih.gov/pubmed/10657293.

[109] Ron Pelrine, Roy D. D. Kornbluh, Qibing Pei, Scott Stanford, Seajin Oh, Joseph Joe Eckerle, Robert J. J. Full, Marcus a. Rosenthal, and Kenneth Meijer. “Dielectric elastomer artificial muscle actuators: toward biomimetic motion.” In: *Proceedings of SPIE* 4695.3 (2002), pp. 126–137. ISSN: 0277786X. DOI: 10.1117/12.475157. URL: http://link.aip.org/link/?PSI/4695/126/1{\&}Agg=doi.

[110] L. Petitjean, M. Reffay, E. Grasland-Mongrain, M. Poujade, B. Ladoux, A. Buguin, and P. Silberzan. “Velocity fields in a collectively migrating epithelium.” In: *Biophysical Journal* 98.9 (2010), pp. 1790–1800. ISSN: 00063495. DOI: 10.1016/j.bpj.2010.01.030.

[111] Marija Plodinec et al. “The nanomechanical signature of breast cancer.” In: *Nature Nanotechnology* 7.11 (2012), pp. 757–765.

ISSN: 1748-3387. DOI: 10.1038/nnano.2012.167. URL: http://www.nature.com/doifinder/10.1038/nnano.2012.167.

[112] M Poujade, E Grasland-Mongrain, a Hertzog, J Jouanneau, P Chavrier, B Ladoux, a Buguin, and P Silberzan. “Collective migration of an epithelial monolayer in response to a model wound.” In: *Proceedings of the National Academy of Sciences of the United States of America* 104.41 (2007), pp. 15988–15993. ISSN: 0027-8424. DOI: 10.1073/pnas.0705062104.

[113] Meenakshi Prabhune, Gazanfer Belge, Andreas Dotzauer, Jörn Bullerdiek, and Manfred Radmacher. “Comparison of mechanical properties of normal and malignant thyroid cells.” In: *Micron* 43.12 (2012), pp. 1267–1272. ISSN: 09684328. DOI: 10.1016/j.micron.2012.03.023. URL: http://dx.doi.org/10.1016/j.micron.2012.03.023.

[114] Nicola M. Pugno, Federico Bosia, and Tamer Abdalrahman. “Hierarchical fiber bundle model to investigate the complex architectures of biological materials.” In: *Physical Review E - Statistical, Nonlinear, and Soft Matter Physics* 85 (2012). ISSN: 15393755. DOI: 10.1103/PhysRevE.85.011903.

[115] L M Rebelo, J S de Sousa, J Mendes Filho, and M Radmacher. “Comparison of the viscoelastic properties of cells from different kidney cancer phenotypes measured with atomic force microscopy.” In: *Nanotechnology* 24.5 (2013), p. 055102. ISSN: 1361-6528. DOI: 10.1088/0957-4484/24/5/055102. URL: http://www.ncbi.nlm.nih.gov/pubmed/23324556.

[116] Marita L. Rodriguez, Patrick J. McGarry, and Nathan J. Sniadecki. “Review on Cell Mechanics: Experimental and Modeling Approaches.” In: *Applied Mechanics Reviews* 65.6 (2013), p. 060801. ISSN: 0003-6900. DOI: 10.1115/1.4025355. URL: http://www.scopus.com/inward/record.url?eid=2-s2.0-84887878152{\&}partnerID=40{\&}md5=289208c8f24a5305ccaed //appliedmechanicsreviews.asmedigitalcollection.asme.org/article.aspx?doi=10.1115/1.4025355.

[117] Stefan G. Samko, Anatoly A. Kilbas, and Oleg I. Marichev. *Fractional Integrals and Derivatives*. Amsterdam: Gordon and Breach Science Pubblishers, 1993. ISBN: 2-88124-864-0.

[118] A Schuster, T Schwab, M Bischof, M Klotz, R Lemor, C Degel, and K. H. Schäfer. “Cell specific ultrasound effects are dose and frequency dependent.” In: *Annals of Anatomy* 195.1 (2013), pp. 57–67. ISSN: 09409602. DOI: `10.1016/j.aanat.2012.03.008`. URL: `http://www.ncbi.nlm.nih.gov/pubmed/22683001`.

[119] G.W Scott Blair. “The role of psychophysics in rheology.” In: *Journal of Colloid Science* 2.1 (1947), pp. 21–32. ISSN: 00958522. DOI: `10.1016/0095-8522(47)90007-X`. URL: `http://linkinghub.elsevier.com/retrieve/pii/009585224790007X`.

[120] Mikkel Settnes and Henrik Bruus. “Forces acting on a small particle in an acoustical field in a viscous fluid.” In: *Physical Review E* 85.1 (2012), p. 016327. ISSN: 1539-3755. DOI: `10.1103/PhysRevE.85.016327`. URL: `http://link.aps.org/doi/10.1103/PhysRevE.85.016327`.

[121] Gerrit Sitters, Douwe Kamsma, Gregor Thalhammer, Monika Ritsch-Marte, Erwin J G Peterman, and Gijs J L Wuite. “Acoustic force spectroscopy.” In: *Nature methods* 12.1 (2015), pp. 47–50. ISSN: 1548-7105. DOI: `10.1038/nmeth.3183`. URL: `http://www.ncbi.nlm.nih.gov/pubmed/25419961`.

[122] S. S. Soumya, Animesh Gupta, Andrea Cugno, Luca Deseri, Kaushik Dayal, Dibyendu Das, Shamik Sen, and Mandar M. Inamdar. “Coherent Motion of Monolayer Sheets under Confinement and Its Pathological Implications.” In: *PLOS Computational Biology* 11.12 (2015). Ed. by Anand R. Asthagiri, e1004670. ISSN: 1553-7358. DOI: `10.1371/journal.pcbi.1004670`. arXiv: `1507.06481`. URL: `http://dx.plos.org/10.1371/journal.pcbi.1004670http://www.ncbi.nlm.nih.gov/pubmed/26691341http://www.pubmedcentral.nih.gov/articlerender.fcgi?artid=PMC4686989`.

[123] B Szabó, G J Szöllösi, B. Gönci G. J, Jurányi Zs, Selmeczi D, and Vicsek T. “Phase transition in the collective migration of tissue cells: Experiment and model.” In: *Physical Review E* 74.6 (2006), p. 061908. ISSN: 1539-3755. DOI: `10.1103/PhysRevE.74.061908`. URL: `http://link.aps.org/doi/10.1103/PhysRevE.74.061908`.

[124] Dhananjay T Tambe et al. “Collective cell guidance by cooperative intercellular forces.” In: *Nature materials* 10.6 (2011), pp. 469–75. ISSN: 1476-1122. DOI: `10.1038/nmat3025`. URL: `http://dx.doi.org/10.1038/nmat3025`.

[125] K. Tanner, H. Mori, R. Mroue, A. Bruni-Cardoso, and M. J. Bissell. “Coherent angular motion in the establishment of multicellular architecture of glandular tissues.” In: *Proceedings of the National Academy of Sciences* 109.6 (2012), pp. 1973–1978. ISSN: 0027-8424. DOI: `10.1073/pnas.1119578109`. URL: `http://www.pnas.org/cgi/doi/10.1073/pnas.1119578109`.

[126] K.M. Taute, S. Gude, S.J. Tans, and T.S. Shimizu. “High-throughput 3D tracking of bacteria on a standard phase contrast microscope.” In: *Nature Communications* 6 (2015), p. 8776. ISSN: 2041-1723. DOI: `10.1038/ncomms9776`. URL: `http://www.nature.com/doifinder/10.1038/ncomms9776`.

[127] Nw Tschoegl. *The phenomenological theory of linear viscoelastic behavior: an introduction*. Springer New York, 1989. ISBN: 9783642736049. URL: `http://www.getcited.org/pub/102712842`.

[128] Tamás Vicsek and Anna Zafeiris. “Collective motion.” In: *Physics Reports* 517.3-4 (2012), pp. 71–140. ISSN: 03701573. DOI: `10.1016/j.physrep.2012.03.004`. URL: `http://linkinghub.elsevier.com/retrieve/pii/S0370157312000968`.

[129] Barbara Wandelt, Piotr Cywinski, Graham D. Darling, and Brent R. Stranix. “Single cell measurement of micro-viscosity by ratio imaging of fluorescence of styrylpyridinium probe.” In: *Biosensors and Bioelectronics* 20.9 (2005), pp. 1728–1736. ISSN: 09565663. DOI: `10.1016/j.bios.2004.06.045`. URL: `http://www.ncbi.nlm.nih.gov/pubmed/15681187`.

[130] Hugo Wioland, Francis G. Woodhouse, Jörn Dunkel, John O. Kessler, and Raymond E. Goldstein. “Confinement Stabilizes a Bacterial Suspension into a Spiral Vortex.” In: *Physical Review Letters* 110.26 (2013), p. 268102. ISSN: 0031-9007. DOI: `10.1103/PhysRevLett.110.268102`. URL: `http://link.aps.org/doi/10.1103/PhysRevLett.110.268102`.